LOW TEMPERATURE PLASMA MODELLING TECHNIQUES FOR ARC DISCHARGE AND HALL-EFFECT THRUSTERS

A Thesis

by

ADNAN MANSOUR

Submitted to the Office of Graduate and Professional Studies of
Texas A&M University
in partial fulfillment of the requirements for the degree of

MASTER OF SCIENCE

Chair of Committee,	Alexandros Gerakis
Co-Chair of Committee,	Kentaro Hara
Committee Member,	David Staack
Head of Department,	Rodney Bowersox

December 2019

Major Subject: Aerospace Engineering

ABSTRACT

The growth of plasma applications in industrial and scientific settings has led to the need for consistent computational plasma models. The multi-scale, highly nonlinear physics involved in plasma processes creates a challenging environment for computational modelling. Different combinations of assumptions and approximations are utilized to ease the computational burden associated with plasma fluid models.

The goal of this research work is to document and describe in detail the theory, numerical modelling and results of two separate projects in plasma modelling. The first project is a multi-species one-dimensional model of ablating carbon arc discharge, namely for the synthesis of carbon nanotubes. It focuses on the development of chemical and physical models, as well as the derivation of multiple governing equations and boundary conditions used. Governing equations are solved for eleven species, and the chemical composition of the arc is dynamically updated. Multiple parameters are varied and benchmarked against each other. Numerical results are presented from published work and compared to experimental results, with which they have shown good agreement.

The second project describes the development of numerical methods for a one-dimensional non-neutral drift-diffusion plasma model for Hall-effect thrusters. The overarching purpose of the project is to investigate the anomalous electron transport observed in experiments, yet to be captured by numerical models, by removing general assumptions one step at a time. The end goal is to have a simulation that does not rely on artificially introducing the empirical anomalous transport coefficient to achieve levels of electron mobility observed in experimental setups. This project removes the quasi-neutral assumption and solves for the electrons as a separate species, utilizing the drift-diffusion model. It focuses on the implementation of several numerical schemes that are developed to help alleviate the severe timestep size restrictions associated with non-neutral plasma models. Results are compared with results from neutral simulations as well as other non-neutral models in development.

DEDICATION

To Mom, Dad, Jamjoomeh and Flaps. Always in my heart.

ACKNOWLEDGMENTS

First and foremost, I would like to thank Dr. Ken Hara for all the work we have done together over the past two years, and all the work that is yet to come. Your mentorship has vastly expanded my knowledge and understanding not only in academic matters, but in life matters as well. Your unrelenting drive inspires me and pushes me to strive for nothing short of the best in my work, and for that I am eternally grateful. Your attention to details resonates with mine, and your methods of instruction are what I hope to exemplify in my future career. I hope that the coming years will be just as fruitful as the two that have passed.

I cannot express my gratitude for my professors at Texas A&M enough. I want to thank Dr. Diego Donzis for his engaging and thought-provoking teaching methods. Your way of quizzically positing ideas forced me to question my understanding of concepts in fluid mechanics and ultimately vastly improved my grasp on the fundamentals. I would like to thank Dr. John Hurtado for his impeccable abilities in teaching complex concepts in such an elegant manner. Somehow, your three-hour-long lectures always ended too quickly, and they were always greatly enjoyable. I would also like to thank Dr. Amine Benzerga for so gracefully instructing a subject that is very complex, and somehow making it elegantly beautiful. Your eloquence and methods will continue to inspire me when I become a professor in the future. Last but not least, many thanks to Dr. Alan Demlow from the math department for his chalkboards upon chalkboards of theories, proofs, and lemmas on numerical methods for PDE's. Your class was both a challenge and a delight through and through. Finally, I would like to express my sincere gratitude to my committee members, Dr. Alexandros Gerakis and Dr. David Staack from the mechanical engineering department, for the extremely fruitful and helpful discussions regarding my thesis, without which this work would not have been completed.

To the many amazing people I've met in College Station, thank you. My eternal love and gratitude goes to Frankie, for being such a kindhearted, compassionate and intelligent

soul, and to Johnny, for always engaging me in social and historical discussions, and for inspiring me with your diligence. Both of you were my family away from home, and this work could not have been completed without your camaraderie and support. I want to thank Nick, who exemplified all that is beautiful in the Texan spirit. Your warm welcome when I was a stranger in a new land will forever be remembered. A hearty thank you to Ryan for being such a diabolically entertaining DM, and to Taryn and Erin and the rest of the gang for those insanely hilarious D&D Friday nights. Thank you Hunter for getting me into so many new things, and for those chill Sundays of cooking, watching TV and talking about music. Thanks to Rupali for all those times we sat together, confused why our codes refused to work. I couldn't have finished this thesis without your help. Last but most definitely not least, a huge thank you to Christine for being my comrade in existential dread as we faced the unknown these past few months. In the midst of the chaos of the qualifying exams, the thesis and everything in between, we helped each other get through everything and made it to the finish line. A shout-out to all the wonderful people I've met in College Station over these past two years that I haven't mentioned by name. All of you have made my experience beyond delightful, and you'll all be missed but not forgotten.

I could not be where I am today without the everlasting and boundless love of my family. Mom and Dad, you were in my thoughts the entire time, and your unending support drove me the way it has always done. I will continue to push forward and achieve my dreams that you've worked so hard to help me attain. I have never gone this long without your loving touch, but you both managed to give me strength to keep on going. Zeenah, soon to be MD, you always were and always will be one of the cornerstones upon which I rest the foundation of my life. Your diligence and hard work always inspires me, as do the hardheadedness and compassion that drive you. Lilas, my baby sis, always a bubbling bundle of joy from your earliest years. You are now blazing your own trail into the unknown, fiercely and boldly, and I am always proud of you. Saad, you may not be my brother by blood, but you've been in the family for so long that you might as well be. I will soon join you in the ranks of doctors, albeit

a different kind. My Aunt Randa, I miss your comforting, loving embrace, and I always feel in your protective presence. You are symbol of matriarchal strength like none other, and none of us in the family would be where we are without you. To Grandma, my uncles, and all my cousins and other relatives in Syria and elsewhere, it may have been years since we've seen each other, but no time or distance can come between us. Thank you all for the unwavering love and support.

Lastly, my profound thanks to the warrior along the sidelines, my best friend Hassan. Thousands of miles separate us, and yet you are always there for me. Thank you for all the countless sleepless nights you've spent with me whenever I was going through rough times. Thank you for believing in me no matter the circumstances. Thank you for helping me become the person that I am today, and encouraging me to continue growing. Most importantly, thank you for being my friend.

If I could go on, this acknowledgement would be dozens of pages. Thank you, everyone.

CONTRIBUTORS AND FUNDING SOURCES

Contributors

This work was supported by a thesis committee consisting of Professors Kentaro Hara and Alexandros Gerakis of the Department of Aerospace Engineering and Professor David Staack of the Department of Mechanical Engineering. The author acknowledges collaboration with his advisor Professor Kentaro Hara throughout the course of his research, and with his colleague Rupali Sahu for the work and discussion on the second part of this thesis.

All other work conducted for the thesis was completed by the student independently.

Funding Sources

Graduate study was supported by the Air Force Office of Scientific Research under award number FA9550-18-1-0090 and by the National Science Foundation under award number NSF-PHY #1903481.

TABLE OF CONTENTS

Page

LIST OF FIGURES

FIGURE Page

LIST OF TABLES

TABLE Page

1. INTRODUCTION: LOW TEMPERATURE PLASMAS

This work presents two low temperature plasma (LTP) projects that were developed over the past two years. The first project is of an ablating carbon arc discharge model that solves the governing equations for multiple species simultaneously and self-consistently resolves the plasma chemistry. The second project is of a non-neutral drift-diffusion Hall effect thruster simulation that solves the governing equations for electrons and ions using Hall thruster operating parameters. The two parts are treated separately, and are, for the most part, independent of each other.

The arc discharge portion of the research work focuses on theoretical physical and chemical models, developed and discussed in detail. Inter-species interactions and heat and current balances at the boundaries are the main scope of the study. Qualitative comparison to empirical data shows good agreement between the model and experimental results. While the research work simulates carbon arc discharge for carbon nanotube synthesis, the synthesis itself is not considered a part of the study. While emphasis is placed on the carbon deposit from which nanotubes are extracted, the model does not delve into the particular production of fullerenes.

The Hall effect thruster portion of the research work focuses on the development of numerical models that simulate the operation of a Hall thruster using a non-neutral drift-diffusion model. Methods are developed to resolve issues involved with timestep limitations of non-neutral plasma models. Comparisons are made between the model and a similar quasineutral model, and the effects of plasma non-neutrality are discussed.

Both models utilize the fluid approach to solve for macroscopic quantities that characterize the plasma. In the fluid description, the plasma is considered collisional due to a high background pressure, high densities, or both. It is advantageous to use the fluid approach when possible because it is a lot less computationally expensive than its particle counterpart. The models presented are considered collisional, and the fluid formulation is used to limit

the computational costs.

Plasma is generally regarded as the fourth state of matter, and it constitutes over 99.9 percent of the universe [5]. It can be characterized by the dissociation of neutral atoms into charged species (e.g. positive ions and negative electrons), forming an electrified, current carrying gas. Plasma is defined as a quasineutral gas of charged and neutral particles which exhibits collective behavior [5]. The plasma behaves collectively because local conditions and properties are affected by fringe sections of the plasma. One of the defining properties of plasmas is the phenomenon known as Debye shielding. Plasma particles are shielded by each other from electromagnetic fields imposed on them. Despite each particle having its own charge, in a pool of particles, same charges repel each other, creating localities that are relatively of the opposite charge. This leads to the particles' electric fields being negated, and leads to the screening effect known as Debye shielding. This is largely due to the high conductivity of plasma allowing for electric currents to flow through freely [6]. The length at which charged particles screen out external fields is known as the Debye length. If and when the Debye length is much smaller than the physical scale of the plasma, the local shielding of external electric fields causes the ion and electron densities to be approximately equal; this condition is referred to as quasineutrality. Plasma is quasineutral throughout a volume of ionized gas except near the boundaries, such as close to walls [7].

Different classes of plasma are generally characterized by n, the plasma number density, and T_e, the electron temperature, which directly depends on the electron energy. Both parameters vary widely: the density can be as low as 10^5 m^{-3} in interstellar medium [8] and as high as 10^{26} m^{-3} in laser plasmas [9], whereas the temperature can range from sub-1 electron-Volt (eV) for interstellar plasma up to tens of thousands of eV in thermonuclear plasmas [9, 10]. Nevertheless, the same set of equations can sufficiently describe any plasma, since only classical laws of physics are needed [5].

A significant sub-category of plasmas is low temperature plasma (LTP), which includes many of the industrial applications of plasma, such as gas discharges, arc welding, electric

propulsion, plasma-assisted combustion and many more [11]. LTPs are characterized by electron energies on the order of a few eV up to 10 eV, which is on the order of 100,000 K, with a relatively low ionization degree, such that the plasma is said to be partially ionized, although in some instances, the ionization degree can be high and the plasma is fully ionized [5, 11]. Other characterizations of LTPs include whether or not they operate in thermal equilibrium, such that the electron and ion temperatures are close or equal, although in most situations that is not the case [11].

Even within LTPs, scales vary drastically, with pressures spanning nine orders of magnitude in range [12], and spatial scales varying over a similar range [13]. Temporal scales can vary over up to twelve orders of magnitudes, from picoseconds to several minutes [13]. The wide range of spatial and temporal scales involved in LTP operation regimes creates challenges when it comes to the creation of computational models for LTPs. The highly coupled and nonlinear physics involved in the operation of LTPs further increases the challenges of creating computational models. However, over the past three decades, with the increase of computational power, effective modelling techniques have allowed for more robust models that have expanded plasma physics [11].

Our understanding of plasma processes is continuously being reinforced by numerical models. Plasma models are typically divided into kinetic models, fluid models, and hybrid kinetic models, with each having advantages, disadvantages, and applicable regimes [14]. All three modelling techniques share the same underlying fundamental physical laws, which are based on gas kinetic equations, namely the Boltzmann and the Vlasov equations [15, 16]. In the regime of LTPs, the plasma is considered highly collisional, and a fluid description can sufficiently model the physics, with some exceptions, such as in sheaths. This section will describe and formulate some of the fundamental governing equations applicable to the fluid description of plasmas.

2. BOLTZMANN EQUATION

The macroscopic behavior of gases can be captured from the microscopic behavior of their particles using the Boltzmann equation [17]. The derivation in the following section is largely based on the derivations from Refs. [17], [18] and [19], with collisional quantities being from Ref. [20]. The derivation of the equation begins by defining the distribution function:

$$f(\mathbf{x}, \mathbf{v}, t) d^3\mathbf{x} d^3\mathbf{v},$$

where f is the distribution function, dependent on the position $\mathbf{x}$, the velocity $\mathbf{v}$, and the time t. The distribution function corresponds to the number of particles present at time t in infinitesimal volume $d^3\mathbf{x}$ around point $\mathbf{x}$, within an infinitesimal velocity interval $d^3\mathbf{v}$ around velocity $\mathbf{v}$. The probability of a particle being within a spatial and velocity interval corresponds to the integration of the distribution function over that interval.

The evolution of the distribution function over time can be written in the general form of:

$$\frac{df}{dt} = \left(\frac{\partial f}{\partial t}\right)_{\text{diffusion}} + \left(\frac{\partial f}{\partial t}\right)_{\text{external}} + \left(\frac{\partial f}{\partial t}\right)_{\text{collision}}, \tag{2.1}$$

where the diffusion term corresponds to the diffusive evolution of the particle distribution; the external term corresponds to forces exerted on the particles externally; and the collision term corresponds to inter-particle interactions through collisions. It can be inferred that the change in the total number of particles in an element over time can be written as:

$$\frac{\partial f}{\partial t} d^3\mathbf{v} d^3\mathbf{x}, \tag{2.2}$$

as long as the the location and shape of the element does not change over time.

The diffusion term describes the evolution of particles with velocity $\mathbf{v}$ leaving the infinitesimal space $d^3\mathbf{x}$ over time t. The number flux of the molecules moving across surface

element dS can be written as:

$$f(\mathbf{x}, \mathbf{v}, t)d^3\mathbf{v}(\mathbf{v} \cdot \mathbf{e_r} dS),$$

where $\mathbf{e_r}$ is the unit vector normal to surface dS, pointing out of the volume $d^3\mathbf{x}$. Integrating over surface dS gives the total number flux through the surface, and using Gauss-divergence theorem, the volume integral form of the flux becomes:

$$-\int_{\mathbf{x}} \nabla \cdot (f\mathbf{v})d(d^3\mathbf{x})d^3\mathbf{v},$$

which can be integrated over the volume, becoming $-\nabla \cdot (f\mathbf{v})d^3\mathbf{x}d^3\mathbf{v}$. The velocity $\mathbf{v}$ is assumed to be constant over the volume, and so $\nabla \cdot \mathbf{v} = 0$. The diffusive term in Eq. (2.1) thus becomes:

$$-\mathbf{v} \cdot \nabla f d^3\mathbf{v}d^3\mathbf{x}. \tag{2.3}$$

By identifying that the external term of Eq. (2.1) corresponds to the particles that have gained velocity $d^3\mathbf{v}$ when exerted upon by external force $\mathbf{F}$, a similar derivation to the one done for the diffusive term leads to the expression for the external force term:

$$-\frac{\mathbf{F}}{m} \cdot \nabla_{\mathbf{v}} f d^3\mathbf{v}d^3\mathbf{x}, \tag{2.4}$$

where m is the particle mass, and $\nabla_{\mathbf{v}}$ is the gradient of the distribution function in the velocity space. The collisional term of Eq. (2.1) will be denoted by $C(f)d^3\mathbf{v}d^3\mathbf{x}$, which is the collision operator over the space and velocity space, and is a function of the distribution function. Combining Eqs. (2.1)-(2.4) with the collision operator, and cancelling $d^3\mathbf{v}d^3\mathbf{x}$ yields:

$$\frac{\partial f}{\partial t} + \mathbf{v} \cdot \nabla f + \frac{\mathbf{F}}{m} \cdot \nabla_{\mathbf{v}} f = C(f), \tag{2.5}$$

which is the Boltzmann equation, accounting for collisions and external forces.

2.1 Moments of the Boltzmann Equation

When describing plasma as a fluid, macroscopic quantities are used to characterize the plasma, and these quantities come directly from the distribution function. By taking the velocity moments of the distribution function, the number density n, the bulk velocity $\mathbf{u}$, and the mean energy ε can all be defined as follows:

$$n(\mathbf{x}, t) = \int_{\mathbf{v}} f d^3\mathbf{v},$$

$$\mathbf{u} = \langle \mathbf{v} \rangle = \frac{1}{n} \int_{\mathbf{v}} \mathbf{v} f d^3\mathbf{v},$$

$$\varepsilon = \frac{m}{2} \left\langle |\mathbf{v}|^2 \right\rangle = \frac{m}{2n} \int_{\mathbf{v}} |\mathbf{v}|^2 f d^3\mathbf{v},$$

where the triangular brackets indicate the macroscopic average of the quantity. It is important to distinguish between the particle velocity $\mathbf{v}$ and the bulk velocity $\mathbf{u}$: the particle velocity is the sum of the mean velocity and the random velocity of particles.

Assuming that the only external influences are due to electromagnetic fields, since gravity can be considered negligible, the Boltzmann equation (Eq. (2.5)) can be written as:

$$\frac{\partial f}{\partial t} + \mathbf{v} \cdot \nabla f + \frac{q}{m}(\mathbf{E} + \mathbf{v} \times \mathbf{B}) \cdot \nabla_{\mathbf{v}} f = C(f), \tag{2.6}$$

where $\mathbf{E}$ is the electric field, $\mathbf{B}$ is the magnetic field, and q is the charge. By taking the moments of Eq. (2.6), the fluid governing equations can be derived.

2.1.1 Continuity equation

By integrating Eq. (2.6) over the velocity space, the conservation of mass, or continuity, is derived. The force term cancels through a combination of the Gauss-divergence theorem and that the integral is evaluated over all values of the velocity space, such that the surface of the integral is at infinity where no particles reside. Utilizing the definitions of n and $\mathbf{u}$ from

the Boltzmann distribution, the continuity equation becomes:

$$\frac{\partial n}{\partial t} + \nabla \cdot (n\mathbf{u}) = S, \tag{2.7}$$

where $S = \int_{\mathbf{v}} C(f) d^3\mathbf{v}$ involves the source and the sink for the particle density.

2.1.2 Conservation of momentum equation

Integrating the first moment of Eq. (2.6), by multiplying the equation by $\mathbf{v}$, gives the conservation of momentum equation. The derivation is done using index notation for brevity. Once again, utilizing the definitions of n and $\mathbf{u}$, the equation becomes:

$$\frac{\partial (nu_m)}{\partial t} + \nabla \cdot (n\langle v_m v_i \rangle) + \int_{\mathbf{v}} v_m \frac{\partial (Q_i f)}{\partial v_i} dv^3 = C_m,$$

where $Q_i = q/m(E_i + \varepsilon_{ijk} v_j B_k)$ is the external force, contracted for brevity, ε_{ijk} is the permutation symbol, and C_m is the momentum transfer due to collisions, which will be shown later. The third term in the equation can be rewritten such that:

$$\int_{\mathbf{v}} v_m \frac{\partial (Q_i f)}{\partial v_i} dv^3 = \int_{\mathbf{v}} \left(\frac{\partial (Q_i f v_m)}{\partial v_i} - Q_i f \delta_{im} \right) dv^3,$$

where δ_{ik} is the Kronecker delta operator. The first term cancels using Gauss-divergence, and the second term, when integrated, yields $Q_m n$.

By substituting $v_i = u_i + w_i$, where w_i is the random motion of the particle, and identifying that the macroscopic average of the random motion is zero, the term $\langle v_m v_i \rangle$ becomes:

$$\langle v_m v_i \rangle = u_m u_i + \langle w_m w_i \rangle,$$

where the second term is the stress tensor. While the stress tensor consists of the pressure term and the viscosity term, an approximation is usually made for plasmas, such that the stress tensor is diagonal and isotropic, denoted by $p\delta_{im}$, where p is the gas pressure. Combining

the terms together, the momentum conservation equation becomes:

$$\frac{\partial(n\mathbf{u})}{\partial t} + \nabla \cdot (n\mathbf{u} \otimes \mathbf{u}) + \frac{1}{m}\nabla p = \frac{qn}{m}(\mathbf{E} + \mathbf{u} \times \mathbf{B}) + C, \tag{2.8}$$

where the collisional term on the right hand side is given by:

$$C = -n_m \sum_j \frac{m_j}{m_m + m_j} n_j k_{mj} (\mathbf{u}_m - \mathbf{u}_j),$$

where the summation is done over all the different species in the fluid, and k_{mj} is the momentum transfer rate coefficient of the collisional event between species m and j.

2.1.3 Conservation of energy equation

Integrating the second moment of Eq. (2.6) gives the fluid energy equation. Using the definitions of n, $\mathbf{u}$ and ε, the equation becomes:

$$\frac{\partial(n\langle v^2\rangle)}{\partial t} + \nabla \cdot (n\langle v_i v^2\rangle) + \int_{\mathbf{v}} v^2 \frac{\partial(Q_i f)}{\partial v_m} dv^3 = \frac{2\mathbf{C}_m}{m},$$

where $\mathbf{C}_m$ is the energy exchange through collisions, and the factor of 2/m is simply used to make the derivation more compact. Using a similar process as in Section 2.1.2, the equation becomes:

$$\frac{\partial(n\langle v^2\rangle)}{\partial t} + \nabla \cdot (n\langle v_i v^2\rangle) - 2nQ_m\langle v_m\rangle = \frac{2\mathbf{C}_m}{m}.$$

Expanding the particle velocity, identifying that the average of the mean bulk velocity is the mean bulk velocity itself, and using the relation between the energy and the average particle velocity, the equation becomes:

$$\frac{\partial}{\partial t}\left(\frac{2n\varepsilon}{m}\right) + \nabla \cdot (n\langle 2u_m w_m w_i + u_i u^2 + w_i w^2 + u_i w^2\rangle) - 2nQ_m\langle u_m\rangle = \frac{2\mathbf{C}_m}{m},$$

Substituting the pressure term for the stress tensor and combining terms, the second term in the equation becomes:

$$\nabla \cdot \left(\frac{2n\varepsilon}{m} u_m + \frac{2p}{m} u_m + \frac{2q_m}{m} \right),$$

where q_m is the heat conduction term. Rewriting the equation, the energy equation becomes:

$$\frac{\partial n\varepsilon}{\partial t} + \nabla \cdot (n\varepsilon \mathbf{u} + p\mathbf{u} + \mathbf{q}) = qn\mathbf{E} \cdot \mathbf{u} + \mathbf{C}, \tag{2.9}$$

where energy transfer due to collisions on the right hand side is given by:

$$\mathbf{C} = -n_m \sum_j \Delta\varepsilon_j n_j k_j - n_m \sum_j \frac{2m_j}{m_m + m_j} n_j k_{mj} (\varepsilon_m - \varepsilon_j),$$

where the first term is the energy transfer due to inelastic collisions, $\Delta\varepsilon_j$ energy lost or gained due to an inelastic collision reaction, and the second term is the energy transfer due to elastic collisions.

This concludes the derivation of the fluid governing equations for plasmas from the Boltzmann equation. These equations will be the basis of the models for both parts of the thesis.

3. PART I: ABLATING CARBON ARC DISCHARGE *

The synthesis of carbon nanomaterials by means of arc discharge has been a rapidly expanding area of research since its inception over two decades ago [21]. The wide range of applications for carbon nanomaterials, including high strength composites, energy storage devices, hydrogen storage media, sensors, and nanoscale semiconductor devices, has sparked great interest in the field [22]. Carbon arc discharge has been used for the manufacturing of single-walled [23, 24] and multi-walled carbon nanotubes [25, 26]. To understand the detailed mechanisms of nanomaterial synthesis, it is vital to gain insight into the physical and chemical processes of the arc discharge plasmas, including plasma-material interactions, a wide range of spatial and temporal scales, and interspecies and microscopic interactions, such as collisions, reactions, and chemistry [27].

The process of nanomaterial synthesis with arc discharge involves an ablating carbon anode, from which the particles evaporate, and the cathode, upon which the particles coalesce into layers of nanotubes [28]. *Ex situ* measurements have traditionally been used to characterize the nanomaterials post-synthesis, using electron microscopy and forms of spectroscopy to analyze the composition and quality of the nanomaterials [28, 29]. Recent methods in laser diagnostics have allowed for *in situ* measurements of the formation of the nanoparticles [29, 30, 31]. This advancement allows for the characterization of the discharge plasma and precursor species during the synthesis process. The development of numerical models alongside these advancements on the experimental front is vital to increase our understanding of this rapidly growing field.

*Reprinted with permission from "Multispecies plasma fluid simulation for carbon arc discharge" by Adnan Mansour and Kentaro Hara, 2019. Journal of Physics D: Applied Physics, Volume 52, Page 105204, Copyright 2019 by IOP Publishing Ltd.

4. INTRODUCTION & LITERATURE SURVEY

Over the past two decades, several computational models have been developed to simulate arc discharge plasmas [32, 33, 34, 35, 36] that account for various assumptions, such as thermal, chemical, or velocity equilibrium and steady-state assumption. For arc discharge plasmas, local thermal and chemical equilibrium have often been assumed [35]. Thermal equilibrium refers to the treatment of the plasma as having a single temperature for all of its constituents. Chemical equilibrium usually involves the utilization of approximations, such as the Saha equation [20, 37], to approximate the source term for each component, as opposed to individually accounting for the reactions taking place within the plasma. Typically, these assumptions are called local thermodynamic equilibrium (LTE). The assumption of LTE implies that the changes in the velocity distribution functions and the population densities over the distance of a mean free path for elastic collisions between identical particles are small [35].

Another approach used for the numerical models is a non-LTE condition, which refers to thermal nonequilibrium [38] or chemical nonequilibrium [35], while, for example, the Saha equilibrium is still used to obtain ionization and recombination rate coefficients [34, 36]. A full set of rate equations can be solved to calculate the species concentration for each component of the plasma [39]. Some models separate the domain to an LTE arc core and non-LTE plasma sheaths [40]. Nonequilibrium effects can be observed in the regions near the electrodes and in the arc periphery, where synthesis processes are important. Although high collisionality is considered to make plasma approach LTE, the validity of LTE condition remains an open question.

In addition to equilibrium and nonequilibrium modelling, steady state assumption is often used [41, 42, 43, 44], which reduces the set of equations to the heat and current balances. In Ref. [41], the ablation rate is considered as an input parameter, not a function of the anode temperature. In Ref. [45] the ablation rate is calculated and a fluid equation of a single

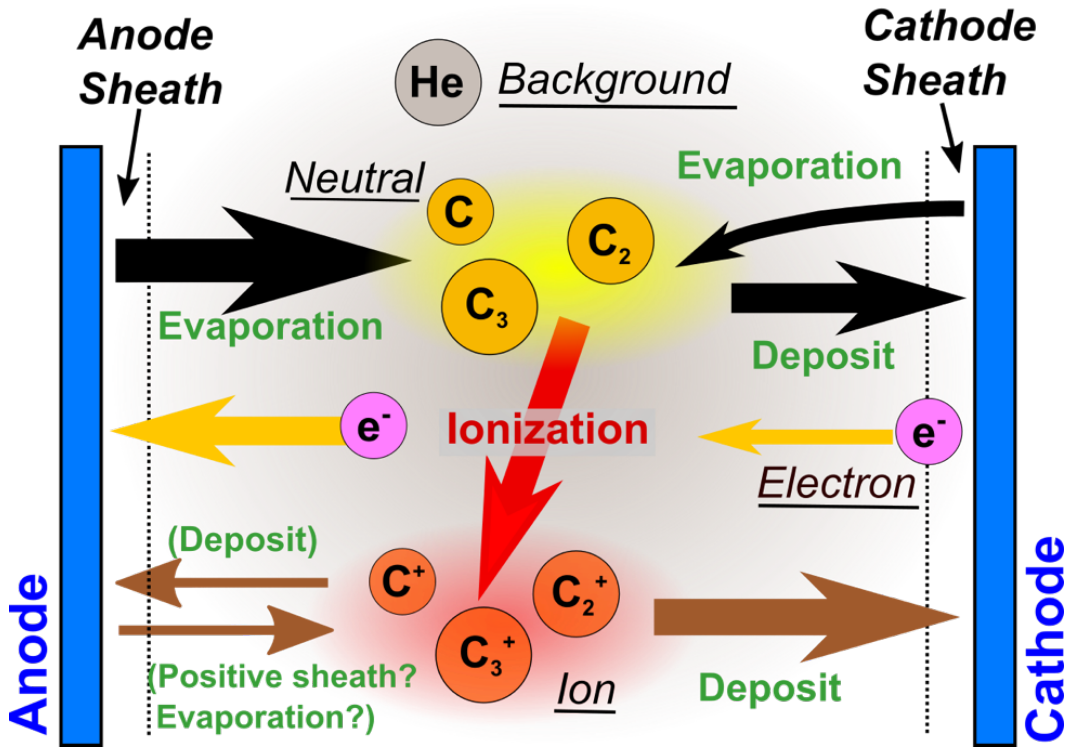

Figure 4.1: Schematic of an ablating arc discharge plasma using graphite electrodes, operating in the atmospheric pressure range using a background inert gas, e.g., helium.

fluid is solved, using chemical equilibrium to account for the plasma chemistry. In order to understand arc discharge plasmas, it is vitally important to develop a *self-consistent* plasma model that accounts for the nonlinear coupling between the composition of the arc plasma and boundary conditions.

The model simulates the operation of an ablating carbon arc used in the synthesis of carbon nanotubes. Figure 4.1 provides a schematic representation of the arc discharge plasma using ablating graphite electrodes. The bulk plasma, which includes carbon species as well as the background inert gas, e.g., helium, interacts with the plasma sheaths at the anode and the cathode. Material evaporation takes place at the anode, and the material gets deposited at the cathode, with some of the deposit reevaporating due to the high cathode temperature. The electron current is supplied from the cathode through electron emissions, and the ionization takes place in the bulk plasma.

It is important to note that the model is designed to allow for any number of species and reactions to be added easily. This could allow for different chemical models and the inclusion of increasingly multiply charged species. Additionally, this allows the model to simulate arc discharges using ablating material other than carbon, such as Boron Nitride. Boron Nitride (BN) nanotubes share a similar structure to carbon nanotubes, and present a definitively growing area of interest in scientific and industrial communities. They have comparable moduli to their carbon counterparts, but BN nanotubes are thermo-mechanically stable in high temperatures [46]. Moreover, unlike the semi-conducting carbon nanotubes, BN nanotubes are excellent insulators, allowing for a variety of applications [46]. It would be fruitful to conduct a study using Boron-Nitride as the ablating material; this is reserved for future work.

5. MULTISPECIES ARC DISCHARGE MODEL

In this model, a one-dimensional (1D) arc discharge that resolves the multispecies bulk plasma using effective sheath boundary conditions is simulated. The fluid governing equations are solved for each species, and detailed current and heat flux balances at the electrodes are used to obtain the wall temperatures and sheath potential drop. No equilibrium assumptions are considered: the temperatures of the electrons and heavy species are solved separately, chemical equations are solved to simulate the composition of the arc, and no velocity equilibrium is assumed. The model's sensitivity to multiple parameters is presented and discussed, with results being compared to experiments.

A set of mass and momentum conservation equations is considered for each species. The species in the model include atomic, diatomic, and triatomic carbon in ground state (C, C_2, C_3), excited states (C^*, C_2^*, C_3^*), and ionized states (C^+, C_2^+, C_3^+), atomic helium (He) as the buffer gas, and electrons (e). The gas pressure in the arc plasma is typically in atmospheric pressure for similar applications [44], and a fluid model is employed due to large collisionality. The domain resolved by the model ends at the sheath edges in the vicinity of the electrodes, employing effective sheath boundary conditions. As such, the plasma in the solution domain can be considered quasineutral, i.e., the electron density is equal to the ion density.

5.1 Heavy Species Transport

The heavy species are modeled by solving the conservation equations. Gaseous carbon is provided via evaporation of the electrodes, which is determined by the electrode temperature. Here, conservation of mass, evaporation model, and conservation of momentum are discussed.

5.1.1 Conservation of mass

The 1D mass conservation equation is given by,

$$\frac{\partial n_s}{\partial t} + \frac{\partial (n_s u_s)}{\partial x} = S_s, \tag{5.1}$$

where n_s, u_s, and S_s are the number density, bulk velocity, and the collisional term, respectively, for a given species s. The collisional term includes detailed chemical balance, taking into account dissociation, direct and stepwise ionization, excitation and quenching, which are discussed later. Species s include n, i, $*$ and e, corresponding to atoms, ions, excited particles, and electrons, respectively.

The collisional term S_s depends on the reaction rates and the number densities of the species involved, which can be written as,

$$S_s = \sum_j X_j k_j \prod_{r=1}^{p} n_{r,j}, \tag{5.2}$$

where k_j is the reaction rate coefficient, and $n_{r,j}$ is the number density of the reactants up to p reactants, for a given reaction j. When the species of interest is a reactant, it is being depleted and $X_j = -1$. When the species is a product, it is being generated and $X_j = +1$.

5.1.2 Evaporation model

The vapor pressure of carbon species is given by the following formulae, suggested by Thorn and Winslow [47]:

$$\log_{10}(p_1) = -\frac{37227.3}{T_0} + 8.143, \tag{5.3}$$

$$\log_{10}(p_2) = -\frac{42332.6}{T_0} + 9.693, \tag{5.4}$$

$$\log_{10}(p_3) = -\frac{40296.0}{T_0} + 9.811, \tag{5.5}$$

where p_1, p_2, p_3 are the vapor pressure in atm for C, C_2, and C_3, respectively, and T_0 is the material temperature in Kelvin. The values in the numerator in Eqs. (5.3) -(5.5) correspond to the heat of vaporization of the species, ΔH, which are shown in Table 5.1. In the present model, carbon molecules larger than triatomic molecules are not accounted for because the data provided by Drowart [3] shows that the evaporation flux of larger molecules (C_n, where $n > 3$) is a few orders of magnitude smaller compared to that of C, C_2, and C_3. This is consistent with the data in Table 5.1, as it is more difficult to evaporate material when ΔH is higher.

Using the vapor pressure, the evaporation flux is given by [48],

$$\Gamma_{\text{evp}} = p(T_0)\sqrt{\frac{1}{2\pi M k_B T_0}}, \tag{5.6}$$

where M is the mass of the vapor gas, k_B is the Boltzmann constant, and Γ_{evp} is the evaporation rate per unit area, in $1/(\text{m}^2 \cdot \text{s})$.

It is to be noted that the net evaporation flux of Thorn and Winslow [47] is in agreement with Dushman's experimental data [49], which is given by,

$$\mathcal{F}_{\text{evp}}(T_0) = C T_0^{-1/2} 10^{A - B/T_0}, \tag{5.7}$$

where $\mathcal{F}_{\text{evp}}(T_0)$ is the evaporated mass flow rate per unit area in $\text{kg}/(\text{m}^2\text{s})$, $C = 10$ $\text{kg}/(\text{m}^2\text{s})$,

Table 5.1: Heat of vaporization. Data from Drowart [3] and data shown in parenthesis are from Honig [4].

Species	ΔH kcal/mol.
C	169.58 (177)
C_2	195.8 (199)
C_3	188.1 (177)
C_4	229.5
C_5	232.5

and A and B are constants dependent on the cathode material. For graphite [50], $A = 12.04$ and $B = 40,030$ K are used.

5.1.3 Conservation of momentum

The conservative form of the momentum equation in 1D is given for each species by,

$$\frac{\partial(\rho_i u_i)}{\partial t} + \frac{\partial(\rho_i u_i^2)}{\partial x} + \frac{\partial p_i}{\partial x} = F_i, \tag{5.8}$$

for ions, and,

$$\frac{\partial(\rho_n u_n)}{\partial t} + \frac{\partial(\rho_n u_n^2)}{\partial x} + \frac{\partial p_n}{\partial x} = F_n, \tag{5.9}$$

for neutrals, where $\rho_s = m_s n_s$ is the mass density, m_s is the species mass, p_s is the pressure, which is assumed to obey the ideal gas law, and F_s is a combination of external or body forces for species $s = i, n$.

The force for ions in Eq. (5.8) can be written as,

$$F_i = e n_i E + \rho_i \sum_j \nu_{ij}(u_i - u_j) + S_i m_n u_n, \tag{5.10}$$

where e is the elementary charge, E is the electric field, and ν_{ij} is the collision frequency between species i and j, which is comprised of electron-ion and ion-ion Coulomb collisions for ions, as well as neutral-ion momentum exchange. The term $S_i m_n u_n$ accounts for the addition of slow ion flux via ionization, as the newly generated ions retain the same velocity as the neutral species. Note that the term S_i is the ionization rate given in Eqs. (5.1) and (5.2). Self-induced magnetic field and the corresponding Lorentz force are ignored due to the one-dimensional assumption. For neutral species in Eq. (5.9), the body forces term is given by,

$$F_n = \rho_n \sum_j \nu_{nj}(u_n - u_j) - S_i m_n u_n. \tag{5.11}$$

The collisions accounted for are neutral-neutral and neutral-ion momentum exchange, and

Table 5.2: Species accounted for in the model.

Species	Energy level (eV)	Remark
C	0	-
C^*	8.846	$2p3p(^3P)$
C^+	11.26	-
C_2	0	-
C_2^*	2.394	$C_2^* \rightarrow C_2$ (e.g., Swan band)
C_2^+	11.79	-
C_3	0	-
C_3^*	3.062	$C_3^* \rightarrow C_3$ (e.g., Swings band)
C_3^+	13.00	-
He	0	Ionization at 24.59 eV.
e^-	-	-

electron-neutral elastic collisions. The last term in the right hand side of Eq. (5.11) accounts for the neutral momentum loss via ionization.

5.2 Carbon Chemistry

Collisions and their resulting reaction rates are critical for both the species generation term in the mass conservation equations and the momentum transfer in the momentum conservation equations.

Table 5.2 shows the species accounted for in the present model. One excited state for each carbon species is assumed, based on the most dominant transition. For atomic carbon, using excitation data from Sasaki [51], the most dominant excited energy level is $2p3p(^3P)$, for which the energy difference from the ground state is 8.846 eV [52]. For molecular carbon, information is scarcer; therefore, the excited levels implemented are the ones most prominently detected. For C_2, Swan bands are detected in relatively high-pressure carbon arcs [53]. The emission of Swan bands, corresponding to a transition of $d^3\Pi_g$ to $a^3\Pi_u$, is the most intense C_2 emission [54]. The energy difference between said levels is 2.394 eV [55]. Similarly, the most observable emission for C_3 is that of Swings band [53], corresponding to a transition between $X^1\Sigma_g$ to $a^1\Pi_u$, and the latter is considered the excited level in the model,

Table 5.3: Electron impact reactions accounted for in the model.

Label	Reaction	Energy	Remarks
E1	$C + e \rightarrow C^+ + e + e$	11.26 eV	Direct ioniz.
E2	$C + e \rightarrow C^* + +e$	8.85 eV	Excitation
E3	$C^* + e \rightarrow C + e$	-8.85 eV	Quenching
E4	$C^* + e \rightarrow C^+ + e + e$	2.41 eV	Stepwise ioniz.
E5	$C_2 + e \rightarrow C_2^+ + e + e$	11.8 eV	Direct ioniz.
E6	$C_2 + e \rightarrow C_2^* + +e$	2.39 eV	Excitation
E7	$C_2^* + e \rightarrow C_2 + e$	-2.39 eV	Quenching
E8	$C_2^* + e \rightarrow C_2^+ + e + e$	9.41 eV	Stepwise ioniz.
E9	$C_3 + e \rightarrow C_3^+ + e + e$	13 eV	Direct ioniz.
E10	$C_3 + e \rightarrow C_3^* + +e$	3.06 eV	Excitation
E11	$C_3^* + e \rightarrow C_3 + e$	-3.06 eV	Quenching
E12	$C_3^* + e \rightarrow C_3^+ + e + e$	9.94 eV	Stepwise ioniz.
E13	$He + e \rightarrow He + e$	-	Elastic
E14	$C_M + e \rightarrow C_M + +e$ (C_M: all carbon species)	-	Elastic

with an energy difference of 3.061 eV [56].

Helium excited particles and ions are not considered due to their large excitation and ionization energies compared to the other species, e.g., the first excitation energy and the direct ionization energy for He are 19.819 eV and 24.587 eV, respectively, whereas the ionization energy is 11.26 eV for C atoms [52], 11.79 eV for C_2 molecules [57], and 13 eV for C_3 molecules [58]. Similarly, doubly and triply charged carbon ions are not considered, since the ionization energies for doubly and triply charged carbon with respect to singly charged carbon ions are 24.38 eV and 47.89 eV, respectively [52]. Since the arc discharge of interest has a voltage of approximately 20 V and the calculated electron temperature is 1-2 eV, helium ions are neglected and only singly charged positive carbon ions are taken into account.

5.2.1 Excitation & de-excitation

The rate coefficients for electron-impact excitation and ionization are given by,

$$k_j(T_e) = \int \sigma_j(\varepsilon)\sqrt{\frac{2\varepsilon}{m_e}} f(\varepsilon, T_e) d\varepsilon, \tag{5.12}$$

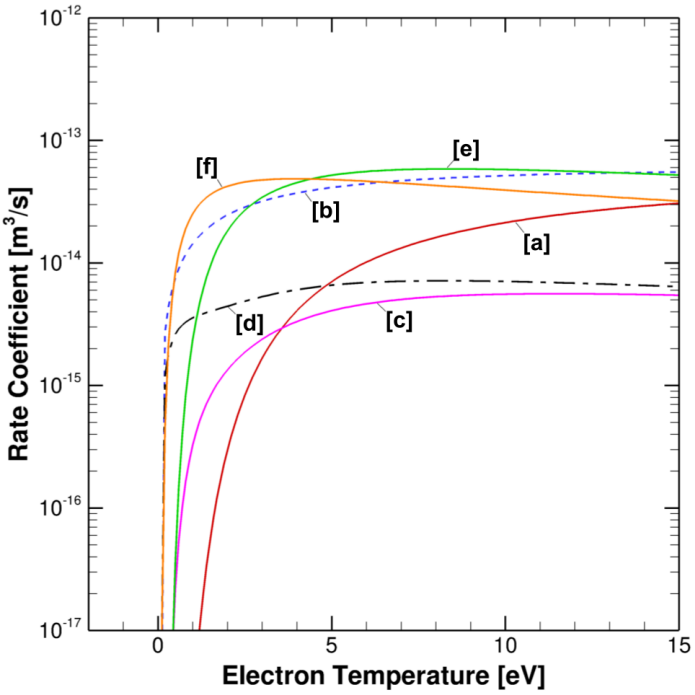

Figure 5.1: Rate coefficients of excitation and quenching assuming a Maxwellian EEDF: [a] C excitation, [b] C quenching, [c] C_2 excitation, [d] C_2 quenching, [e] C_3 excitation, [f] C_3 quenching.

where σ_j is the cross section for reaction j, $f(\varepsilon, T_e)$ is the energy distribution function (EEDF) assumed to be a Maxwellian, T_e is the electron temperature, and ε is the electron energy. Electron impact reactions are summarized in Table 5.3.

Figure 5.1 shows the rate coefficients for excitation and quenching assuming a Maxwellian EEDF. The cross section of electron-impact excitation from state i to state j for C is given by Suno and Kato [59] in the following form,

$$\sigma_{ij}(\varepsilon) = 1.1969 \times 10^{-15} \times \frac{\Omega_{ij}}{g_i \varepsilon}, \tag{5.13}$$

where Ω_{ij} is the collision strength, g_i is the statistical weight of the initial state, and the cross section $\sigma_{ij}(\varepsilon)$ is in cm^2. The collision strength Ω_{ij} is fitted from experimental data for

excitation to various excited states from ground state carbon, and is given as,

$$\Omega_{ij} = \omega_0 + \frac{\omega_1}{X_{ij}} + \frac{\omega_2}{X_{ij}^2} + \frac{\omega_3}{X_{ij}^3} + \omega_4 \ln X_{ij}, \tag{5.14}$$

where $X_{ij} = \varepsilon/\Delta E_{ij}$ is the reduced electron energy and ΔE_{ij} is the difference in energy levels in eV. For $2p3p(^3P)$ excited state, the values are given as [59] $\omega_0 = 7.728$, $\omega_1 = -0.8661$, $\omega_2 = -16.40$, $\omega_3 = 7.754$, and $\omega_4 = 0$.

The cross section for C_2 excitation is taken from Halmová [60], and the data for C_3 is acquired from Munjal [61]. For both species, the data only covers electron energy below 10 eV. As such, the data was extrapolated using an exponential fit up to a higher energy to calculate Maxwellian-averaged rate coefficients.

The quenching rate coefficients are also shown in Fig. 5.1. The model takes collisional de-excitation, or quenching, of the carbon species into account. Detailed balance for the three excitation reactions is considered using Boltzmann's relation, which is given as $k_j/k_i = g_i/g_j \exp(-\Delta E_{ij}/T_{eV})$ [20], where T_{eV} is the electron temperature in eV, to calculate the quenching rates.

De-excitation due to spontaneous emission, such as Swan and Swings bands, are taken into account. The de-excitation frequencies are assumed to be 7.14×10^6 Hz, estimated based on the lifetime of high pressure Swan bands [62, 53]. An optically thin plasma is assumed in the present model, hence radiation trapping is neglected.

5.2.2 Ionization & recombination

Figure 5.2 shows the direct and stepwise ionization rate coefficients assuming a Maxwellian EEDF. The cross section for electron-impact direct ionization of atomic carbon is given as a function of electron energy by Suno and Kato [59], fitted from experimental data,

$$\sigma(\varepsilon) = \frac{10^{-13}}{E_i \varepsilon} \left[A_1 \ln\left(\frac{\varepsilon}{E_i}\right) + \sum_{z=2}^{5} A_z \left(1 - \frac{E_i}{\varepsilon}\right)^{z-1} \right], \tag{5.15}$$

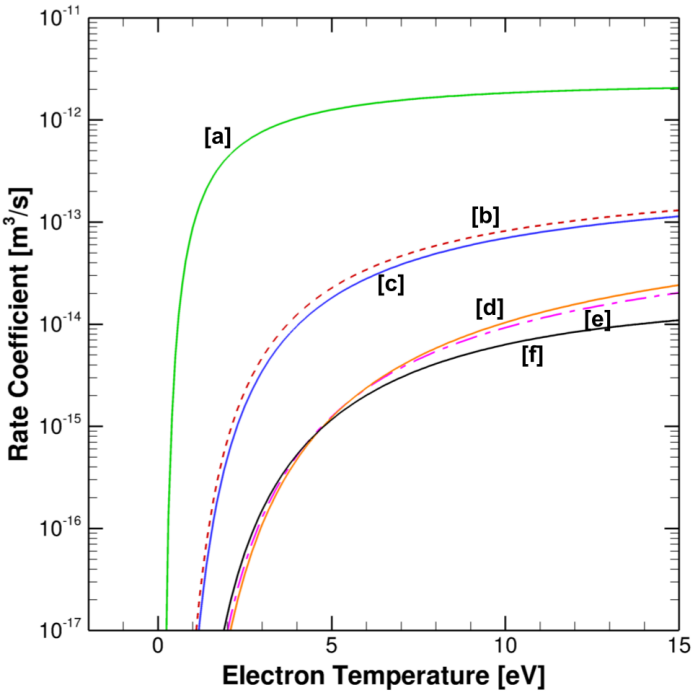

Figure 5.2: Rate coefficients of direct and stepwise ionization assuming a Maxwellian EEDF: [a] C stepwise ionization, [b] C_2 stepwise ionization, [c] C_3 stepwise ionization, [d] C_3 direct ionization, [e] C_2 direct ionization, [f] C direct ionization.

where $\sigma(\varepsilon)$ is in cm^2, E_i is the ionization energy, A_1=1.829, A_2=-1.975, A_3=1.149, A_4=-3.583, and A_5=2.451 for the ionization of carbon.

Experimental data is not available for the ionization of C_2 and C_3, so theoretical models are used to obtain their ionization cross section data and their respective ionization rate coefficients. The electron-impact ionization cross sections for diatomic and triatomic carbon are taken from Deutsch and Märk [63].

For the stepwise ionization of atomic carbon, Vriens and Smeets's model is used [64]. It employs the following equation for the cross section:

$$\sigma(\varepsilon) = \pi a_0^2 \frac{4R_y^2}{\varepsilon + \alpha E_i}\left(\frac{5}{3E_i} - \frac{1}{\varepsilon} - \frac{2E_i}{3\varepsilon^2}\right), \tag{5.16}$$

where $a_0 = 5.29 \times 10^{-11}\mathrm{m}$ is the Bohr radius, $R_y = 13.65$ eV is the Rydberg energy, and α

is a coefficient, for which $\alpha = 3.25$ is the suggested value. The cross section $\sigma(\varepsilon)$ is given in m^2. Due to the lack of data on C_2 and C_3, this model is also implemented to obtain the cross section for the stepwise ionization for molecular carbon. The stepwise ionization reaction rates are shown in Fig. 5.2.

Three-body recombination of ions is also accounted for in the model, for which the recombination rate is given by [37],

$$k_{rec} = 8.75 \times 10^{-27} T_{eV}^{-4.5}, \tag{5.17}$$

where the units of k_{rec} are in cm^6/s, which is applied to all ions. Dissociative recombination [37] of C_2^+ and C_3^+ is also accounted for in the model. The rate coefficient of dissociative recombination $C_2^+ + e \rightarrow C + C$ is provided up to electron temperature of 1.5 eV in Ref. [65] and is extrapolated. Since no data is available, the same rate coefficient is assumed for C_3^+ dissociative recombination.

5.2.3 Heavy species reactions

Chemistry between heavy species contributes to the transport of species concentration and momenta. Table 5.4 summarizes the heavy species reactions accounted for. Blottner's model is used for the rate coefficients of carbon related chemistry [66], which was developed to investigate the composition of the Martian atmosphere. The rate coefficients are given by,

$$k = \beta T^N \exp\left(-\frac{\Theta}{T}\right), \tag{5.18}$$

where β, N and Θ are constants given in Table 5.5, and T is the gas temperature in Kelvin. Note that the unit for β is $cm^3/(mol\ s)$ for reactions involving two reactants or $(cm^3/mol)^2/s$ for reactions involving three reactants.

Using Blottner's model, additional reactions involving ions are considered in the present model. Since no data is available for heavy species reactions involving ions, the rate coef-

Table 5.4: Chemical reactions between heavy species accounted for in the model.

Label	Reaction	Dissociation Energy
H1	$C_3 + C \rightarrow C_2 + C_2$	1.53 eV
H2	$C_2 + C_2 \rightarrow C_3 + C$	-1.53 eV
H3	$C_2 + M \rightarrow C + C + M$	6.08 eV
H4	$C + C + M \rightarrow C_2 + M$	-6.08 eV
H5	$C_3 + M \rightarrow C + C_2 + M$	7.61 eV
H6	$C + C_2 + M \rightarrow C_3 + M$	-7.61 eV
H7	$C_3 + C^+ \rightarrow C_2^+ + C_2$	1.89 eV
H8	$C_2^+ + C_2 \rightarrow C_3 + C^+$	-1.89 eV
H9	$C_3^+ + C \rightarrow C_2^+ + C_2$	1.41 eV
H10	$C_2^+ + C_2 \rightarrow C_3^+ + C$	-1.41 eV
H11	$C_2^+ + M \rightarrow C^+ + C + M$	5.72 eV
H12	$C^+ + C + M \rightarrow C_2^+ + M$	-5.72 eV
H13	$C_3^+ + M \rightarrow C^+ + C_2 + M$	7.12 eV
H14	$C^+ + C_2 + M \rightarrow C_3^+ + M$	-7.12 eV
H15	$C_3^+ + M \rightarrow C + C_2^+ + M$	7.51 eV
H16	$C + C_2^+ + M \rightarrow C_3^+ + M$	-7.51 eV
	(M: all heavy species)	

Table 5.5: Constants of the rate coefficients for carbon reactions $k = \beta T^N \exp(-\Theta/T)$ following Blottner's model, shown in Eq. (5.18). The labels for the reaction types shown correspond to the labels in Table 5.4.

Reaction	β	N	Θ
H1, (H7, H9)	1.7×10^9	1.5	1.958×10^4
H2, (H8, H10)	5×10^{11}	0.5	3.02×10^3
H3, (H11)	4.5×10^{18}	-1	7.093×10^4
H4, H6, (H12, H14, H16)	1×10^{16}	-0.5	0
H5, (H13, H15)	1.6×10^{16}	1	8.748×10^4

ficients for neutral reactions are assumed, since the dissociation energy is close [67]. For reactions H7-H16 in Table 5.4, the same reactions involving neutral atoms are considered. Hence, the same constants shown in Table 5.5 are used.

5.3 Electron Transport & Electric Field

Due to the high collisionality in an atmospheric pressure plasma, and because the electron characteristic time is much shorter than the heavy species characteristic time [19], the transient term and the inertial term are dropped from the momentum equation (Eq. (5.8)) for the electrons. This leads to the 1D drift-diffusion approximation:

$$0 = -\frac{\partial p_e}{\partial x} - en_eE + F_e, \tag{5.19}$$

where p_e is the electron pressure and F_e accounts for the collisional drag for electrons. In this model, two collisional drag terms are considered: Krook operator for collisions with neutral gas (a feature of partially ionized plasmas) [10] and Braginskii's model for collisions with charged species (a feature of fully ionized plasmas) [6, 9]. Thus, the collisional drag can be written as,

$$F_e = -0.71n_e e\nabla T_{eV} - 0.51m_e n_e \nu_{m,ei}(u_e - u_i) - m_e n_e \nu_{m,en}(u_e - u_n),$$

where ν_m is the momentum transfer collision frequency, with subscripts *en* and *ei* denoting electron-neutral and electron-ion collisions, respectively, and u_e, u_n, and u_i are the electron, neutral, and ion bulk velocities. The first term in Eq. (5.20) is the thermal force, the second term corresponds to the momentum exchange due to Coulomb collisions with ions, and the last term is friction from collisions with neutrals. Note that the right hand side of the ion momentum equation, see Eq. (5.10), also employs the thermal flux and Coulomb collision momentum exchange [6]. Using this definition for the external forces and rearranging the terms in Eq. (5.19) yields the electron flux, given by,

$$\Gamma_e = -n_e\mu_e E - \mu_e \frac{\partial p_{eV}}{\partial x} - \Delta\Gamma_{e,mod}, \tag{5.20}$$

where $\mu_e = e/(m_e \nu_{m,e})$ is the non-magnetized electron mobility, $p_{eV} = n_e T_{eV} = p_e/e$ is the electron ideal gas pressure, and $\Delta\Gamma_{e,mod}$ is the remaining terms, given by,

$$\Delta\Gamma_{e,mod} = n_e \left(u_n \frac{\nu_{en}}{\nu_{m,e}} + 0.51 u_i \frac{\nu_{ei}}{\nu_{m,e}} - 0.71 \mu_e \frac{\partial T_e}{\partial x} \right),$$

where $\nu_{m,e} = \nu_{m,en} + 0.51 \nu_{m,ei}$ is the total momentum transfer collision frequency for electrons. Note that $\Delta\Gamma_{e,mod} = 0$ and $\nu_{m,e} = \nu_{m,en}$ correspond to the electron flux in the drift-diffusion approximation obtained from Krook's drag and $u_n \approx 0$.

Based on the assumption that only singly charged ionization takes place, i.e., no multiply charged ions, the current conservation can be written as,

$$j_i + j_e = j_D, \tag{5.21}$$

where $j_i = e n_i u_i$ is the ion current density, $j_e = -e n_e u_e$ is the electron current density, and j_D is the net current density. Here, $j_D = I_d/A$ where I_d is the total discharge current and A is the area of the arc core using a quasi-1D assumption. Then, from Eqs. (5.20) and (5.21), the electric field can be calculated as,

$$E = \frac{1}{n_e \mu_e} \left(\frac{j_D - j_i}{e} - \mu_e \frac{\partial p_{eV}}{\partial x} + \Delta\Gamma_{e,mod} \right). \tag{5.22}$$

The potential drop in the bulk plasma can then be calculated as $V_{pl} = -\int E dx$.

5.4 Energy Equations

In the presence of large collisionality, the different temperatures will eventually equilibriate, which may approach thermal equilibrium. That said, this is not implicitly assumed in the model, and separate energy equations are solved, with the collisionality of the model potentially allowing for equilibriated temperatures. Here, three separate energy equations are solved, one for electrons, one for helium, and one for all the carbon species, accounting for collisions among the species.

5.4.1 Electron energy equation

The 1D electron energy equation is given as,

$$\frac{3}{2}\frac{\partial(n_e k_B T_e)}{\partial t} + \frac{\partial}{\partial x}\left(\frac{5}{2}n_e k_B T_e u_e + h_e\right) = -e n_e u_e E - Q_{el,en} - Q_{el,ei} - Q_{inel}, \tag{5.23}$$

where h_e is the conductive heat flux, $-e n_e u_e E$ is the Joule heating, $Q_{el,en}$ and $Q_{el,ei}$ are the energy transfer through elastic collisions with neutrals and ions, and Q_{inel} is the energy transfer through inelastic collisions. Here $h_e = -\kappa_e \nabla T_e$, where the electron thermal conductivity κ_e is given by [20],

$$\kappa_e = \frac{2.4}{1 + \nu_{ei}/(\sqrt{2}\nu_e)}\frac{k_B^2 n_e T_e}{m_e \nu_{m,e}},$$

where ν_{ei} is the electron-ion Coulomb collision frequency summed over all ions, and ν_e is the total electron collision frequency with all heavy particles. It must be noted that the factor $2.4/[1 + \nu_{ei}/(\sqrt{2}\nu_e)]$ is an approximation, and that in the limit of a fully ionized plasma, when $\nu_e \rightarrow \nu_{ei}$, the factor becomes 1.4. This contrast with the value given 3.2 given by Chapman-Enskog's approach for fully ionized plasma [20]. The energy exchange due to elastic collisions can be written as [20],

$$Q_{el} = n_e \sum_s \frac{3}{2} k_B (T_e - T_s)\frac{2m_e}{m_s}\nu_{s,e},$$

where T_s is either the heavy species temperature or the temperature of helium, and $\nu_{s,e}$ is taken as the Coulomb collision frequency for elastic collisions with ions and as hard sphere collision frequency for elastic collisions with neutrals. The electron-neutral energy transfer is given by the form $Q_{el,en} = Q_{el,eHe} + Q_{el,eC}$, where subscripts eHe and eC correspond to electron-helium and electron-carbon collisions. The energy transfer term due to inelastic collisions is given by $Q_{inel} = \sum_j n_e \nu_j \Delta\varepsilon_j$, where ν_j is ionization or excitation frequency, and $\Delta\varepsilon_j$ is the ionization or excitation energy, summarized in Table 5.3.

5.4.2 Heavy species energy equations

The model solves two separate energy equations for the heavy species: one for helium and the other for carbon species. The helium energy equation is given by

$$\frac{3}{2}\frac{\partial(n_{He}kT_{He})}{\partial t} + \frac{\partial}{\partial x}\left(\frac{5}{2}n_{He}k_BT_{He}u_{He} + h_{He}\right) = Q_{el,eHe} - Q_{el,HeC}, \tag{5.24}$$

where $h_{He} = -\kappa_{He}\nabla T_{He}$ is the conductive heat flux of the helium atoms and $Q_{el,HeC}$ is the energy exchange between helium and carbon, obtained assuming hard-sphere collisions.

The carbon energy equation includes ground, excited, and ionized states of carbon atoms and molecules. The internal energy of all carbon species is assumed to be that of monoatomic species for simplicity, whereas the specific heat capacities of polyatomic species are different due to the internal energy modes such as rotational and vibrational excitation [68]. Note that the energy equation will be independent of the specific heat if convective heat flux is negligible due to the small bulk velocity. Considering the total density of carbon species, n_h, to be the sum of all carbon species, the carbon energy equation is given by,

$$\frac{3}{2}\frac{\partial(n_hk_BT_c)}{\partial t} + \frac{\partial}{\partial x}\left(\frac{5}{2}n_hk_BT_cu_h + h_c\right) = en_iu_iE + Q_C, \tag{5.25}$$

where $h_c = -\kappa_c\nabla T_c$ is the ion conductive heat flux, the thermal conductivity κ is given from the data in Refs. [69] and [70], and Q_C accounts for the energy exchange that involves the carbon species, which can be written as $Q_C = Q_{el,eC} + Q_{el,HeC} + Q_{exo} + Q_{recomb}$. The term Q_{exo} accounts for the energy lost or gained by the carbon through exothermic and endothermic chemical reactions in Table 5.4, and Q_{recomb} refers to the energy gained from dissociative-recombination reactions.

6. ANODE & CATHODE SHEATH MODEL

Since the surface temperature of the anode determines the ablation rate of the carbon species, it is important to self-consistently model the heat flux balance towards the electrodes. In this model, the non-neutral regions in the anode and cathode sheaths are not explicitly solved due to the use of the quasineutral assumption. However, the current and heat conditions are considered between the sheath edge and electrodes to evaluate the sheath potential drop and the electrode temperatures.

6.1 Anode Module

Depending on the current balance at the sheath edge, the sheath potential can be either *negative*, accelerating ions towards the wall and repelling electrons, or *positive*, accelerating electrons to the wall and repelling ions. When the electron thermal flux at the anode sheath edge is small compared to the electron current required at the anode surface, a positive anode sheath will be formed. In order for the plasma discharge to be sustained, more ionization needs to take place within the sheath, which can be achieved by electrons accelerating towards the anode. Their increased energy leads to ionization, and those new ions will be accelerated to the plasma. This was hypothesized as a source of enhanced ablation in Refs. [71], [41], and [44].

6.1.1 Anode sheath potential

The sign of the sheath potential depends on the electron current density required at the sheath edge in comparison to the theoretically maximum electron current density:

$$j_{e_0} = \frac{1}{4} e n_e \bar{C}_e, \tag{6.1}$$

where $\bar{C}_e = \sqrt{8 k_B T_e / \pi m_e}$ is the electron thermal velocity, which corresponds to a half-Maxwellian distribution without any sheath potential. For a negative sheath, the electron

current density at the wall can be written as $j_e = j_{e_0} \exp(U_a/T_e)$, where U_a is the anode sheath potential and $U_a < 0$. The electron current density can also be written as $j_e = j_D - j_i$ from Eq. (5.21). Hence, for a negative sheath,

$$U_a = \frac{k_B T_e}{e} \ln\left(\frac{j_D - j_i}{j_{e_0}}\right). \tag{6.2}$$

When $j_{e0} < j_D - j_i$, a positive sheath must form as the electrons at the sheath edge are not sufficient to satisfy the required electron current. Since the ion current in the positive anode sheath is typically much smaller than the electron current, it can be approximated that the electron current to the wall equals the discharge current, $j_e = j_D$. As a simplification, in such cases, the anode sheath potential is set to be $U_a = 0$.

6.1.2 Anode heat balance

The heat flux balance at the anode can be given by

$$0 = q_{pl,e} + q_{pl,i} + j_D \Phi_W - \Delta H \mathcal{F}_{\text{evp}}(T_a) - \varepsilon_a \sigma_{SB} T_a^4 - \kappa_a \frac{dT_a}{dx}, \tag{6.3}$$

where T_a is the anode temperature, $q_{pl,e}$ and $q_{pl,i}$ are the plasma heat flux contributions from the electrons and the ions, respectively, Φ_W is the material work function, ΔH is the latent heat of vaporization of graphite, T_a is the anode temperature, ε_a is the radiation trapping coefficient, σ_{SB} is the Stefan-Boltzmann constant, and κ_a is the graphite conductivity. The term $\Delta H \mathcal{F}_{\text{evp}}(T_a)$ is the heat lost to the vaporized graphite particles. While some of the evaporated material could deposit itself onto the anode, the deposit is likely significantly small, mainly due to the flux of the evaporated material. Thus, it is assumed that the sticking coefficient of the neutral particles at the anode is small. The evaporation rate is taken from fitted experimental data [49]. For the radiative heat flux, it is considered that ε_a is a radiation trapping coefficient accounting for radiation exchanged between the anode and cathode, which is further discussed later.

The heat flux from the plasma to the anode due to the electron current is given by,

$$q_{pl,e} = \begin{cases} j_e(2T_e) & \text{if } U_a < 0 \\ j_e(2T_e + KE) & \text{if } U_a \geq 0 \end{cases} \tag{6.4}$$

where $KE = 0.5 m_e u_e^2 / e$ corresponds to the kinetic energy of the electrons, which is deposited onto the anode as the electrons get accelerated and bombard its surface, for a positive sheath. The negative sheath case corresponds to the heat flux considering a half-Maxwellian [7]. The heat flux due to the ion current to the anode can be written as,

$$q_{pl,i} = \begin{cases} |j_i|(2T_g + |U_a| + E_i) & \text{if } U_a < 0 \\ 0 & \text{if } U_a > 0 \end{cases} \tag{6.5}$$

where, in the case of a negative sheath, the ions will bombard the anode wall and lose their energy through wall recombination. In the positive anode sheath case, the ions are repelled towards the plasma, and it is assumed that there are no ions that reach the anode.

6.2 Cathode Module

In an ablating carbon arc, a carbon deposition occurs on the surface of the cathode. Experiments show that the arc is attached to the carbon deposit, which grows in time [1]. The cathode deposit area plays a role in determining the heat balance and the temperature of the gas at the cathode, and different ablation modes lead to differently sized deposit areas [42].

6.2.1 Cathode temperature

It is considered that electron emission from the cathode deposit is due to thermionic electron emission, given by the Richardson-Dushman equation:

$$j_{emit} = \mathcal{A}_{RD} T_c^2 \exp\left(-\frac{e\Phi_W}{k_B T_c}\right), \tag{6.6}$$

where j_{emit} is the emitted electron current density, $\mathcal{A}_{RD} = 1.20173 \times 10^6$ A/m^{2}K^2 is the Richardson-Dushman constant, and T_c is the cathode deposit temperature. It is assumed that the sheath is not space charge limited [16] and the Schottky effect is negligible[34].

The emitted electron current density is calculated as $j_{emit} = I_{emit}/A_d$, where A_d is the deposit area and I_{emit} is the emitted electron current. From the current condition in Eq. (5.21), $I_{emit} = (j_D - j_i)A$, where A is the plasma arc area. Thus, $j_{emit} = (j_D - j_i)A/A_d$, and Eq. (6.6) becomes a function of two variables, T_c and A_d.

6.2.2 Cathode sheath potential

Another relation to consider is the cathode heat balance which is used to find the cathode sheath potential, U_c. Here, it is assumed that the area of the bulk plasma up to the cathode sheath edge is constant while the cathode deposit has a different size. Although the bulk plasma in an actual arc discharge is multidimensional so that the area of the arc core varies in space [42], the total current must be conserved across the bulk plasma and cathode in the present model. The bulk plasma components are multiplied by the core area, A, and the heat transfer on the material takes only the deposit area, A_d, into consideration.

The heat flux balance at the cathode can be written as,

$$0 = A\left[j_i(U_c + E_i) + e\Gamma_{ex}E_{ex} + \sum_j \Delta H_j \mathcal{F}_{m,j}\right] - A_d\left[\frac{A}{A_d} j_e \Phi_W + \kappa_c \frac{dT_c}{dx} + \varepsilon_c \sigma_{SB} T_c^4 + \Delta H \mathcal{F}_c(T_c)\right] \quad (6.7)$$

where T_c is the cathode deposit temperature, E_{ex} is energy released when excited species quench to the neutral state upon wall collision, $\mathcal{F}_m$ is the flux of carbon species from the bulk plasma to the cathode deposit, and $\mathcal{F}_c$ is the carbon flux that reevaporates from the cathode deposit. The terms multiplied by A correspond to the heat gained by the cathode deposit: $j_i(U_c + E_i)$ is the heat contribution of ion current; $e\Gamma_{ex}U_{ex}$ is the energy gained by the cathode due to wall quenching; and $\Delta H_j \mathcal{F}_{m,j}$ is the heat added by the deposited materials arriving

from the arc. The terms multiplied by A_d correspond to heat lost by the cathode deposit, which are the heat loss due to the emitted electrons from the cathode, heat conduction, losses due to radiation, and heat lost with re-evaporation of the cathode deposit. While it is proposed that reevaporation of cathode deposit materials occurs since the cathode temperature is high [42], such effects are self-consistently accounted for in the present model. This would result in an enhanced carbon density in the vicinity of the cathode.

6.2.3 Cathode deposit area

There are three variables to be solved at the cathode: the cathode temperature T_c, the cathode deposit area A_d, and the cathode sheath potential U_c. It can be seen from Eq. (6.7) that U_c can be determined for given A_d and T_c, which are related by Eq. (6.6). A third equation is needed to close the system and solve for the three variables. The formulation of the third equation is discussed below.

Depending on the values of A_d and T_c, the energy loss terms in Eq. (6.7) can vary. The energy loss terms in Eq. (6.7) can be written as,

$$f(T_c, A_d) = \kappa_c \pi (T_c - T_{ref}) \sqrt{A_d} + \varepsilon_c \sigma_{SB} T_c^4 A_d + \Delta H \mathcal{F}_c(T_c) A_d, \tag{6.8}$$

where the conduction length is assumed to be $L_c \sim \sqrt{A_d}$, and T_{ref} is assumed to be 1000 K. From Ref. [2], the temperature drops to such levels across a few millimeters into the cathode. However, the results in the present model are found not to be sensitive to the value of T_{ref}. It is hypothesized that the system finds the optimal values of A_d and T_c based on minimizing the total energy loss while satisfying the current condition, i.e., Eq. (6.6): T_c is small when A_d is large, while T_c is large when A_d is small. If the energy loss terms, i.e., Eq. (6.8), are large, that would mean that the cathode sheath potential U_c must be large to satisfy the energy balance, which requires more discharge power to the system. Hence, the hypothesis is that the cathode deposit size will be optimized by minimizing $f(T_c, A_d)$, which serves as the third condition needed to solve for the three variables.

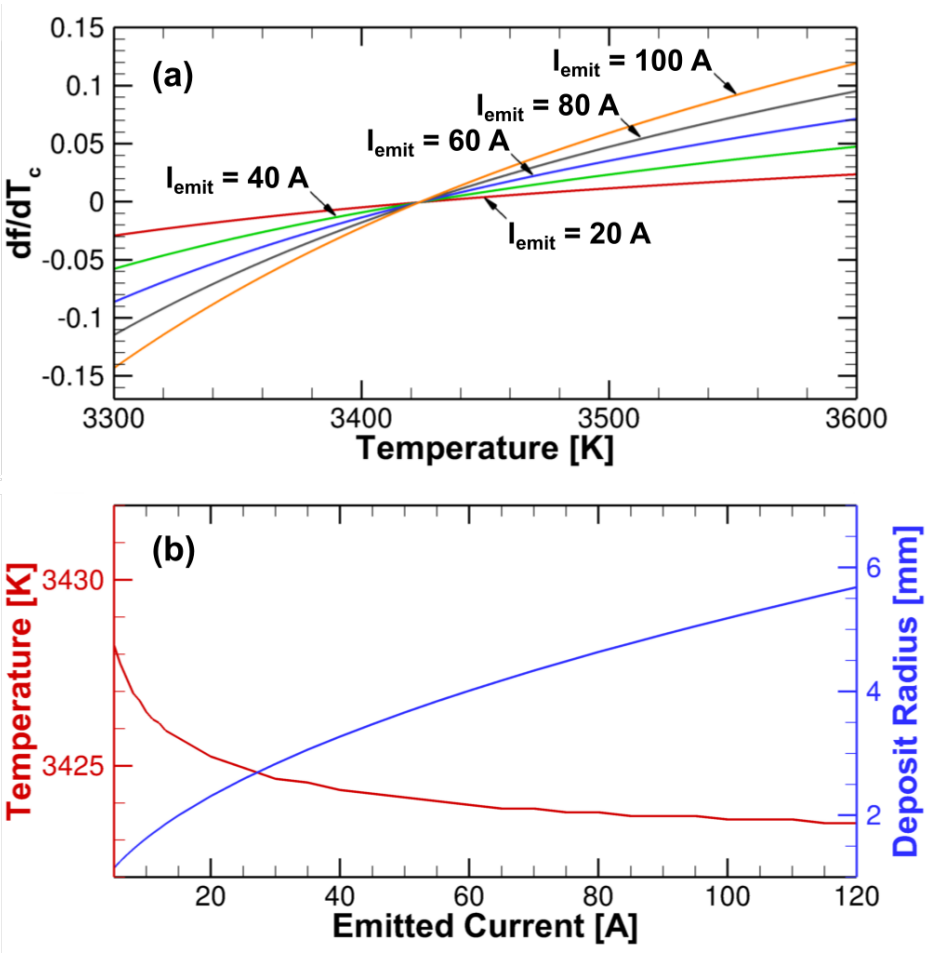

Figure 6.1: The cathode deposit area model. Plot (a) shows the derivative of the function f in Eq. (6.8) with respect to T_c to find the minimum f for different values of I_{emit}. Plot (b) shows the cathode temperature and cathode deposit radius for the optimized energy loss terms, when f is at minimum, i.e., when $df/dT_c = 0$.

The exact value of κ_c is not known; it can be assumed to be that of graphite, but the deposit contains nanotube structures that have much lower thermal conductivities compared to graphite [72]. The conductivity κ_c is assumed to be 0.1 W/m^2·s. The emissivity ε is taken to be 50%. The last term accounts for the heat loss due to reevaporation of carbon using Dushman's equation (see Eq. (5.7)) for the mass flux $\mathcal{F}_c$.

Figure 6.1 (a) shows the variation of the function f to find its minimum value for a given electron emission current I_{emit}. The minimum value of f, which gives the optimal values of A_d and T_c, corresponds to $df/dT_c = 0$. As a result of the assumed κ_c, the heat conduction

term is smaller than the radiation and evaporation terms. It is to be noted that the energy flux densities due to radiation and evaporation, namely $\varepsilon_c \sigma_{SB} T_c^4$ and $\mathcal{F}_c(T_c)$, respectively, increase as a function of T_c. However, the *net* energy flux has a contribution from the size of the cathode deposit A_d. It can be seen from Eq. (6.6) that $A_d \propto T_c^{-2} \exp(\bar{\Phi}_W / T_c)$, where $\bar{\Phi}_W = e\Phi_W / k_B$. The net energy flux due to radiation becomes a *decreasing* function with respect to an increasing T_c for $T_c < \bar{\Phi}_W / 2 \approx 23,000$ K. On the other hand, $\mathcal{F}_c(T_c)$ is proportional to $T_c^{-1/2} 10^{-B/T_c}$, as shown in Eq. (5.7). Multiplying by the deposit area A_d, the net energy flux due to evaporation is an *increasing* function with respect to an increasing T_c. This leads to the existence of a minimum value of f, which can be seen in Fig. 6.1 (a).

Figure 6.1 (b) shows the *optimal* cathode deposit temperature and radius that results in the minimum value of f as a function of emitted current, I_{emit}. The optimal T_c is approximately 3420 – 3430 K, and the deposit radius varies from 1 mm to 6 mm in the range of I_{emit} from 10 A to 120 A. Incorporating the minimal energy loss principle, Eq. (6.8), a curve fitting of the optimal A_d as a function of I_{emit} is precalculated. Once the deposit area is obtained, the Richardson-Dushman equation (Eq. (6.6)) is employed to find the cathode temperature, T_c. Both are then used in Eq. (6.7) to find the cathode potential U_c.

7. NUMERICAL MODEL & PARAMETERS

A finite volume method is used to solve the plasma model assuming a quasineutral plasma. Fluxes found at the cell interfaces are used to evaluate the quantities in the cell centers. The boundary conditions are assumed to be at the anode and cathode sheath edges.

7.1 Flowchart

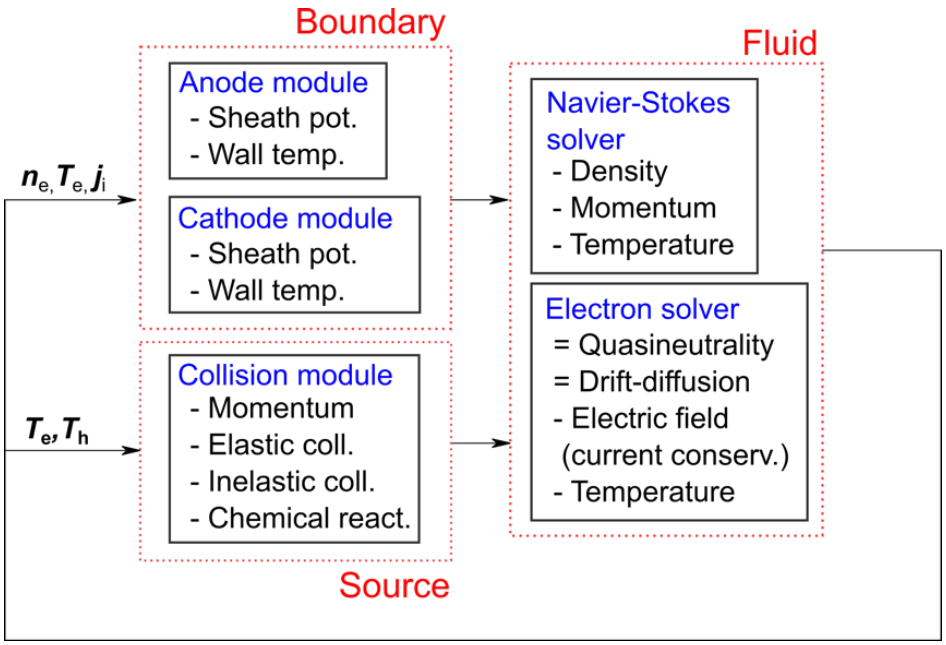

Figure 7.1: Flowchart of the numerical model, including the boundary, source, and fluid submodules.

Figure 7.1 provides a flowchart of the arc discharge model. The system is solved in a time explicit manner. For every time iteration, the number densities and momenta are calculated. The reaction rate coefficients, which depend on the temperatures, are updated, from which the source terms and collisional frequencies are calculated. The electron transport and electric field are then solved, making use of the collisional frequencies. Using the bulk plasma properties, the boundary conditions are accounted for, which provides the anode and the

cathode temperatures and effective sheath potentials. The mass flow rates due to evaporation at both electrodes are calculated using the surface temperatures, and the species mass and momentum fluxes within the domain are updated. The three energy equations for electrons, helium and other heavy species are then solved, quantities are updated to their cell center values from the cell interfaces, and the next time iteration begins.

7.2 Numerical Schemes

The inviscid components of the conservation of mass and momentum are solved using a finite volume Steger-Warming scheme [73], and the source terms are updated in a first-order manner. In this model, Monotonic Upwind Scheme for Conservation Laws (MUSCL) is used with a Koren limiter [74]. Further description of both Steger-Warming and MUSCL is provided in Appendix B. The energy equations are decoupled and are solved using a second order Crank-Nicolson scheme with a Thomas tridiagonal matrix solver. The former is described in Appendix C, and the latter is described in Appendix A.

7.3 Boundary Conditions

The variables to be solved for in this model are the number densities and velocities for all the species, totaling to eleven densities and eleven bulk velocities, as well as three temperatures: electron, carbon, and helium temperatures. The electric field is solved from the drift-diffusion approximation and current balance.

For the density, Neumann boundary conditions are applied for all the species. For the bulk velocity of neutral species, a reflective boundary condition is imposed at the anode. At the cathode, a sticking coefficient of 100% is assumed. In the case of a negative sheath, the ion bulk velocity is assigned a percentage of the Bohm velocity at the sheath edge. Otherwise, the ion bulk velocity at the boundary is set to zero.

A Neumann boundary condition is imposed based on the heat flux to the anode and the cathode for the electron energy equation, Eq. (5.23), and Dirichlet boundary conditions for the temperatures are imposed at the anode and the cathode for the heavy species equations,

e.g., Eqs. (5.24) and (5.25). The electrode temperatures are found using Newton's method, applied to Eqs. (6.3) and (6.6). The cathode sheath potential is solved using the bisection method.

7.4 Numerical Parameters

The numerical parameters used in the model are as follows. The number of spatial cells is 100; the number of time steps is 2.0×10^6; spatial domain size is 2.0 mm; total simulation time is 5.0×10^{-4} s; baseline arc core radius $r = 6.0$ mm; baseline total current $I_d = 60.0$ A. Radial diffusion loss is accounted for in order for the deposition rate to be smaller than the evaporation rate, which was observed in experiments [1]. It is assumed that the arc core dimension is equal to the anode diameter, since the anode is often ablated uniformly. Although anode attachment instability is reported in experiments [75], the multidimensional dynamic phenomena are neglected due to the use of a 1D model.

The main input parameters varied are the anode diameter and the total current, in order to investigate the two modes of ablation observed in experiments [1, 2]. The former is varied from 6 mm to 16 mm, all tested at 60 A. The latter is varied from 20 A to 120 A for an anode diameter of 12 mm. The model's sensitivity is tested for three components: the electron drag F_e in the electron transport equation, the ion Bohm velocity factor ζ accounting for a high pressure environment, and the gas temperature at the anode sheath edge $T_{g,a}$. The numerical results are compared to experimental results.

8. RESULTS & DISCUSSION

8.1 Transition between High & Low Ablation Modes

Figure 8.1 shows the mode transition between high and low ablation modes. Here, the emissivity ε, i.e., the radiative heat loss from the electrode surfaces, is varied. The experimental data shown are from Vekselman et al. [1], and Ng and Raitses [2]. Due to the proximity of the electrodes to each other and their high surface temperatures, radiative heat exchange could take place between the two. Heat being radiated from the anode surface is absorbed by the cathode and vice versa, effectively leading to radiative heat being trapped within the system of the two, while the remainder is emitted to the surrounding, e.g., vacuum chamber. The radiation trapping rates are modeled using ε_a and ε_c in Eqs. (6.3) and (6.7). The factor ε can be considered an effective emissivity, with a smaller value signifying less heat radiated outside of the plasma discharge and more heat exchanged between the electrodes.

8.1.1 Evaporation rate

Figure 8.1 (a) shows the results for different effective emissivities ε while varying the total current, keeping the anode diameter constant at 12 mm. The numerical results show a qualitative agreement with experimental results obtained by Vekselman et al. [1]. Although a different anode diameter is used in the experiments, it was reported in Ref. [1] that there is a plasma *bulb* of C_2 molecules that forms between the electrodes, which indicates that the effective arc plasma diameter is larger than the electrodes in some cases. Additionally, it can be seen from the experimental data that there is a slight enhancement in the evaporation rate above 55 A. From the numerical results, this enhancement can be explained by the decreased emissivity of the radiative heat flux within the electrodes. As the ε decreases, the effective heat loss from the anode surface due to radiation decreases as well. This raises the temperature of the anode surface, leading to enhanced evaporation.

Figure 8.1 (b) shows the evaporation rates when varying the anode diameter with a total

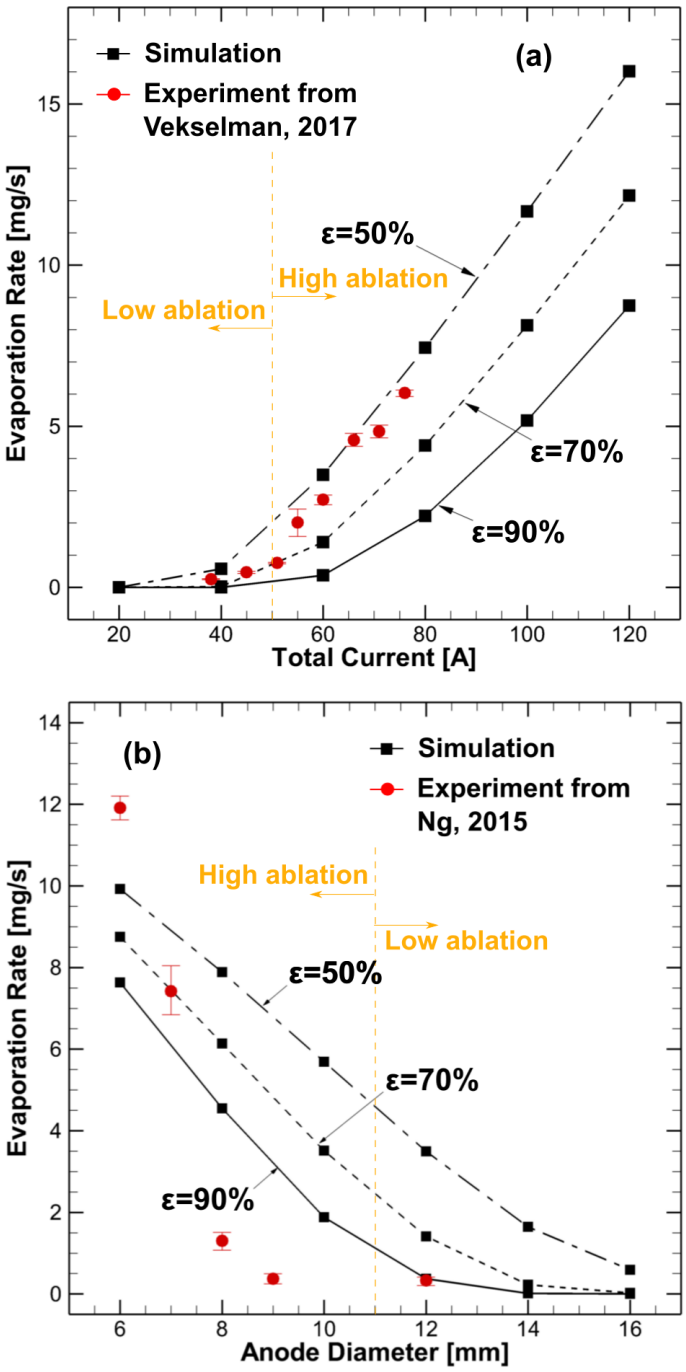

Figure 8.1: Evaporation rates against (a) total current, compared to experimental data from Vekselman et al. [1], and (b) anode diameter, compared to experimental data from Ng and Raitses [2], for $\varepsilon = 50\%, 70\%, 90\%$. The dashed orange line indicates the transition from low to high ablation modes, which is arbitrarily chosen to help guide the readers.

current of 60 A, compared to earlier experimental results from Ng and Raitses [2]. It can be seen from the experimental data that the anode temperature is likely to be constant between the 9 mm and 12 mm diameter cases. The discrepancy between the simulation and experiments may be due to the cathode deposit area model. In Fig. 8.1 (a), the cathode deposit area increases with increasing I_d, which is consistent with the experimental observation. On the other hand, the discharge current is kept constant while the anode diameter is varied in Fig. 8.1 (b). A higher ablation mode at smaller anode size indicates that the cathode deposit rate is also high, which most likely results in a large deposit area. However, simultaneously, it is likely that the ion current increases for a smaller anode diameter case, which would yield a smaller electron emission current. This poses an inconsistency between the present simulation results and the experimental observation.

The numerical results suggest that the cathode deposit model is a reasonable model when the total current varies since the trend is that the higher total current, the higher ablation rate, and the larger deposit area. For the cases where the anode diameter is decreased for a fixed total current, the current density and the cathode deposit area grow due to the enhanced ablation rate, but the arc attachment to the deposit may be restricted to a smaller area. This is contradictory to the proposed cathode deposit model, where the deposit area is assumed to be equal to the plasma attachment area at the cathode. Therefore, the plasma-cathode interaction may play an important role in the mode transition, and a multi-dimensional simulation that accounts for the growth of the cathode deposition layer and arc attachment is needed.

While the results shown plot the evaporation rates against the total current and the anode area separately, it is important to study the variation of the evaporation rate with the *current density*. In this model, the current density is indirectly varied by changing the total current and the anode diameter. Since the current density varies linearly with the current and squarely with the diameter, the effects of a varying current density are not properly captured. Comparing numerical and experimental results using the current density as the metric could provide further insight into the operation of the arc discharge. That is reserved for future

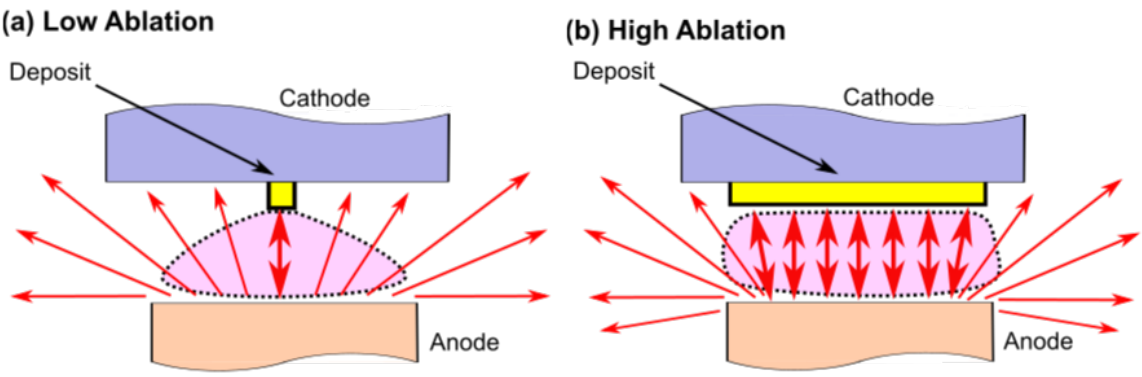

Figure 8.2: Schematic showing the difference in radiative heat flux between the cathode and anode for (a) small and (b) large cathode deposit areas. The shaded pink region illustrates the time-averaged arc discharge region.

work.

8.1.2 Radiative heat transfer between electrodes

In this model, it is hypothesize that the radiative heat transfer from the electrodes plays an important role in the arc discharge. Although it will depend on discharge characteristics (e.g., power, voltage, and current) and electrode geometry, here the sensitivity of radiative heat transfer is investigated by varying ε_a and ε_c in the energy balance equations of the anode and cathode, respectively. Furthermore, $\varepsilon_a = \varepsilon_c = \varepsilon$ is assumed.

Figure 8.2 shows two schematics of the arc discharge for low and high ablation modes. In the low ablation case, the cathode deposit is typically much smaller than the anode area, as shown in Fig. 4 of Ref. [1] and Fig. 3 of Ref. [2]. In the former study, the total current is varied between 35 A and 80 A with a fixed anode diameter of 6.5 mm, while the anode diameter is varied between 6 mm and 12 mm keeping the discharge current constant at 65 A in the latter study. Both configurations operated with an inter-electrode gap of 1-2 mm.

In the low ablation mode, the cathode deposit area is only a fraction of the anode area. Both the anode surface and the deposit surface are radiating in all directions. Some of the radiation is exchanged between the two electrodes, and the heat is trapped within the system.

However, the radiative heat flux from the cathode deposit to the anode is small, as the cathode deposit is much smaller than the anode size. The radiation transfer between the two electrodes is thus small, and it can be considered that the radiative heat flux escapes outside of the arc. Hence, the *net* radiation heat loss from the surface, specified by ε, can be considered large.

For the high ablation mode, the deposit area becomes larger and approaches the size of the anode area for both the varying anode diameter case and the varying total current case. In Fig. 3 of Ref. [2], it can be seen that the ablation is so large that the cathode deposit surpasses the area of the anode. More heat gets exchanged between the two electrodes through radiation, trapping more of the radiative heat within the system. It is to be noted that the radiation from the bulk plasma to the surrounding, i.e., spontaneous emission from the excited states is explicitly modeled via the conservation of mass, while the radiative heat transfer between the arc plasma and electrodes are not considered. In this numerical model, more radiative heat trapped between the electrodes correlates to a lower ε. Particularly, the cathode deposit temperature from our calculation is predicted as $\sim$ 3400 K, as shown in Fig. 6.1. If the cathode deposit is large, a large amount of the radiative heat flux can travel from the cathode to the anode, leading to an enhanced ablation rate.

The results shown in Fig. 8.1 seem to support the hypothesis regarding the radiative heat transfer. The numerical results using a larger value of ε, i.e., more radiative heat being lost from the system, show excellent agreement with experimental results in the low ablation regime. As the arc transition to the high ablation mode, the numerical results with lower values of ε, i.e., more radiative heat remaining in the system, coincide with the experimental results. This can be taken as an indication that the radiative heat transfer plays a vital role in dictating the ablation mode of the arc.

8.1.3 Cathode drop & discharge voltage

Figures 8.3 and 8.4 show the voltage as it varies with total current and anode diameter, respectively. In the numerical model, the total current is preset for each run and the discharge voltage can fluctuate. The total discharge voltage is not sensitive to ε, particularly in the

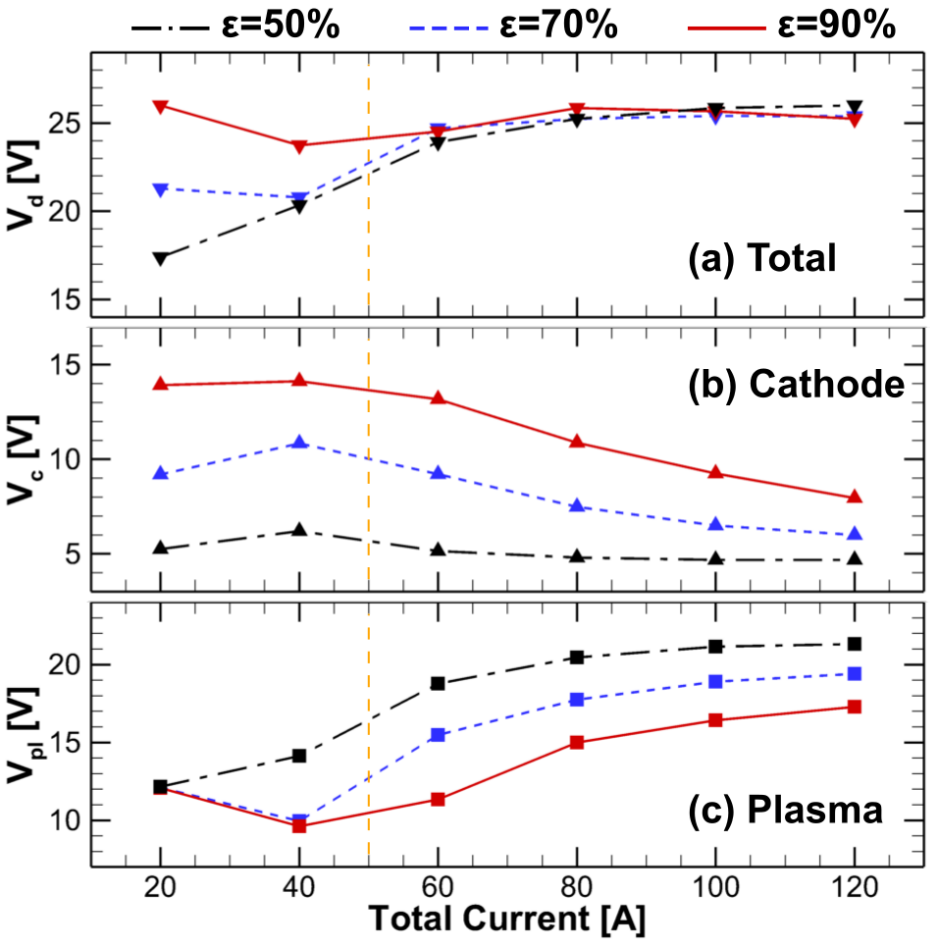

Figure 8.3: Voltage while varying total current for a given anode diameter of 12 mm and various radiative heat loss from the electrodes, ε: (a) total discharge voltage V_d, (b) cathode voltage V_c, and (c) plasma potential drop V_{pl}. The dashed orange line corresponds to the transition between ablation modes, as shown in Fig. 8.1.

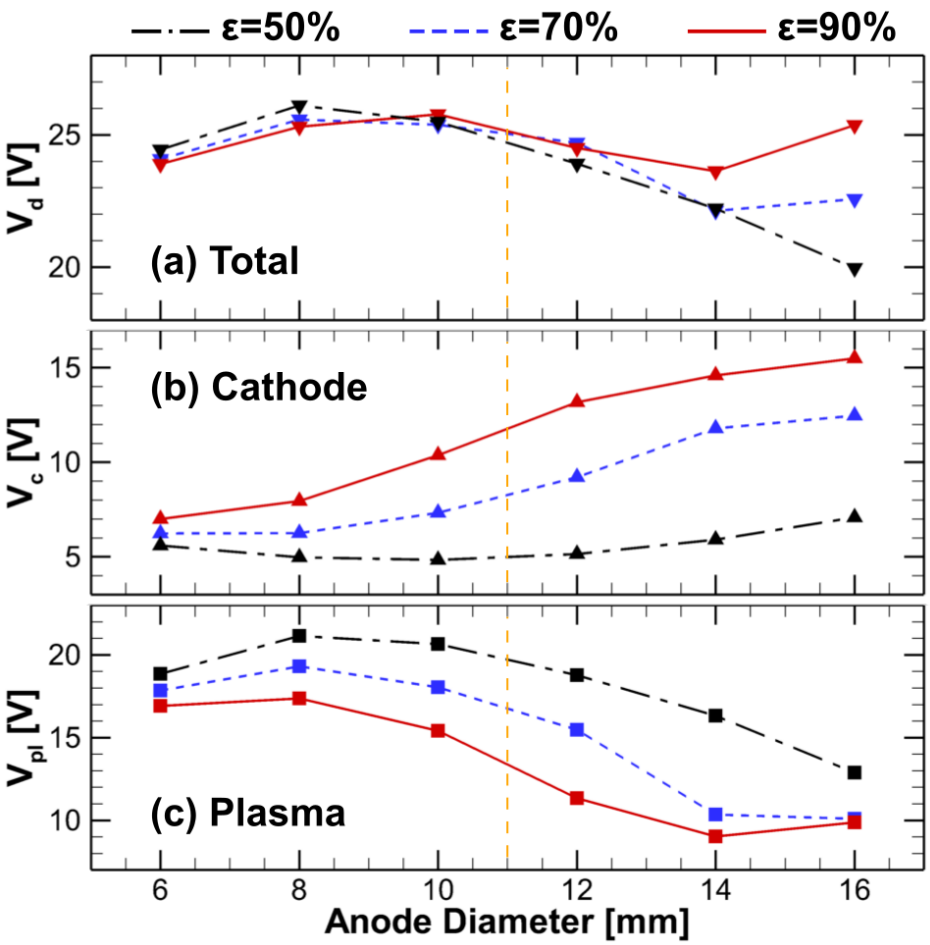

Figure 8.4: Voltage while varying anode diameters for a given total current of 60 A and various radiative heat loss from the electrodes, ε: (a) total discharge voltage V_d, (b) cathode voltage V_c, and (c) plasma potential drop V_{pl}. The dashed orange line corresponds to the transition between ablation modes, as shown in Fig. 8.1.

high ablation mode. The numerical results shown in Fig. 8.3 show excellent agreement with experiments, in which the total discharge voltage stays relatively constant at 25 V for varying total current [76, 2]. The discharge voltage is kept around 25 V particularly when $\varepsilon = 90\%$ in the low ablation mode. This supports the hypothesis of radiative heat exchange between electrodes, as shown in Fig. 6.1: for a low ablation mode when the cathode deposit is small, most of the radiative heat flux is lost to the surroundings, e.g., vacuum chamber, and a higher effective emissivity ε is expected.

The cathode voltage V_c increases with larger values of ε because the cathode sheath

potential must compensate for the energy lost due to radiative heat flux. With lower values of ε, the anode evaporation rate increases, leading to a higher plasma density. To sustain the plasma discharge, the electric field in the bulk discharge needs to be higher. Hence, the total potential drop, V_{pl}, increases. The cathode voltage V_c decreases in the high ablation mode because the convective heat due to the ions and neutrals is large, leading to a self-sustaining cathode that does not require acceleration of ions to heat the cathode. It is to be noted that the anode sheath potential is not shown because $U_a = 0$ for all cases in the present model, which could be due to the ion boundary condition at the anode. It is assumed that ion flux is zero at the anode when a positive anode sheath forms, but there can still be finite ion flux approaching the anode surface considering the ion velocity distribution.

8.2 Plasma Properties

The two modes of ablation change the composition and the behavior of the bulk plasma in the arc discharge. The model does not assume thermal, velocity, and chemical equilibrium as the conservation equations are solved for each species. Here, the deposition rate, number density, bulk velocity, and temperature are discussed.

8.2.1 Deposition rate at the cathode

Figure 8.5 shows the deposit rate density of each species on the cathode for the cases of 6 mm anode diameter (high ablation) and 12 mm anode diameter (low ablation) at 60 A. The results show the differences between the two modes, with the net deposition rate significantly dropping from 6.35 mg/s to 0.31 mg/s. In both cases, C_3 particles evaporate from the cathode deposit surface due to its high temperature and are re-deposited as C_3^*, after being excited by the electrons accelerated within the cathode sheath. As shown in Figs. 8.3 and 8.4, $V_c > 5$ V and the excitation energy of C_3^* is 3.06 V from Table 5.2, suggesting that such electronic excitation can occur within the cathode sheath. The dominant depositing species are C and C^+, followed by C_2 and C_2^*. The flux of C_3^* molecules to the cathode is large due to the high level of excitation in the vicinity of the cathode sheath. There is a stream of C_3 molecules

from the bulk discharge in addition to the C_3 molecules evaporating from the cathode, both of which get electronically excited and result in C_3^* flux toward the cathode deposit. This leads to a net deposit on the cathode.

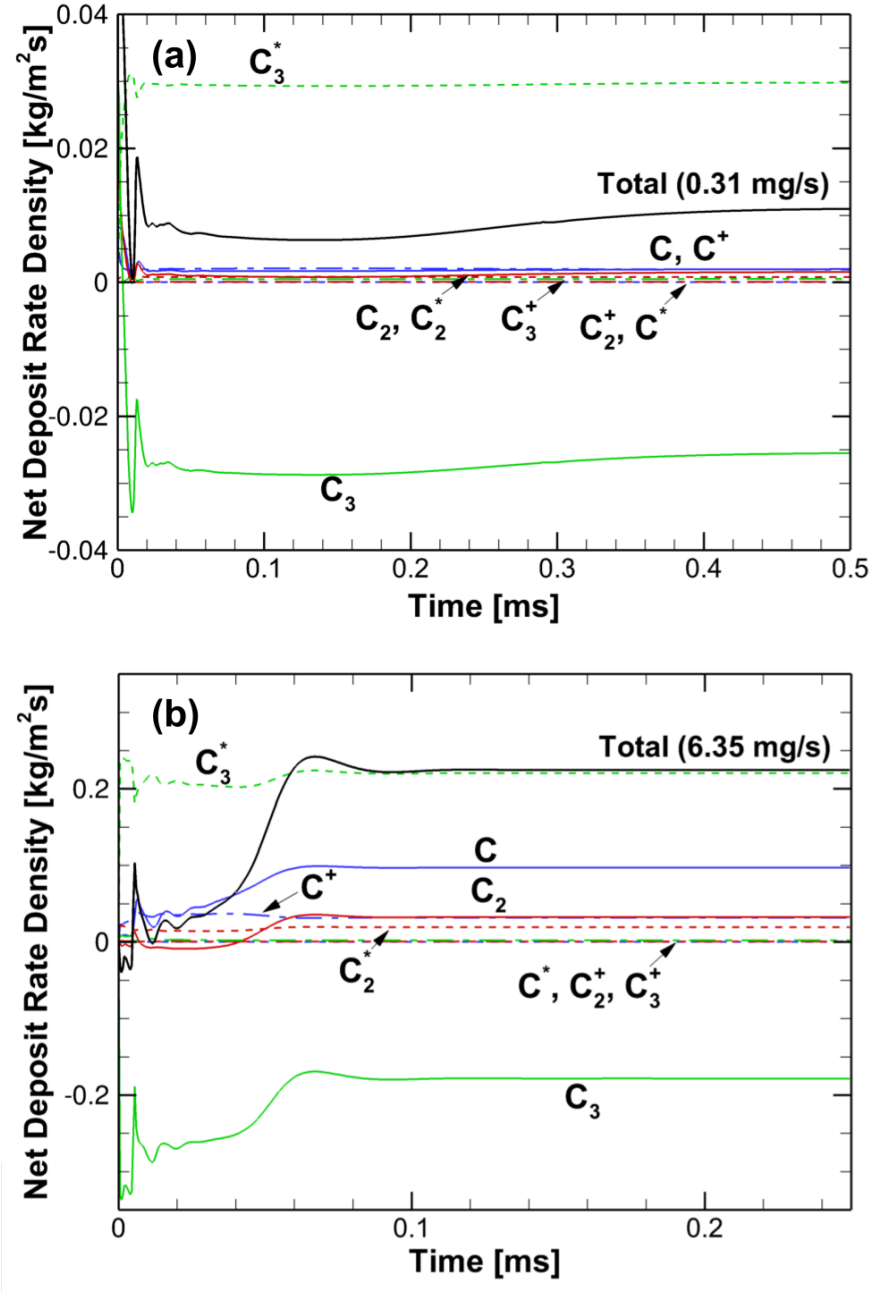

Figure 8.5: Deposition rate for (a) low and (b) high ablation modes, corresponding to r=12 mm and r=6 mm, at I=60 A. Negative deposition rate corresponds to evaporation of the material. The net deposition rate is shown in the solid black line.

For the low ablation mode, as shown in Fig. 8.5 (a),the deposit rate densities are approximately 0.03 kg/m^{2}s for C_3^*, -0.025 kg/m^{2}s for C_3, 0.002 kg/m^{2}s for C and C^+, and 0.001 kg/m^{2}s for C_2 and C_2^*. For the high ablation mode, shown in Fig. 8.5 (b), the deposit rate densities are 0.22 kg/m^{2}s for C_3^*, -0.18 kg/m^{2}s for C_3, 0.1 kg/m^{2}s for C, and 0.08 kg/m^{2}s for C_2 and C^+. The majority of the deposition is from C_3 for the low ablation mode, while it is from C in the high ablation mode because the gas temperature increases, causing C_3 and C_2 to dissociate.

8.2.2 Number density

Figure 8.6 shows the number density of each species in the bulk plasma. The density of C_2 near the anode agrees well with experimental data [71], which gives the density in the order of 10^{22} m^{-3}. The density of excited dicarbon, C_2^*, also shows good agreement with experimental data for the Swan bands [77], which gives the density in the order of 10^{21} m^{-3} for a carbon arc plasma at 65 A total current and 6 mm anode diameter that corresponds to high ablation mode as shown in Fig. 8.6 (b). Ion and electron densities are on the order of 10^{21} m^{-3}, one order of magnitude lower than experimental data [1], which are on the order of 10^{22} m^{-3} in the arc core. The discrepancy can be attributed to the fact that the arc core is constricted to an area smaller in the actual discharge than the anode area. The 1D limitation of the model cannot take that into account, and as such the higher density in the constricted arc is averaged out over the area of the anode, effectively leading to lower densities reported by the model. An energy-minimizing method that is arc temperature and density dependent can potentially be used to find the optimal current density for a given total current. The current density can then be directly used to evaluate the arc core area.

The elevated densities in the high ablation mode are to be expected, since more materials evaporate and become present in the arc core. It can also be seen that monoatomic carbon density becomes dominant over C_3 in the high ablation mode, resulting from an increased gas temperature which is discussed later.

Reaction H7 in Table 5.4 ($C_3 + C^+ \rightarrow C_2^+ + C_2$), one of the heavy species reactions, is the

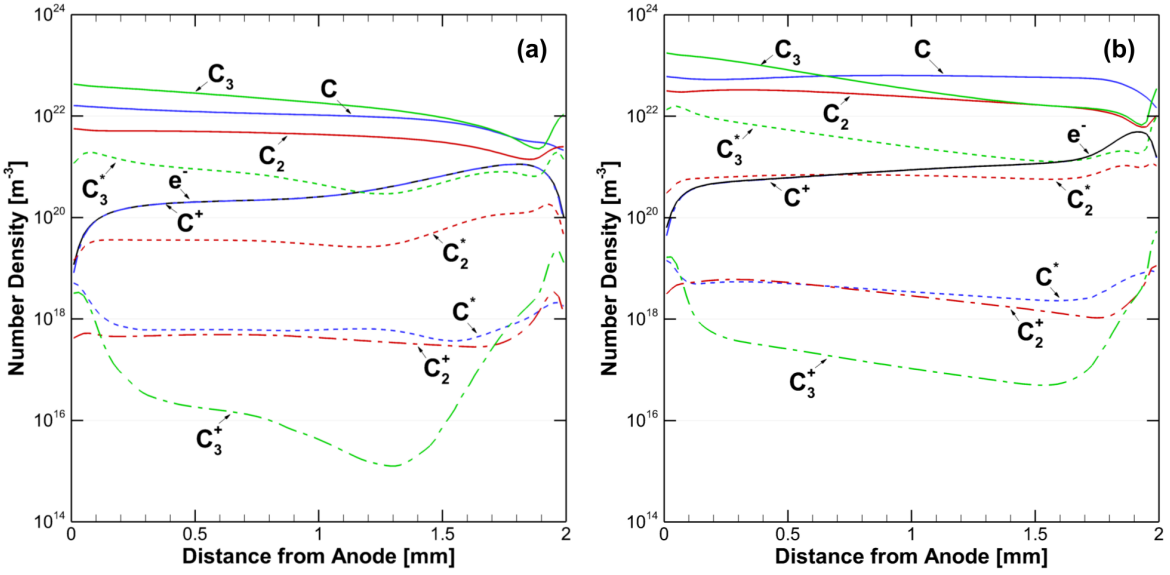

Figure 8.6: Species number density for (a) low (d = 12 mm) and (b) high (d = 6 mm) ablation modes at 60 A.

most dominant source for C_2^+ due to the high density of both C_3 and C^+. The most dominant source for C_3^+ is stepwise ionization. The most dominant loss mechanism for both C_2^+ and C_3^+, however, is dissociative recombination. At steady state, C^+ density is one to two orders of magnitude larger than C_2^+ density, and three to four orders larger than C_3^+ density. This is primarily due to the large dissociative recombination rate for the latter two [65].

8.2.3 Bulk velocity

Figures 8.7 and 8.8 show the bulk velocities of individual species. Instead of assuming a single bulk velocity for the carbon species, each momentum equation is solved separately. For both modes, the bulk velocities of neutral species are in equilibrium spatially except near the electrodes. In the low ablation mode, the bulk velocity of the heavy species is approximately 10-30 m/s. The momentum exchange due to Coulomb collisions between counterstreaming electrons and ions causes the ions to travel at such low speeds. Then, other elastic collisions involving heavy species (e.g., ion-neutral, neutral-neutral) contribute to further momentum exchange between ion and neutral species, which results in local velocity equilibrium. In the

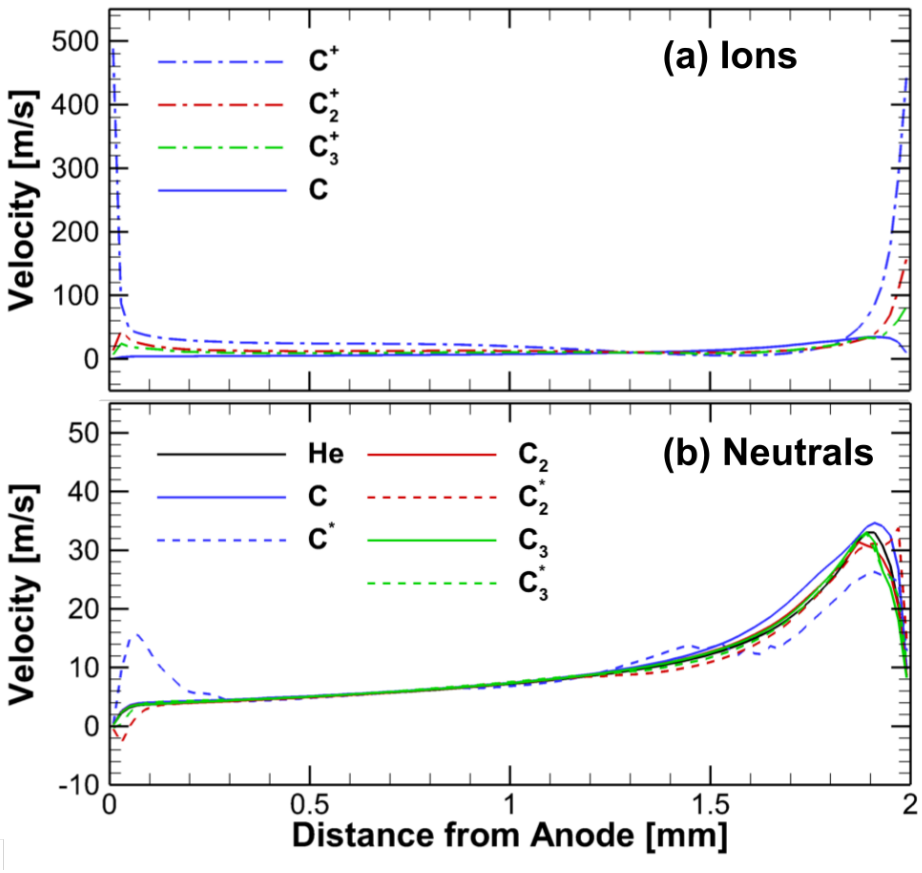

Figure 8.7: Bulk velocity for (a) ions and (b) neutral particles for a low ablation mode (d = 12 mm, 60 A).

high ablation mode, the bulk velocity varies from 20 m/s to 200 m/s, which primarily results from the increase in ion bulk velocity due to larger potential drop (V_{pl}) within the bulk plasma in comparison to the low ablation mode. At the cathode sheath edge, it is assumed that the ion velocities accelerate to 10% of the Bohm velocity. As such, an electric field sets up near the cathode presheath, accelerating the ions toward the cathode sheath edge. As the ion velocities increase, other species are accelerated as they approach the cathode via collisions. In the high ablation mode, high velocities ($\sim$ 200 m/s) near the cathode can be seen in Fig. 8.8 (b). Such axial particle flux can lead to the convection of particles in the radial directions, reported in 2D simulations [45]. Evaporated materials from the cathode deposit increase the density of carbon species near the cathode, which leads to the decreased bulk velocity seen

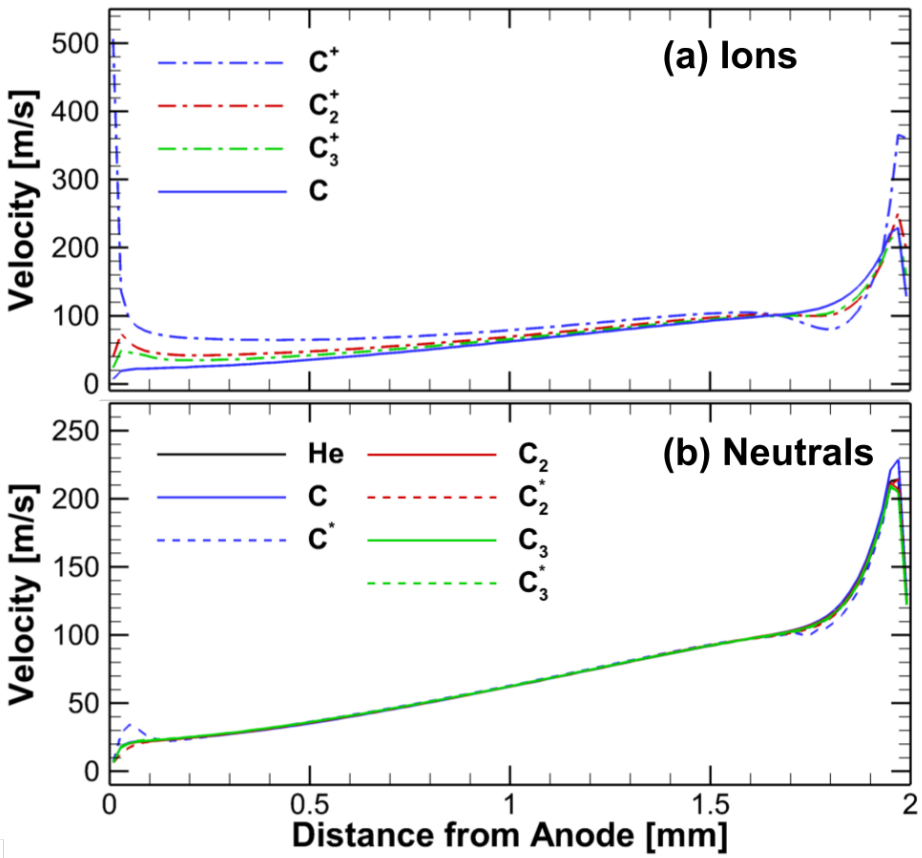

Figure 8.8: Bulk velocity for (a) ions and (b) neutral particles for a high ablation mode (d = 6 mm, 60 A).

for neutrals.

The ion velocity is also large close to the anode, moving away from it, and that is due to the formation of a positive sheath. This phenomenon could potentially be a numerical artifact due to the ion boundary condition in the bulk plasma model. A negative sheath could be formed when the plasma density is larger near the anode sheath, which can occur if the arc core was more constricted. It is hypothesized in Ref. [44] that the anode sheath transitions from a negative sheath to a positive sheath to explain the enhanced anode ablation. In the present simulation, a positive sheath is always observed due to the current balance. It is likely that Eq. (6.5) is too restrictive a condition, because hot ions (on the order of 3000 K) have a thermal speed of 1500 m/s for carbon, indicating that ion flux can still be non-zero even with

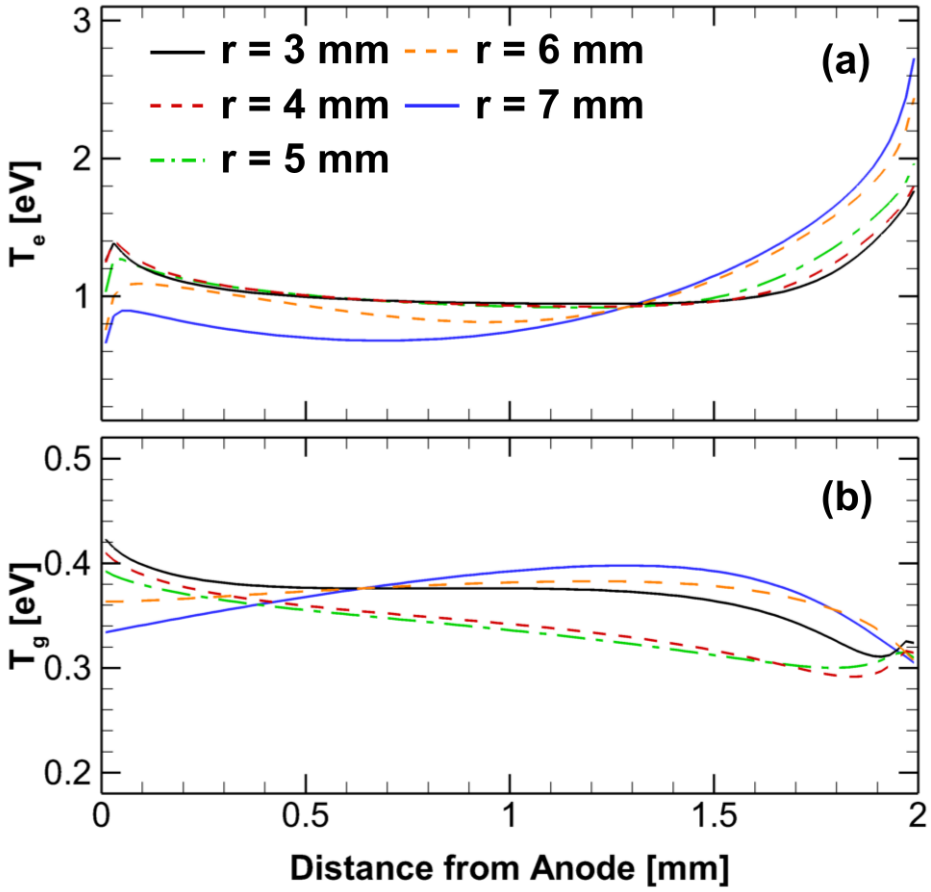

Figure 8.9: Spatial profile of temperatures for different radii at total current $I = 60$ A: (a) electron temperature and (b) gas temperature.

$U_a \simeq 0$ V. Further studies on boundary conditions can be performed in future work.

8.2.4 Gas & electron temperature

Figure 8.9 shows the results of the gas and electron temperatures for different anode diameters. Although the temperatures of the carbon species and helium are solved separately, the two temperatures become almost identical due to high collisionality between the heavy species. However, it is evident that in all cases, the numerical results deviate substantially from the LTE condition, i.e., the electron temperature is not the same as the heavy species temperature, in the present setup. While the electron temperature in the core, e.g., 1 eV, shows agreement with experimental values [1], the gas temperature is predicted to be lower,

which can be attributed to the limitation of the 1D model. In reality, the arc is constricted to a densely populated core; in the present 1D model the arc is averaged over the anode area, which yields lower densities. This in turn leads to a decrease in the number of Coulomb collisions, lowering the gas temperature due to collisions with the electrons.

8.2.5 Electric Field

Figure 8.10 shows the electric field profile for the high and low ablation cases. In the bulk plasma (e.g., 0.2 mm$\leq x \leq$ 1.7 mm), the electric field for the high ablation mode is higher than that of the low ablation mode. The higher electric field for high ablation leads to a larger plasma potential, which can be seen in Figs. 8.3 and 8.4. The reason behind this increase in electric field can be attributed to the current density through Ohm's law, $j_e = \sigma_c E$, where $\sigma_c = en_e\mu_e \propto n_e/nu_m$ is the conductivity. Since Coulomb collisions are more dominant than electron-neutral elastic collisions, the conductivity becomes a function of the electron temperature alone. As the electron temperature in the bulk remains constant around 1 eV, as shown in Fig. 8.9, the value of the conductivity is essentially constant. Thus, from Ohm's law, the electron current density and the electric field are approximately linearly related. In the high ablation mode, the electron current density increases and therefore the electric field becomes larger, leading to a large potential drop in the bulk plasma, V_{pl}.

In the region near the cathode, the electric field increases in strength. Since the electron temperature near the cathode is higher for the low ablation mode (larger r) than that for the high ablation mode (smaller r) as can be seen in Fig. 8.9, the ion Bohm velocity becomes larger and the ions need to accelerate in the presheath, resulting in a larger electric field in the cathode presheath. This can be seen in Fig. 8.10, where the electric field strength is smaller near the cathode for the high ablation mode. Additionally, it is to be noted that there exists a region of negative electric field close to the cathode in both ablation cases. This might be due to the electron diffusion flux being sufficiently large so that the drift flux is less needed, leading to a negative electric field.

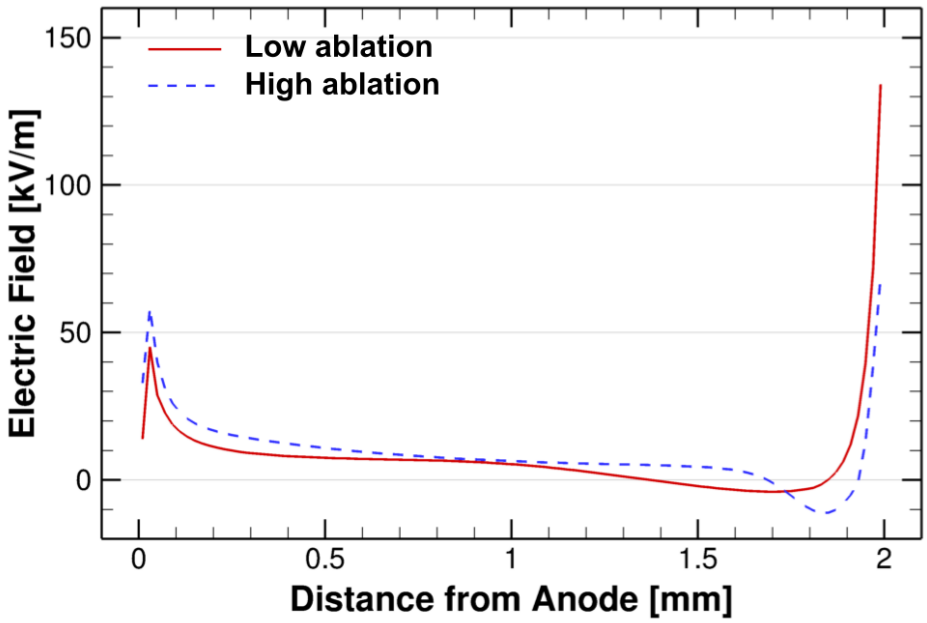

Figure 8.10: Electric field profile for low (d = 12 mm) and high (d = 6 mm) ablation modes at 60 A.

8.3 Sensitivity Analysis

Aside from the variation of the anode diameter and the total current, several other parameters in the model are investigated, and the sensitivity of the model to these parameters is tested.

8.3.1 Krook vs. Krook-Braginskii drag for electrons

The drag term for the electron transport in Eq. (5.19), which accounts for the external forces on the electrons, is investigated. The results shown so far use a hybrid of Krook's and Braginskii's models. In the low temperature plasma (LTP) community, it is common to only assume Krook's operator due to the weakly ionized state of the plasma.

Figure 8.11 shows the results between the two electron drag formulations. A 1-2 V decrease in the plasma potential drop is seen when using the Krook-Braginskii drag model, while V_c remains the same. The introduction of the thermal term $-0.71\mu_e \frac{\partial T_e}{\partial x}$ to the electron flux in Eq. (5.21) leads to a smaller electric field required to sustain a similar electron current

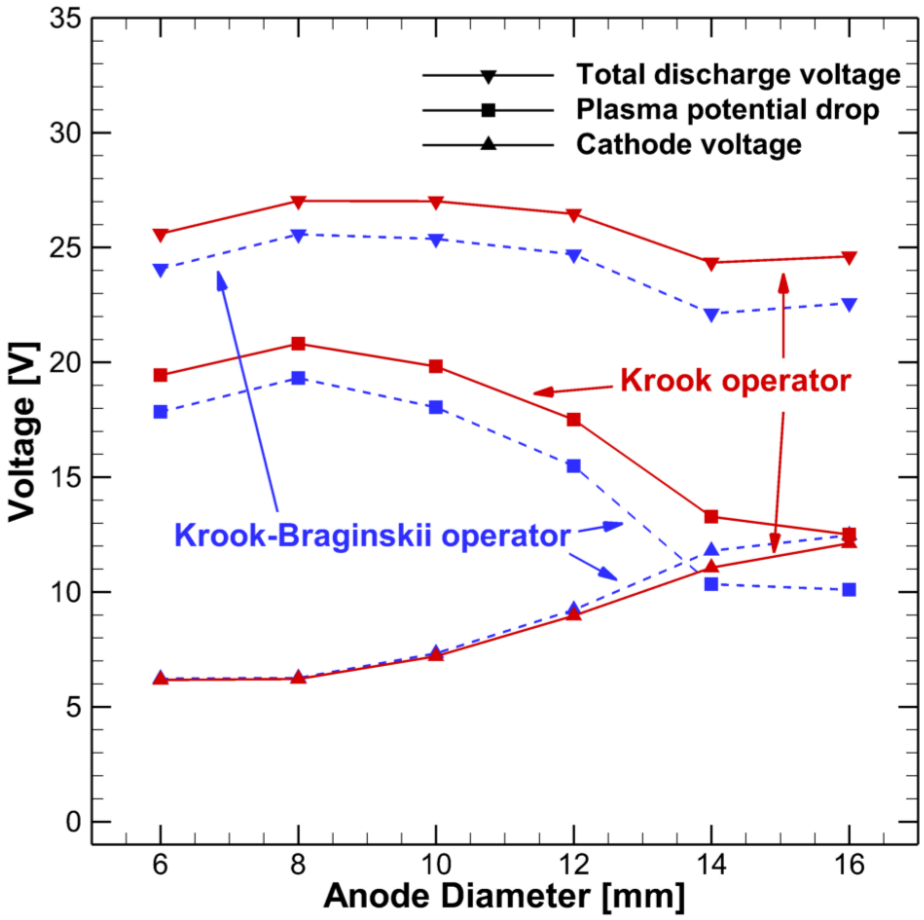

Figure 8.11: Total voltage, plasma potential drop, and cathode voltage for the cases corresponding to the two formulations of F_e in Eq. (5.19). Total current I=60 A. Red solid lines are for Krook's operator only and blue dashed lines are for the Krook-Braginskii drag force. The latter is identical to Fig. 8.4 for ε = 70%.

density. The conditions at the electrodes, including the anode temperature and thus directly the evaporation rate, as well as plasma parameters, remain similar. The results suggest that the Krook's drag operator alone overestimates the plasma potential required. In an arc where the plasma density becomes large, Coloumb collisions play an important role in the core, and as such Braginskii's model must be taken into account.

8.3.2 Varying ion Bohm velocity factor ζ due to high pressure

The Bohm sheath criterion is only valid for a collisionless sheath. When the background pressure increases, the sheath becomes collisional, and the Bohm condition no longer applies

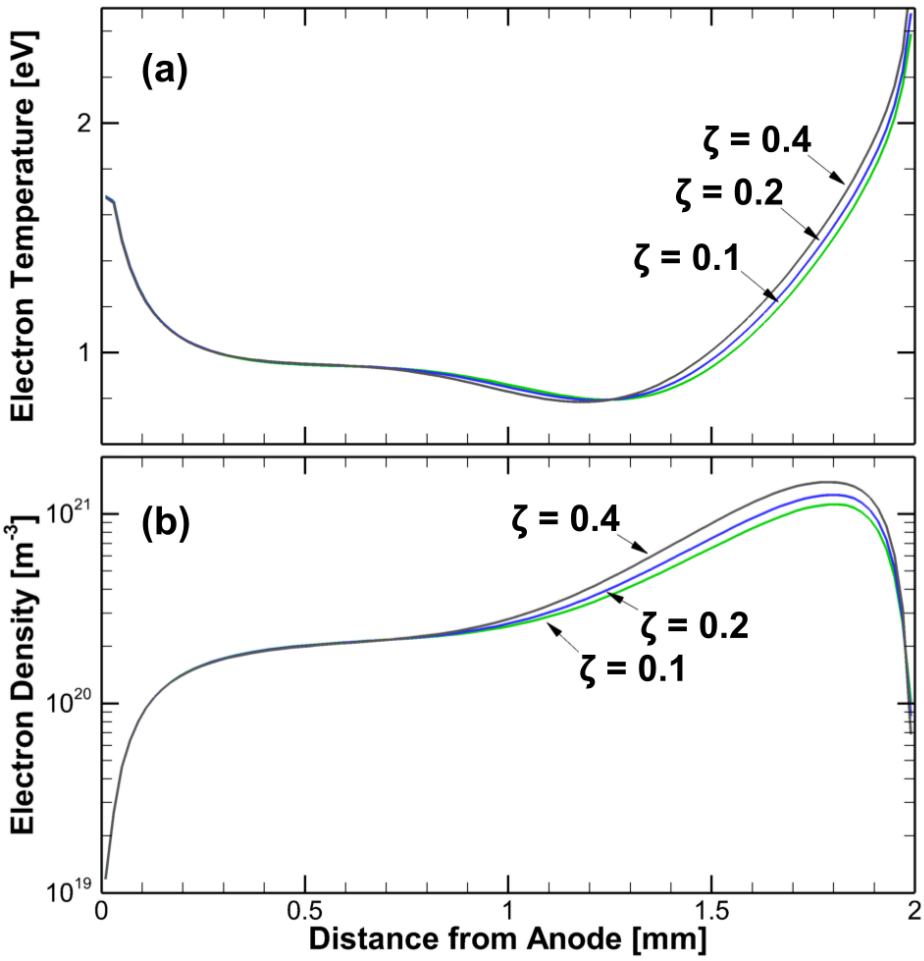

Figure 8.12: Spatial profile of (a) electron temperature and (b) electron number density for varying Bohm condition factor ζ.

[78, 79]: the ion flux increases in the presence of a high background pressure. In order to incorporate the reduced ion flux into the model, a factor ζ was introduced to the Bohm sheath criterion equation, varying from $\zeta = 1$ for a purely collisionless sheath to $\zeta = 0$ for a fully collisional sheath. In order to investigate the impact of using the Bohm sheath criterion on a collisional model, the factor ζ was varied.

The numerical results of electron temperature and number density are shown in Fig. 8.12. It is shown that the Bohm factor does not have a significant impact on the results. Increasing the factor, which directly corresponds to accelerating the ions towards the cathode sheath edge, leads to a larger electric field in the bulk plasma. This in turn increases the plasma

potential drop, which results in a higher electron temperature, as can be seen in Fig. 8.12 (a). Additionally, Table 8.1 summarizes the voltage values for all three test cases. The cathode voltage dropped proportionally to the increase in the plasma potential drop, retaining the same total discharge voltage in all cases.

The slight increase in the temperature directly leads to more ionization in the plasma, increasing the number density of the ions and electrons, as can be seen in Fig. 8.12 (b). The changes in the total voltage are not significant, and there is merely a potential drop exchange between the bulk plasma and the cathode sheath potential. It can be concluded that the macroscopic results of the model are insensitive to the Bohm condition at the anode sheath edge.

8.3.3 Artificially increasing gas temperature in the vicinity of the anode sheath edge

In an attempt to achieve results closer to LTE, the gas temperature at the anode sheath edge was artificially increased to 1.5 times the anode wall temperature, $T_{g,a} = 1.5T_{w,a}$,where $T_{w,a}$ is the *actual* anode temperature that governs the ablation rate, while $T_{g,a}$ is the *effective* gas temperature that is used as a boundary condition for the energy equation.

Figure 8.13 shows the gas and electron temperatures. While the gas temperature increases, the electron temperature in the bulk plasma is still around 1 eV, suggesting that the system is still quite far from being in LTE. The reason of the artificial increase in gas temperature is from experimental data showing 5000–6000 K near the electrode [77].

Figure 8.14 shows the corresponding change in the voltage and the evaporation rate. The plasma potential drop decreases drastically, since the number density of C atoms increases

Table 8.1: Voltage values for varying Bohm condition factor ζ. V_p, V_c, and V_d correspond to plasma potential drop, cathode voltage, and total discharge voltage, respectively.

ζ	V_d	V_c	V_p
10%	24.69 V	9.22 V	15.47 V
20%	24.70 V	8.34 V	16.36 V
40%	25.19 V	7.10 V	18.09 V

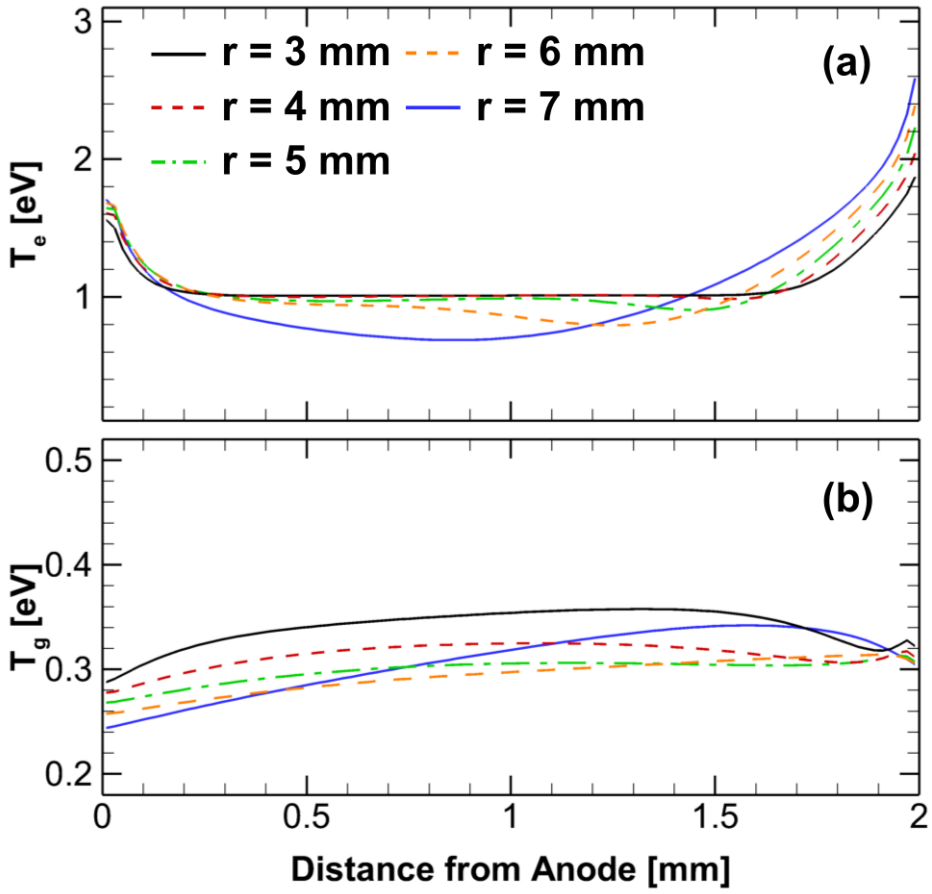

Figure 8.13: Spatial profile of (a) electron and (b) gas temperatures with anode temperature artificially increased to $T_{g,a} = 1.5T_{w,a}$.

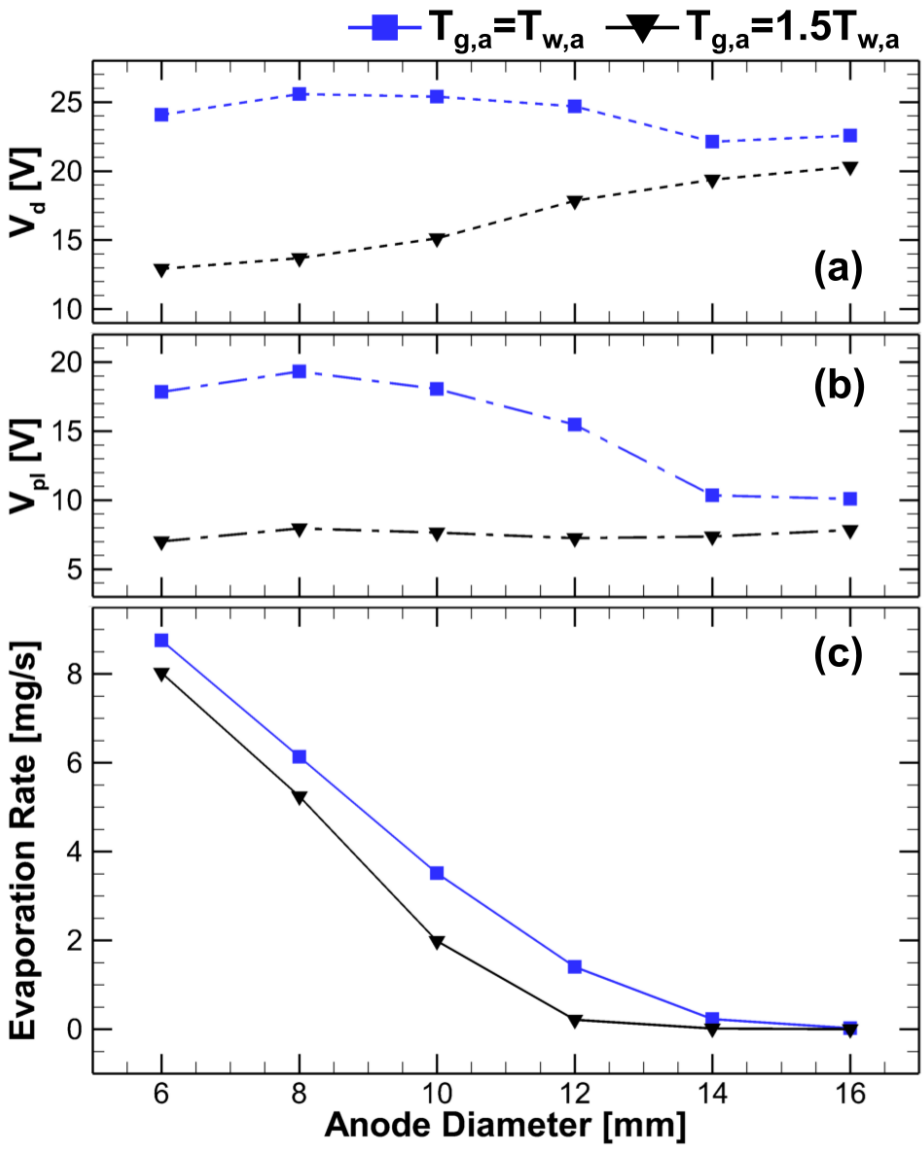

Figure 8.14: Results for total current I=60 A using artificially raised anode temperature: (a) total discharge voltage V_d, (b) plasma potential drop V_{pl} and (c) evaporation rate. $T_{g,a} = T_{w,a}$ case is identical to Fig. 8.4 with $\varepsilon = 70\%$

due to the artificially increased gas temperature. With the increase in the gas temperature, C_2 and C_3 molecule dissociate, leading to a higher C density. This provides a larger pool for ionization, making the required voltage within the bulk plasma much smaller. While the cathode sheath voltage does not change, the lower plasma potential leads to a significantly smaller total voltage. The evaporation rate also decreases, which can be attributed to the lower plasma potential drop, particularly near the anode, which leads to a lower electron temperature. This drop in the electron temperature directly leads to smaller anode wall temperatures, resulting in lower ablation rates. Although the lower ablation rate approaches the experimental trend (see Fig. 8.1 (b)), artificially increasing the gas temperature near the anode does not help the numerical results at getting closer to the experimental results.

There are various potential mechanisms for the discrepancy between the numerical model and experiments. First, multidimensional effects of the plasma flow and sheath physics may result in a more confined arc core, which yields a larger plasma density. Another possible explanation for the discrepancies between numerical and experimental results is the fact that the boundary conditions may affect the anode sheath. With a negative sheath, the plasma density particularly near the anode sheath edge can increase, which would affect the bulk plasma. Finally, the dynamic nature of the arc discharge, e.g., instabilities and oscillations, could alter the spatio-temporal distribution of the plasma flow, which in turn affects the nanomaterial synthesis.

9. CONCLUSION & FUTURE WORK

The synthesis of carbon nanotubes using ablating carbon arcs has become a subject of great interest. The limited understanding of the physical phenomena that govern the synthesis process still poses a challenge for further growth. A 1D multispecies fluid model was developed to simulate an ablating carbon arc discharge in atmospheric pressure conditions. Mass and momentum conservation equations were solved for all the species in the arc, with collisions between the species taken into account. The model does not assume any LTE conditions, solving energy equations for the electrons and the heavy species separately. Using the experimental observations, a model for the carbon deposit area is developed.

Evaporation rates obtained from the model show good agreement with experimental results, particularly when varying the total current for a given anode size. The transition between low and high ablation modes was investigated. The number densities for ions and electrons are one order of magnitude lower than experimental values, which can be attributed to the fact that the model averages the arc core over the area of the anode, when in reality the arc is more constricted, and as such has higher densities. The model did not achieve LTE conditions in the arc core as has been reported by other arc discharge models. This can be related to the lower densities, which in turn lead to lower collisional exchange of energy between the electrons and heavy species.

The model's sensitivity to several parameters was investigated, the most notable of which being the effective emissivity ε for radiative heat exchange between the cathode and anode. The numerical results using a higher value for ε, corresponding to more radiative heat flux being lost to the system's surroundings, show greater agreement with experimental results in terms of evaporation rate and total voltage for the low ablation mode. An enhancement of anode ablation is observed when accounting for more radiative heat transfer between electrodes resulting in a lower ε. The results suggest that radiative heat transfer plays a significant role in determining the properties of the ablating arc.

For future work, the model will be expanded into two dimensions, axial and radial, in order to capture the multidimensional physics. The incorporation of radial mass and heat diffusion self-consistently could provide valuable insight regarding the transition between ablation modes. The implementation of a varying arc core area would allow for a more constricted plasma, potentially yielding densities more agreeable with experimental values. Additional work can be done on the arc attachment to the electrodes, which would give insight to the instabilities observed in experiments.

10. PART II: NON-NEUTRAL DRIFT-DIFFUSION MODEL FOR HALL EFFECT THRUSTERS

Plasma thruster technology has been in development for over half a century [7, 11, 80], but to this day it faces many difficulties that cannot be resolved without the use of consistent computational models that can accurately and successfully capture the highly nonlinear and coupled physics that governs plasma thrusters [11]. Hall effect thrusters (HET) are devices that utilize an axial electric field to accelerate a propellant gas, usually xenon, while at the same time using a radial magnetic field to confine electrons that are used to ionize xenon [7]. Due to the mass difference, electrons are trapped in the $E \times B$ azimuthal direction, while the heavier ions to exit the channel, generating thrust.

Hall thrusters operate on a high specific impulse, low thrust regime, operating at 1-5 kW power range with relatively high efficiencies ranging between 35% and 60%. Specific impulse tends to be as high as 2,000 seconds, with lifetimes of about 10,000 hours [7], and thrust is on the order of tens to hundreds of milli-Newtons [81]. Recent advancements in magnetic shielding of HET channel walls have allowed for reduced erosion rates and greatly increased lifespans [82]. The development of nested Hall thrusters shows promise in providing increased thrust performance, becoming an attractive option for deep-space missions [83]. With the expansion of the operations of HET's, it becomes even more critical that we fully understand the physics governing them.

11. INTRODUCTION

Plasma discharge in HET is riddled with multiscale phenomena, with oscillations spanning modes from the kHz range up to the MHz range [84]. These oscillations arise from multiple mechanisms, including electron-neutral collisions and plasma-wall interactions, and the processes are complex and are not fully understood. One of the main low-frequency modes present in HET's is the so-called breathing mode, occurring in the 10-30 kHz range [81]. These oscillation can affect the operation parameters of the thruster, with variations in the thrust and specific impulse affecting the performance [84].

High frequency phenomena on the scale of 1-10 GHz, which coincides with the electron plasma frequency, also play a vital role in the operation of HET's. One of the main challenges in modelling Hall effect thrusters comes from the so-called anomalous electron transport [84, 85, 86]. Classical gas dynamics theory and models predict the mobility of electrons operating in the conditions of HET's, accounting for collisional and magnetic effects [85, 86]. Experiments, however, show significantly larger mobility for electrons in the cross-field direction [86]. It has been suggested that the anomalous transport is due to sheath-induced plasma instabilities [87]. Others have suggested electron cyclotron drift instability as being a source of the anomalous transport [88]. While multiple other hypotheses have been developed to explain this phenomenon, the subject is still a work in progress. Further development of models that can capture plasma instabilities may allow for better understanding of the mechanism that causes the anomalous transport.

Fluid models are often utilized for HET plasma simulations due to their relatively low computational costs compared to particle-in-cell (PIC) simulations [89, 90]. Fluid models are developed by taking the moments of the Boltzmann equations, and require assumptions for the distribution functions and fluid properties in order to close the system of equations [91, 19]. Most commonly in plasma simulations, two-fluid models are used, breaking up the ions and the electrons into their own respective set of interacting equations. An assumption

that is used is quasi-neutrality, such that the electron density is assumed to be equal to the ion density [81, 92, 93]. Another assumption used is based on the fact that electrons react to changes in the potential much faster than ions, such that the electrons are essentially steady state in the ions' timescale [84]. This, along with assuming that the electron inertial term is negligible, makes up the drift-diffusion plasma model [19, 84], which can be utilized to evaluate the potential in a quasineutral plasma. Evidently, there are multiple important assumptions that are made in plasma fluid models, and any one of these assumptions, or a combination of them, could lead to the lower electron mobility seen in computational fluid models compared to experiments. As such, it is worthwhile to investigate the effect of each individual approximation in order to come closer to a fully understanding anomalous electron transport.

The overarching motivation for this model is investigating the anomalous electron transport reported in experiments. The idea is to start with a quasineutral model and remove the underlying assumptions one at a time, studying the changes to the results progressively. This work can be considered the first step in a much broader project, investigating the effects of non-neutrality on the results from a quasineutral model.

The basis of the model presented is a quasineutral, two fluid model from Ref. [94]. In the aforementioned study, numerical oscillations due to the ion velocity stagnation point were successfully damped by coupling the electron pressure and the ion momentum. This was only achievable due to the quasineutral condition; in the present non-neutral model, other numerical approaches must be developed in order to ensure numerical stability.

The model developed simulates the operation of a HET using a 1D geometry in the axial direction. The geometry used is that of an SPT-100ML thruster: the thruster channel is 2.5 cm long, from the anode to the channel exit, and the inner and outer radii of the channel annulus are 3.45 cm and 5.0 cm, respectively. The domain extends past the channel exit, such that the total domain length is 5.0 cm. The operating gas is xenon, injected from the anode at a mass flowrate of 5 mg/s. A discharge voltage of 300 V is applied across the domain. The

magnetic field varies across the domain, being a maximum of 160 G at the channel exit.

The model simulates the non-neutral plasma using the two fluid approach, with the ions and the electrons solved separately as two different fluids. Neutral atoms are considered in the background and are not simulated; instead, a number density profile is assumed for the source term in the ion and electron equations. The fluid governing equations are derived by taking the first, second and third moments of the Boltzmann equation, leading to the continuity, momentum and energy equations, respectively. For ions, the continuity and momentum equations are solved, and the energy equation is ignored, since the ion temperature is assumed to be constant. The three equations are considered for electrons.

12.1 Governing Equations

The continuity equation for a species s is given by:

$$\frac{\partial n_s}{\partial t} + \nabla \cdot \Gamma_s = S_s, \tag{12.1}$$

where n_s is the number density, $\Gamma_s = n_s \mathbf{u}_s$ is the density flux, $\mathbf{u}_s$ is the fluid bulk velocity, S_s is the source term, and the species s is either ions, denoted by subscript i, electrons, denoted by subscript e, or neutrals, denoted by subscript n. The source term for both ions and electrons is identical and is due to direct ionization, such that $S_e = S_i = \nu_{ion.} n_e$, where $\nu_{ion.} = k_{ion.} n_n$ is the ionization frequency, $k_{ion.}$ is the ionization rate coefficient, n_n is the neutral atom density, and n_e is the electron density. The source term can include multiple reactions, such as excitation and step-wise ionization, but in this model, excited states are not considered, and as such these reactions are neglected.

The momentum equations are given by:

$$\frac{\partial (n_s \mathbf{u}_s)}{\partial t} + \nabla \cdot (n_s \mathbf{u}_s \otimes \mathbf{u}_s) + \frac{1}{m_s} \nabla p_s = \frac{q n_s}{m_s} (\mathbf{E} + \mathbf{u}_s \times \mathbf{B}) - \nu_m n_s \mathbf{u}_s, \tag{12.2}$$

where m_s is the particle mass, p_s is the partial pressure of species s, assumed to be isotropic, q is the charge of the species, being $+1$ for ions and -1 for electrons, $\mathbf{E}$ is the electric field, $\mathbf{B}$ is the magnetic field, and ν_m is the momentum transfer collision frequency.

In the operation of HET's, ions are largely unaffected by the magnetic field and are non-magnetized; as such, the $\mathbf{u}_s \times \mathbf{B}$ term is negligible. For this reason, ions are considered collisionless, while electrons are considered collisional [86]. Lastly, the electric field acts in the axial direction. By assuming that the flow is one dimensional, the ion momentum equation becomes:

$$\frac{\partial(n_i u_{i,x})}{\partial t} + \frac{\partial(n_i u_{i,x}^2)}{\partial x} + \frac{1}{m_i}\frac{\partial p_i}{\partial x} = \frac{e n_i}{m_i} E, \tag{12.3}$$

where the pressure $p_i = n_i k_B T_i$ is given by the ideal gas law, k_B is Boltzmann's constant, and T_i is the ion temperature, assumed to be constant for simplicity.

For the electrons, the drift diffusion approximation is utilized to simulate the momentum. This assumption comes from the fact that the time scale for electron motion is much smaller than the ion characteristic time, such that electron momentum is in steady state. The inertial term is also neglected, based on the fact that collisions take place on a much smaller time and length scale than macroscopic field and pressure variations [19]. These two assumptions cancel out the first two terms of Eq. (12.2). The momentum transfer collision frequency for electrons is taken to be $\nu_m = 2.5 \times 10^{-13} n_n$ [81].

To derive the magnetized drift-diffusion equation, the three components of the electron velocity are retained, such that $\mathbf{u}_e = u_{e,x}\hat{\mathbf{i}} + u_{e,y}\hat{\mathbf{j}} + u_{e,z}\hat{\mathbf{k}}$. By taking the cross product between the velocity and magnetic field vectors, and by assuming one-dimensionality of the pressure term, the electron momentum equations become:

$$\frac{1}{m_e}\frac{\partial p_e}{\partial x} = -\frac{e n_e}{m_e}(E_x - u_{e,z} B_y) - \nu_m n_e u_{e,x}, \tag{12.4}$$

$$0 = -\frac{e n_e}{m_e} u_{e,x} B_y - \nu_m n_e u_{e,z}. \tag{12.5}$$

Substituting the second equation into the first, then isolating $n_e u_{e,x}$:

$$n_e u_{e,x}\left(1+\Omega^2\right) = -\frac{\mu_e}{e}\frac{\partial p_e}{\partial x} - \mu_e n_e E_x,$$

where $\Omega = \omega_B/\nu_m$ is the Hall parameter, which is the ratio of the electron gyrofrequency $\omega_B = eB/m_e$ and the momentum transfer collision frequency, and $\mu_e = e/m_e\nu_m$ is the non-magnetized electron mobility. By defining the cross-field mobility $\mu_{e,\perp} = \mu_e/(1+\Omega^2)$, the 1D electron momentum equation is given by:

$$n_e u_{e,x} = -\mu_{e,\perp} n_e E - \frac{\mu_{e,\perp}}{e}\frac{\partial p_e}{\partial x}.$$

Using the ideal gas law, such that $p_e = n_e k_B T_e$, where T_e is the electron temperature, and defining the diffusion coefficient $D = k_B T_e \mu_{e,\perp}/e$, the equation can be rewritten as:

$$\Gamma_e = -\mu_{e,\perp} n_e E - \frac{\partial(D n_e)}{\partial x}, \tag{12.6}$$

where $\Gamma_e = n_e u_{e,x}$ is the electron density flux. By substituting this flux into Eq. (12.1), the governing drift-diffusion equation for electrons is attained:

$$\frac{\partial n_e}{\partial t} + \frac{\partial}{\partial x}\left[-\mu_{e,\perp} n_e E - \frac{\partial(D n_e)}{\partial x}\right] = S_e, \tag{12.7}$$

where S_e is the electron source term, taken to be direct ionization.

Based on experimental evidence, the electron mobility is higher than what is described by the classical mobility derived here, a phenomenon known as anomalous electron transport. The electron mobility used in Eq. (12.7) is as such modified to include empirically determined anomalous mobility, such that:

$$\mu_{e,\perp,tot.} = \mu_{e,\perp} + \mu_{e,\perp,ano.},$$

where $\mu_{e,\perp,tot.}$ is the total, modified electron mobility, $\mu_{e,\perp}$ is the classical mobility as defined earlier, $\mu_{e,\perp,ano.} = \alpha/B$ is the anomalous contribution to the mobility, and α is an empirical coefficient, chosen such that the mean discharge current agrees with experimental observations. A two region model is adopted, such that $\alpha = 1/16$ inside the channel of the HET, and $\alpha = 1/160$ outside the thruster channel, according to the geometry described in Chapter 11.

While the model only resolves the plasma in the axial direction, electrons exhibit a high velocity in the azimuthal direction that greatly increases their kinetic energy, and as such this velocity needs to be accounted for. The azimuthal velocity is given by Eq. (12.5):

$$u_{e,z} = \Omega u_{e,x},$$

where $u_{e,z}$ is the azimuthal velocity. Note that this is an approximation based on the drift-diffusion model. The azimuthal velocity is exaggerated in regions where the axial velocity is high, and this could lead to inaccurate kinetic energy calculations. This is further discussed in the results.

The electron energy equation is given by:

$$\frac{\partial(n_e\varepsilon_e)}{\partial t} + \nabla \cdot (n_e\varepsilon_e\mathbf{u}_e + p_e\mathbf{u}_e + \mathbf{q}_e) = \mathbf{j}_e \cdot \mathbf{E} - S_{loss}, \tag{12.8}$$

where $\varepsilon_e = 3k_BT_e/2 + m_e|\mathbf{u}_e|^2/2$ is the electron total energy, comprised of the internal energy for the first term and the kinetic energy for the second term, $\mathbf{q}_e = -\kappa_e\nabla T_e$ is the heat conduction, κ_e is the electron heat conductivity, $\mathbf{j}_e = -en_e\mathbf{u}_e$ is the electron current density, and S_{loss} is the energy loss term, which will be discussed further shortly.

Instead of solving for the total electron energy, the equation can be solved for the electron temperature alone. This can be achieved by substituting the definition of the total energy ε_e into Eq. (12.8), taking the dot product of the momentum equation for electrons (Eq. (12.2)) and the electron bulk velocity $\mathbf{u}_e$, then subtracting the result from the energy equation. The

electron internal energy equation thus becomes:

$$\frac{\partial}{\partial t}\left(\frac{3}{2}n_e k_B T_e\right) + \nabla \cdot \left(\frac{5}{2}n_e k_B T_e \mathbf{u}_e + \mathbf{q}_e\right) = \nabla p_e \cdot \mathbf{u}_e + m_e n_e \nu_m |\mathbf{u}_e|^2 - S_{loss}. \tag{12.9}$$

The electron energy loss term S_{loss} is comprised of wall heat loss S_{wall} and heat lost due to collisions, $S_{coll.}$. The former is is further discussed in Section 12.4. The collision heat loss term is due to inelastic collisions, such as ionization and excitation, and is given by $S_{coll.} = \sum_s n_e \nu_s \Delta\varepsilon_s$, where ν_s is the collision frequency and $\Delta\varepsilon_s$ is the change in the energy level for collision s.

Since the plasma is non-neutral, the plasma potential needs to be evaluated in order to update the electric field, and that is done by solving Poisson's equation, given by:

$$\nabla \cdot (\varepsilon_0 \nabla \phi) = -e(n_i - n_e), \tag{12.10}$$

where ε_0 is the permittivity of free space and ϕ is the potential. Once the potential is evaluated, the electric field is found using the electrostatic condition:

$$E = -\nabla \phi. \tag{12.11}$$

Neutrals are only basically simulated, with a constant uniform temperature and a constant velocity of 270 m/s, being injected from the anode plane. As such, the only equation solved for neutrals is continuity Eq. (12.1), where the flux is simply $\Gamma_n = u_{n,x} n_n$ using the constant injection velocity, and the ionization source term $S_n = -S_e = -S_i$ reflects the depletion of neutral atoms as they ionize.

12.2 Boundary Conditions

The boundary conditions (BC's) of the model are imposed at the two ends of the domain, corresponding to the anode and the cathode of the HET. The BC's imposed include the electric potential at each electrode, the electron temperature, the particle fluxes, and the

particle injection speed. The BC's are imposed at the cell interfaces, as opposed to the cell centers, since the electrodes reside on the interfaces. The electric potential uses Dirichlet BC at both ends of the domain, such the potential is set to 300 V at the anode and 0 V at the cathode. For the electron temperature, a combination of Dirichlet and Neumann BC's are used. The temperature is set to 3 eV at the cathode, and at the anode, an adiabatic BC is used.

For ions and electrons, kinetic fluxes are imposed on the anode assuming a shifted half-Maxwellian distribution while assuming the particles are traveling in one direction only. The derivation begins with the shifted Maxwellian distribution function:

$$f(v_{s,x}) = \left(\frac{m_s}{2\pi k_B T_s}\right)^{1/2} \exp\left[-\frac{m_s(v_{s,x} - u_{s,x})}{2k_B T_s}\right], \tag{12.12}$$

where f is the distribution function, $v_{s,x}$ is the particle velocity, m_s is the particle mass of species s, T_s is the temperature, and $u_{s,x}$ is the fluid bulk velocity. The particle flux is obtained by multiplying the distribution function by $v_{s,x}n_s$, where n_s is the number density, then integrating over the range of particle speeds $v_{s,x}$. Since a half-Maxwellian is assumed, and the particles are travelling towards the anode, the function is integrated from $-\infty$ to 0:

$$\Gamma_{s,a} = \int_{-\infty}^{0} v_{s,x} n_s \left(\frac{m_s}{2\pi k_B T_s}\right)^{1/2} \exp\left[-\frac{m_s(v_{s,x} - u_{s,x})}{2k_B T_s}\right] dv_{s,x},$$

where $\Gamma_{s,a}$ is the kinetic flux of species s at the anode surface, moving outwards. Once the integration is carried out using a substitution, the flux can be written as:

$$\Gamma_{s,a} = -\frac{n_s}{4}\left(\frac{8k_B T_s}{\pi m_s}\right)^{1/2} \left\{\sqrt{\pi}\hat{u}_{s,x}\left[-1 + \mathrm{erf}\left(\hat{u}_{s,x}\right)\right] + \exp\left(-\hat{u}_{s,x}^2\right)\right\}, \tag{12.13}$$

where $\left(\frac{8k_B T_s}{\pi m_s}\right)^{1/2}$ is the local thermal speed, $\hat{u}_{s,x} = u_{s,x}\sqrt{m/2k_B T_s}$ is the local fluid bulk velocity normalized using the internal energy, and erf is the error function.

At the cathode, a Maxwellian distribution is assumed for the ions, such that the integration

of Eq. (12.12) is done from $-\infty$ to ∞, which simply yields:

$$\Gamma_{i,c} = n_i u_{i,x}, \tag{12.14}$$

where $\Gamma_{i,c}$ is the ion kinetic flux at the cathode surface, corresponding to an outflow condition.

In order to formulate the cathode electron flux, the plasma is assumed to be quasineutral in the vicinity of the cathode. Using the discretized continuity equation (Eq. (12.1)) for both the ions and the electrons at the last cell center N:

$$\frac{n_{e,N}^{k+1} - n_{e,N}^{k}}{\Delta t} + \frac{\Gamma_{e,c}^{k} - \Gamma_{e,N-1/2}^{k}}{\Delta x} = S_{e,N},$$

$$\frac{n_{i,N}^{k+1} - n_{i,N}^{k}}{\Delta t} + \frac{\Gamma_{i,c}^{k} - \Gamma_{i,N-1/2}^{k}}{\Delta x} = S_{i,N},$$

where the source terms $S_{e,N} = S_{i,N}$ are equivalent, the number densities for both ions and electrons in the next timestep $k+1$ are set to be equal. Substituting the two equations into each other, and solving for the cathode electron flux $\Gamma_{e,c}$, the expression becomes:

$$\Gamma_{e,c} = \Gamma_{e,N-1/2} + \Gamma_{i,c} - \Gamma_{i,N-1/2} + \frac{\Delta x}{\Delta t}(n_{e,N}^{k} - n_{i,N}^{k}), \tag{12.15}$$

of which all the components on the right hand side are known beforehand.

The anode BC for neutrals at the anode surface accounts for wall recombination. As ions and electrons collide with the anode surface, they recombine, forming neutral atoms that can then be re-injected into the thruster. The cathode BC for neutrals is simply an outflow condition.

12.3 Numerical Methods

The equations being solved by the model are, in summary: the ion continuity equation (Eq. (12.1)) and momentum equation (Eq. (12.3)) to evaluate the ion density and velocity, respectively; the electron drift-drift equation (Eq. (12.7)) to evaluate the electron density

and velocity; the electron energy equation (Eq. (12.9)) to evaluate the electron temperature; Poisson's equation (Eq. (12.10)) and the electrostatic condition (Eq. (12.11)) to evaluate the plasma potential and electric field, respectively; and the neutral continuity equation (Eq. (12.1)) to update the neutral density. The system of equations is highly coupled and can have very restrictive timestep limitations. The numerical methods discussed here seek to alleviate some of those issues.

12.3.1 Ion solver

The ion continuity and momentum equations are solved using Steger-Warming inviscid flux vector splitting (FVS) method, utilizing MUSCL reconstruction with Koren limiter to eliminate the sonic problem for rarefaction waves. The eigenvalues of the fluid governing equations are evaluated and used to calculate the fluxes for the ion density, momentum, and energy. Since the ion energy is not solved, the latter is not evaluated. Both Steger-Warming and MUSCL reconstruction are further described in Appendix B.

Steger-Warming has been shown, mathematically and numerically, to generate numerical oscillations on the grid level at locations of stationary contact discontinuities, i.e. where $u_{i,x} = 0$ [95]. This can be alleviated by using a global flux vector splitting method, such as Global Lax-Friedrichs, which is used in this model. While the fluxes are evaluated the same way as Steger-Warming, a global parameter is accounted for in the calculation of the eigenvalues. Further discussion of the implementation of Global Lax-Friedrichs is presented in Appendix B.

12.3.2 Electron solver

Two components of the electron governing equation can be identified: the drift component $\partial(-\mu_{e,\perp} n_e E)/\partial x$, which bears resemblance to the advection equation, and the diffusion component $\partial^2(-D n_e)/\partial x^2$, which is the term of the diffusion equation. Both the advection and the diffusion equations are heavily studied numerical problems with well developed solution methods.

Discretizing the drift-diffusion equation (Eq. (12.7)) around cell center j for timestep k using first order Euler for time integration yields:

$$\frac{n_{e,j}^{k+1} - n_{e,j}^{k}}{\Delta t} + \frac{\Gamma_{e,j+1/2}^{k} - \Gamma_{e,j-1/2}^{k}}{\Delta x} = S_{e,j}, \tag{12.16}$$

where $\Gamma_{e,j+1/2}$ is the drift-diffusion flux defined by Eq. (12.6). Defining the components of the flux at the cell interfaces ($j \pm 1/2$) is discussed below.

First order upwind is used to solve the drift portion of the electron flux. While the electric field E is inherently evaluated at the cell interfaces, the electron mobility and density $\mu_{e,\perp} n_e$ are in the cell centers. The interface value of the mobility is taken as the average of the adjacent cell center values. Upwind is used to evaluate the number density at the interface: if the propagation speed $-\mu_{e,\perp} E$ at the interface is positive, the density from the left cell center is used at the interface, and vice versa. When done explicitly, this provides a conditionally stable solution method, subject to the Courant-Friedrichs-Lewy (CFL) condition:

$$\left| \frac{c \Delta t}{\Delta x} \right| \leq 1,$$

where $c = \mu_{e,\perp} E$ is the propagation speed. This is the first and least restricting limitation imposed on the simulation timestep size. The electric field can be of the order of 10^4 V/m, and the non-magnetized can be of the order 10^4 $\mathrm{m}^2/(\mathrm{Vs})$, so that the restriction on the timestep can be $\Delta t \leq \Delta x \times 10^{-8}$ s, depending on the chosen grid size. Since the model simulates magnetized electrons, the mobility becomes at most on the order of 10^2, making this condition even less restrictive.

Second order central difference is used to solve the diffusion component of the electron flux. Central difference uses the cell center values to evaluate the second derivative on the cell center, and no reconstruction of the variables to the interfaces is needed. The scheme is

conditionally stable, subject to the Von Neumann condition:

$$\left|\frac{D\Delta t}{\Delta x^2}\right| \leq 0.5,$$

where D is the diffusion coefficient. This timestep constraint is very restrictive, due to the square dependence on the grid size. The non-magnetized diffusion coefficient can be on the order of 10^5 m^2/s, making the timestep size relation $\Delta t \leq 0.5\Delta x^2 \times 10^{-5}$ s, whereas in the case of magnetized electrons, this becomes two orders of magnitude larger. A grid size of 10^{-5} m, which is around what is used in this model, would require a timestep size on the picosecond or sub-picosecond scale.

In order to alleviate the restriction imposed by the Von Neumann condition, an implicit number density solver can be implemented. Both upwind and central difference can be easily formulated in an implicit fashion, but the issues lies in imposing the BC's. From Eq. (12.13), it can be seen that the boundary flux is a highly non-linear function of the velocity, which in turn is a function of the number density and the flux. The terms cannot be implicitly extracted, and using values from the previous timestep would be inconsistent and could lead to numerical instabilities. As such, the electron density is updated explicitly, and the Von Neumann condition is used to dictate the timestep size.

12.3.3 Scharfetter-Gummel method for drift-diffusion flux

Scharfetter-Gummel (S-G) scheme is a method used to discretize the drift-diffusion equation [19, 96]. The discretization is derived by solving the ODE of the drift diffusion flux, Eq. (12.6) [97]. Assuming that in the interval $[x_j, x_{j+1}]$ all quantities are constant, and $n_{e,j} = n_{e,j}(x)$, the flux equation can be rearranged into:

$$\frac{dn_e(x)}{dx} = -\frac{\mu_{e,\perp}E}{D}n_e(x) - \frac{\Gamma_e}{D},$$

which can be solved to yield:

$$n_e(x) + \frac{\Gamma_e}{\mu_{e,\perp} E} = \exp\left(-\frac{\mu_{e,\perp} E}{D} x + b\right),$$

where b is a constant of integration that will cancel out shortly. In order to evaluate $\Gamma_{e,j+1/2}$, which is constant on the interval $[x_j, x_{j+1}]$, The above equation is written at points j and $j+1$:

$$n_e(x_j) - \frac{\Gamma_{e,j+1/2}}{W_{j+1/2}} = \exp\left(\frac{W_{j+1/2}}{D_{j+1/2}} x_j + b\right),$$

$$n_e(x_{j+1}) - \frac{\Gamma_{e,j+1/2}}{W_{j+1/2}} = \exp\left(\frac{W_{j+1/2}}{D_{j+1/2}} x_{j+1} + b\right),$$

where $W_{j+1/2} = -\mu_{e,\perp} E$ is the constant advection speed in the interval $[x_j, x_{j+1}]$. Substituting the two equations into each other and solving for $\Gamma_{e,j+1/2}$, the electron drift-diffusion flux using S-G becomes:

$$\begin{aligned}\Gamma_{j+1/2} &= \frac{W_{j+1/2}\left[n_{j+1} - \exp(z_{j+1/2}) n_j\right]}{\exp(z_{j+1/2}) - 1} \\ &= -\frac{D_{j+1/2}}{\Delta x}\left[\frac{z_{j+1/2} n_{j+1} - z_{j+1/2}\exp(z_{j+1/2}) n_j}{\exp(z_{j+1/2}) - 1}\right], \quad (12.17)\end{aligned}$$

where $z_{j+1/2} = W_{j+1/2}(x_{j+1} - x_j)/D_{j+1/2}$. This is a combination of upwind and central difference, and that can be seen in the limits of the parameters. In the limit of $W_{j+1/2} \to 0$, the flux becomes:

$$\lim_{W \to 0} \Gamma_{e,j+1/2} = -D_{j+1/2} \frac{n_{j+1} - n_j}{\Delta x},$$

which when substituted into Eq. (12.7) yields the central difference equation. Likewise, taking the limit of the diffusion coefficient:

$$\lim_{D\to 0} \Gamma_{e,j+1/2} = \begin{cases} W_{j+1/2} n_j & \text{if } W_{j+1/2} > 0, \\ W_{j+1/2} n_{j+1} & \text{if } W_{j+1/2} < 0, \end{cases}$$

which is simply the upwind scheme. As long as the Von Neumann and CFL conditions are satisfied, the electron number density is updated without the introduction of numerical instabilities or oscillations.

12.3.4 Electron temperature solver

The electron energy equation is solved using second order implicit Crank-Nicolson scheme for the left hand side terms of Eq. (12.9). The terms on the right hand side are evaluated explicitly. Due to the coupling of the electron energy with source terms and collision frequencies, thus the electron transport directly, an explicit treatment of the energy equation could lead to the growth of minor oscillations [98]. Additionally, it adds a timestep limitation, dependent on the heat conductivity [99, 100], and as such, the electron energy equation is solved semi-implicitly. The semi-implicit Crank-Nicolson scheme is described in Appendix C. The resulting tridiagonal matrix is solved using the highly-efficient Thomas tridiagonal solver, described in Appendix A.

12.3.5 Poisson solver

Poisson's equation is solved using second order central difference. The discretized equation is given by:

$$\frac{\phi_{j-1} - 2\phi_j + \phi_{j+1}}{\Delta x^2} = -\frac{e}{\varepsilon_0}(n_{i,j} - n_{e,j}),$$

which when discretized over the entire domain forms a tridiagonal matrix that is then solved using Thomas tridiagonal matrix solver, described in Appendix A. The cell centered electric

potential values are then used to find the cell interface values of the electric field:

$$E_{j+1/2} = -\frac{\phi_{j+1} - \phi_j}{\Delta x}.$$

12.3.6 Semi-implicit Poisson solver

One of the challenges faced when simulating non-neutral plasmas is the very strong coupling between the charged particles, especially electrons, and the electric field. As the particles move, the charge distribution shifts, and the electric field changes accordingly. Electrons, due to their low mass, respond rapidly to the perturbations in the electric field, quickly shifting the charge distribution once again. For this reason, when simulating non-neutral plasmas, the timestep size must be small enough to resolve the time it takes electrons and the electric field to react to changes in each other. This is known as the dielectric relaxation time or the Maxwell relaxation time, and it is evaluated as:

$$\tau_d = \frac{\varepsilon_0}{\sum_s |q_s| \mu_s n_s},$$

where τ_d is the dielectric relaxation time, s denotes the charged species, and q_s is the charge of the species. Since the mobility of the electrons is several orders of magnitude higher than the mobility of ions, τ_d is assumed to only depend on electron quantities, such that

$$\tau_d = \frac{\varepsilon_0}{e \mu_e n_e}. \tag{12.18}$$

Typically, this constraint restricts the allowable timestep size substantially. With electron densities being on the order of $10^{17} - 10^{18}$ m^{-3} and non-magnetized electron mobility being on the order of 10^4 m^2/V $\cdot$ s, the dielectric relaxation time can be as small as 10^{-15} seconds, making simulation times absurdly long. Since the electrons are magnetized in this model, the mobility is much smaller, and the timestep size restriction is on the order of 10^{-12} s, which is comparable to the timestep restriction imposed by the Von Neumann condition discussed

earlier. Due to that and the fact that the electron density is solved explicitly, the explicit Poisson equation is solved in this model. However, a method to alleviate the constraint set by the dielectric relaxation time was developed. For the sake of completion, it is described below.

One way to bypass the dielectric relaxation time is to solve the Poisson equation implicitly, using information from the next timestep to evaluate the potential in the next timestep as well. This, however, would require the ion and electron densities to be solved implicitly, leading to a complicated numerical system. Alternatively, Poisson's equation can be solved semi-implicitly by using *predicted* ion and electron number densities using the potential in the next timestep with other quantities from the current timestep. The semi-implicit Poisson equation is given by:

$$\frac{\partial}{\partial x}\left(\varepsilon_0 \frac{\partial \phi}{\partial x}\right) = -e\left(n_i^* - n_e^*\right), \tag{12.19}$$

where n_i^* and n_e^* are the predicted ion and electron number densities, respectively. To evaluate the predicted densities, the continuity equation (Eq. (12.1)) is used, with the fluxes being functions of the electric fields in the future timestep:

$$n_i^* = n_i^k + \Delta t \frac{\partial \Gamma_i(E^{k+1})}{\partial x}, \tag{12.20}$$

$$n_e^* = n_e^k + \Delta t \frac{\partial \Gamma_e(E^{k+1})}{\partial x}. \tag{12.21}$$

Note that the source term is neglected; since the term is shared between ions and electrons, it cancels in Eq. (12.19). The use of the electric field at a future timestep introduces some implicitness to the model, and alleviates the constraint set on the timestep size by the dielectric relaxation time.

The strong coupling in the Poisson equation happens with the electrons due to the drift-diffusion equation. By combining the momentum and continuity equations for the electrons, the density flux becomes directly dependent on the electric field. That is not the case for

the ions, for which the number density flux does not depend on the electric field explicitly. For this reason, the predicted ion density used in Eq. (12.19) uses the flux from the current timestep, and the implicitness is only introduced through the electrons.

By substituting the drift-diffusion flux Eq. (12.7) using the electric field in the future timestep into Eq. (12.21), and substituting the predicted number density into Poisson's equation Eq. (12.19), the equation becomes:

$$\frac{\partial}{\partial x}\left(\varepsilon_0 \frac{\partial \phi}{\partial x}^{k+1}\right) = -e\left(n_i^k + \Delta t \frac{\partial \Gamma_i}{\partial x} - \left[n_e^k + \Delta t \frac{\partial}{\partial x}\left(n_e \mu_e \frac{\partial \phi}{\partial x}^{k+1} - \frac{\mu_e}{e}\frac{\partial p_e}{\partial x}\right)\right]\right),$$

which can be rearranged in order to group all the ϕ^{k+1} terms on the left hand side:

$$\frac{\partial}{\partial x}\left[\left(\varepsilon_0 - \Delta t e n_e \mu_e\right)\frac{\partial \phi}{\partial x}^{k+1}\right] = -e\left(n_i^k + \Delta t \frac{\partial \Gamma_i}{\partial x} - n_e^k + \Delta t \frac{\partial}{\partial x}\left(\frac{\mu_e}{e}\frac{\partial p_e}{\partial x}\right)\right), \tag{12.22}$$

which is the 1D semi-implicit Poisson equation using drift diffusion flux. Discretizing the equation around grid point j:

$$\begin{aligned}\left[\left(\varepsilon_0 - e\Delta t n_e \mu_e\right)\frac{\partial \phi}{\partial x}^{k+1}\right]_{j+1/2} - \left[\left(\varepsilon_0 - e\Delta t n_e \mu_e\right)\frac{\partial \phi}{\partial x}^{k+1}\right]_{j-1/2} \\ = -e\Delta x(n_{i,j}^k - n_{e,j}^k) - e\Delta t\left(\Gamma_i + \frac{\mu_e}{e}\frac{\partial p_e}{\partial x}\right)_{j+1/2}^k + e\Delta t\left(\Gamma_i + \frac{\mu_e}{e}\frac{\partial p_e}{\partial x}\right)_{j-1/2}^k.\end{aligned}$$

Further discretizing and grouping terms together gives the system in a tridiagonal form:

$$\begin{aligned}&\left(\varepsilon_0 - e\Delta t n_e \mu_e\right)_{j+1/2}\phi_{j+1}^{k+1} \\ &\qquad - \left[\left(\varepsilon_0 - e\Delta t n_e \mu_e\right)_{j+1/2} + \left(\varepsilon_0 - e\Delta t n_e \mu_e\right)_{j-1/2}\right]\phi_j^{k+1} \\ &\qquad + \left(\varepsilon_0 - e\Delta t n_e \mu_e\right)_{j-1/2}\phi_{j-1}^{k+1} \\ &= -e\Delta x(n_{i,j}^k - n_{e,j}^k) - e\Delta t\left(\Gamma_i + \frac{\mu_e}{e}\frac{\partial p_e}{\partial x}\right)_{j+1/2}^k + e\Delta t\left(\Gamma_i + \frac{\mu_e}{e}\frac{\partial p_e}{\partial x}\right)_{j-1/2}^k,\end{aligned} \tag{12.23}$$

which is the discretized semi-implicit Poisson equation. All the quantities on the right hand

side and the coefficients of ϕ on the right hand side are known quantities from the current timestep. Thomas tridiagonal matrix solver is used to evaluate the potential throughout the domain, and the resulting electric field is then used to update the ions and electrons.

12.3.7 Coupling semi-implicit Poisson with Scharfetter-Gummel

The implementation of Scharfetter-Gummel adds a level of complexity to the implementation of the semi-implicit Poisson solver. As can be seen in Eq. (12.19), the Poisson solver depends on predicted densities, using the future potential to evaluate the fluxes. Since the S-G flux non-linearly depends on the electric field, the future potential cannot be intuitively extracted from the flux. In order to solve this problem, a Taylor expansion of the S-G flux around E is performed [101]:

$$\Gamma_{j+1/2}(E_{j+1/2}^{k+1}) \approx \Gamma_{j+1/2}(E_{j+1/2}^{k}) + \left(\frac{\partial \Gamma}{\partial E}\right)_{j+1/2}^{k} (E_{j+1/2}^{k+1} - E_{j+1/2}^{k}). \tag{12.24}$$

From here on, for this derivation and for the sake of brevity, the subscript $j + 1/2$ will be omitted. The S-G flux is given by Eq. (12.17). To evaluate the derivative of the flux with respect to the electric field, a chain rule is applied:

$$\frac{\partial \Gamma}{\partial E} = \frac{\partial \Gamma}{\partial z}\frac{\partial z}{\partial E},$$

$$\longrightarrow \frac{\partial \Gamma}{\partial z} = -\frac{D}{\Delta x}\left[\frac{e^z(1-z)-z}{(e^z-1)^2}n_{j+1} - \frac{e^z(e^z-1-z)}{(e^z-1)^2}n_j\right],$$

$$\longrightarrow \frac{\partial z}{\partial E} = \frac{-\mu_e \Delta x}{D},$$

$$\longrightarrow \frac{\partial \Gamma}{\partial E} = \mu_e\left[\frac{e^z(1-z)-z}{(e^z-1)^2}n_{j+1} - \frac{e^z(e^z-1-z)}{(e^z-1)^2}n_j\right].$$

Combining the above with Eq. (12.24) leads to an expression of the S-G flux that is decoupled from the electric field in the next timestep. Knowing that $E_{j+1/2}^{k+1} = (\phi_{j+1} - \phi_j)/\Delta x$, this

expression of the flux can be substituted into Eq. (12.22), and the terms involving the potential in the future timestep can be grouped together:

$$\frac{\partial}{\partial x}\left[\left(\varepsilon_0 - \Delta t\frac{\partial \Gamma_e^k}{\partial E}\right)\frac{\partial \phi}{\partial x}^{k+1}\right] = -e\left[n_i^k - n_e^k + \Delta t\frac{\partial}{\partial x}\left(\Gamma_i^k - \Gamma_e^k + \frac{\partial \Gamma_e^k}{\partial E}E^k\right)\right]. \tag{12.25}$$

This equation is then discretized and solved much in the same way as Eq. (12.22). It is important to note that while semi-implicit Poisson and the coupling of semi-implicit Poisson with S-G have been developed, they were not used in the final version of the model, due to the dielectric relaxation time and the Von Neumann condition being on the same order. Both methods are reported for the sake of completion.

12.3.8 Neutral density solver

Neutral atoms are greatly simplified in the model, with a constant velocity and temperature assumed uniformly throughout the domain. The neutral continuity equation is solved using first order upwind. Since the velocity is constant and positive to the right, the discretized equation through the domain is given by:

$$\frac{n_{n,j}^{k+1} - n_{n,j}^k}{\Delta t} + u_{n,x}\frac{n_j^k - n_{j-1}^k}{\Delta x} = S_n,$$

such that the flux imposes upwind, with boundary conditions imposed as described in Section 12.2.

12.4 Numerical Parameters

The numerical parameters used in the model are summarized here. The domain is divided into 800 cells of 6.275×10^{-5} m. In order to resolve the Debye length, a grid size of the order of 10^{-5} must be used, according to the following equation:

$$\lambda_D = \sqrt{\frac{\varepsilon_0 k_B T_e}{n_e e^2}},$$

where λ_D is the Debye length. The Debye length for this model's range of temperatures and densities is on the order of 10^{-5} m. The model was found not to be sensitive to the gridsize.

The timestep size used in the simulations is based on the Von Neumann condition for the stability of the electron diffusion term in Eq. (12.7). The diffusion coefficient becomes very large in the anode sheath region due to the steep number density gradient, and due to that, the timestep size needs to be set at a value smaller than 5 picoseconds (10^{-12} s). For this reason, a timestep size of 4×10^{-12} s is used.

The wall heat loss term S_{wall} from Eq. (12.9) is considered a varying parameter in this model. The electron energy loss due to wall sheaths in the radial direction is given by:

$$S_{wall}(\varepsilon_e) = \alpha_{\varepsilon_e} 10^7 \exp\left(-\frac{U}{\varepsilon_e}\right)\varepsilon_e,$$

where α_{ε_e} is an adjustable parameter that can be set based empirical data [81, 102], in this model set to unity, and U is another experimental parameter, taken to be 20 eV [81]. The loss term represents the energy lost by electrons as they bombard the walls of the channel due to secondary electron emission. In the model, the part of the domain where this term is activated is varied as an input parameter. In one case, the simulation is done with the wall heat loss term being active in the channel, and another case has the wall heat loss term active in the entire domain. The justification behind the latter is the fact that outside the channel, the plasma bombards the outside walls of the spacecraft, losing its energy in the process. Additionally, due to the 1D assumption of the model, this can be seen as a radial diffusion mechanism through which the electrons lose energy. The results between the two are compared and are discussed in Ch. 13.

Another adjustable term in the model is the electron kinetic energy. As previously mentioned in Section 12.1, the azimuthal velocity of the electrons is not explicitly modeled, but instead is the Hall parameter multiplied by the axial velocity. Due to the development of an anode sheath in the non-neutral model, the electron axial velocity near the anode becomes

very large, two orders of magnitude larger than the velocities farther in the channel and outside the channel. This leads the azimuthal velocity to become unphysically large as well, and both contribute to the electron kinetic energy being over 100 eV in the anode sheath. This directly leads to higher ionization rates in the sheath. It is worthwhile to study the significance of this heightened kinetic energy on the results. A control parameter χ is introduced to the model, such that:

$$\chi = \begin{cases} 100x & \text{if } 0 \leq x \leq 0.01, \\ 1 & \text{if } 0.01 \leq x, \end{cases}$$

and the electron kinetic energy is then multiplied by χ, effectively being turned off at the anode and linearly growing until it retains its full value 1 cm away from the anode. The effects on the results are discussed. Note that this parameter affects the kinetic energy as part of the total energy only; the electron velocities are not affected directly in any way.

13. RESULTS & DISCUSSION

The numerical results of this model are benchmarked and compared to the results of the quasineutral model presented in Ref. [94]. In that model, numerical oscillations around the ion velocity stagnation point were mitigated and effectively removed by coupling the electron pressure with the ion momentum. The study utilized quasineutrality ($n_i \approx n_e$) to make the electron pressure a function of the ion density. Since the model developed here is non-neutral, this substitution cannot be utilized. Instead, Global Lax scheme for FVS is utilized in order to remove the oscillations reported in Ref. [94]. By using global Lax instead of Steger-Warming, the oscillations at the ion stagnation point never initiate, and the model successfully runs without any numerical oscillations.

13.1 Plasma Properties

The results presented in this section are, unless otherwise specified, from the case where the wall losses due to collisions in the electron energy equation (Eq. (12.8)) are inactive outside the channel. The plasma parameters, such as the number density, electron velocity, and electric field, are largely unaffected by having the losses active. The parameters that are affected are explicitly presented in this section and discussed.

Figure 13.1 shows the number density profile for both the quasineutral and the non-neutral models. The number density profile distinctly shows the development of an anode sheath due to the lower electron density. Another feature can be seen at the channel exit (0.025 m), where the electron density is slightly higher than the ion density. This corresponds to the region of maximum electric field. The plasma density in the channel is lower for the non-neutral model than the quasineutral model, and that can be attributed to the much higher particle flux at the anode due to the development of the sheath.

Figure 13.2 shows the electron axial and azimuthal velocities, compared to results from the quasineutral model. It can be seen that the axial velocity largely coincides with the

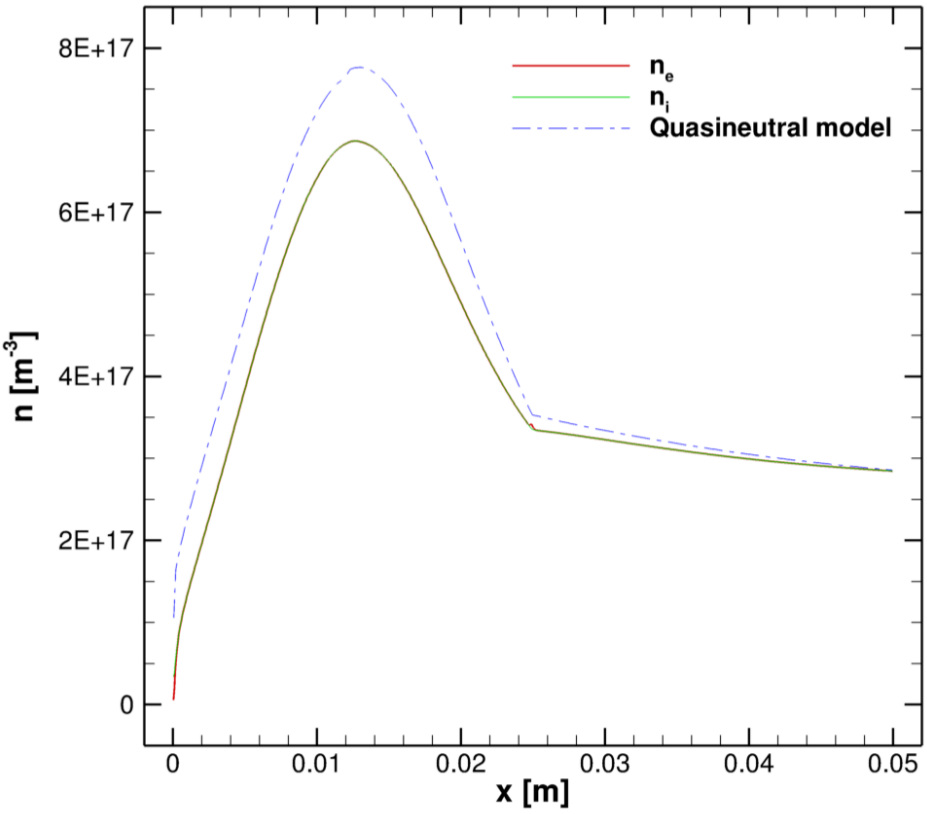

Figure 13.1: Spatial distribution of the plasma density for the current non-neutral and the quasineutral models.

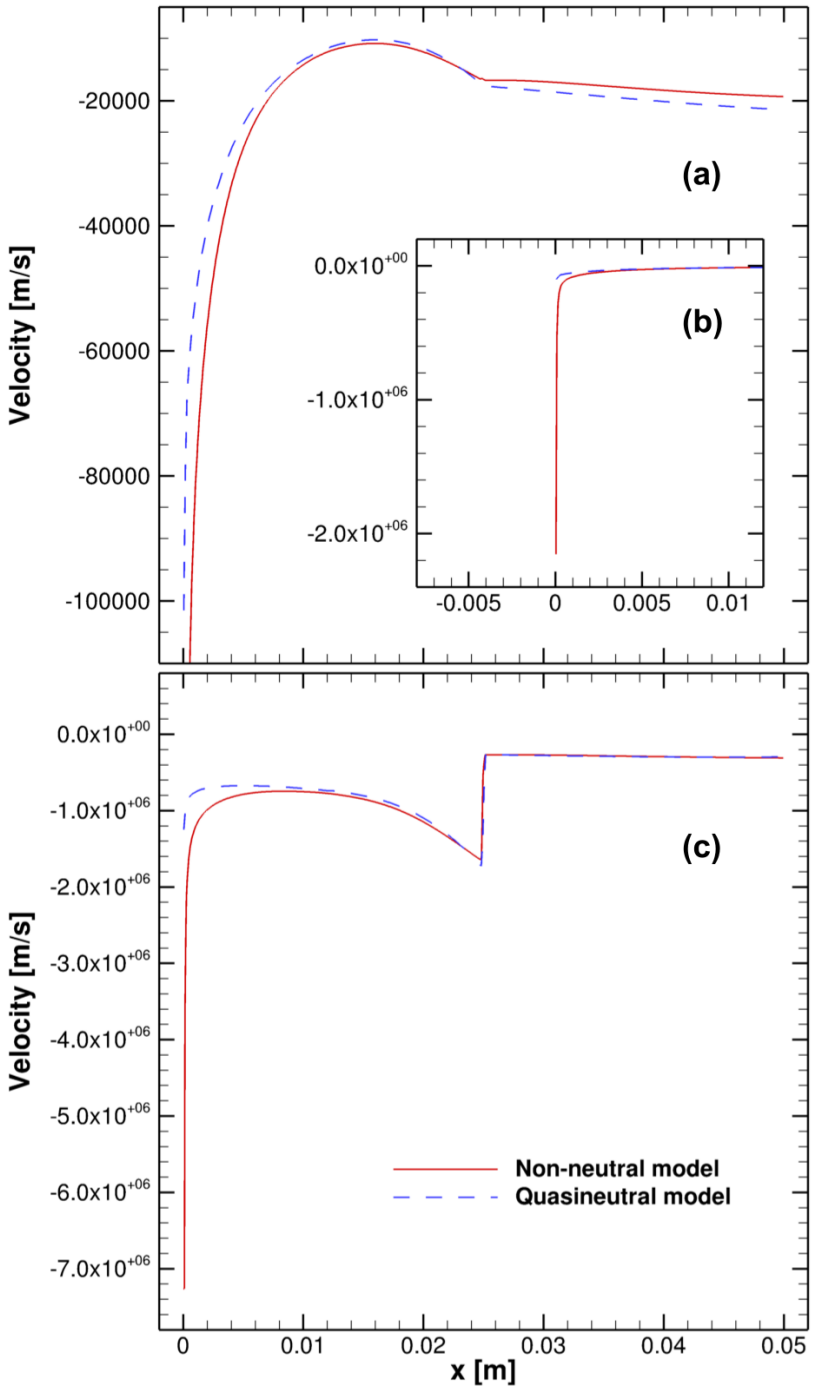

Figure 13.2: Electron velocity profile for the current non-neutral model and the quasineutral model (a) in the axial direction, (b) in the axial direction near the anode, and (c) in the azimuthal direction.

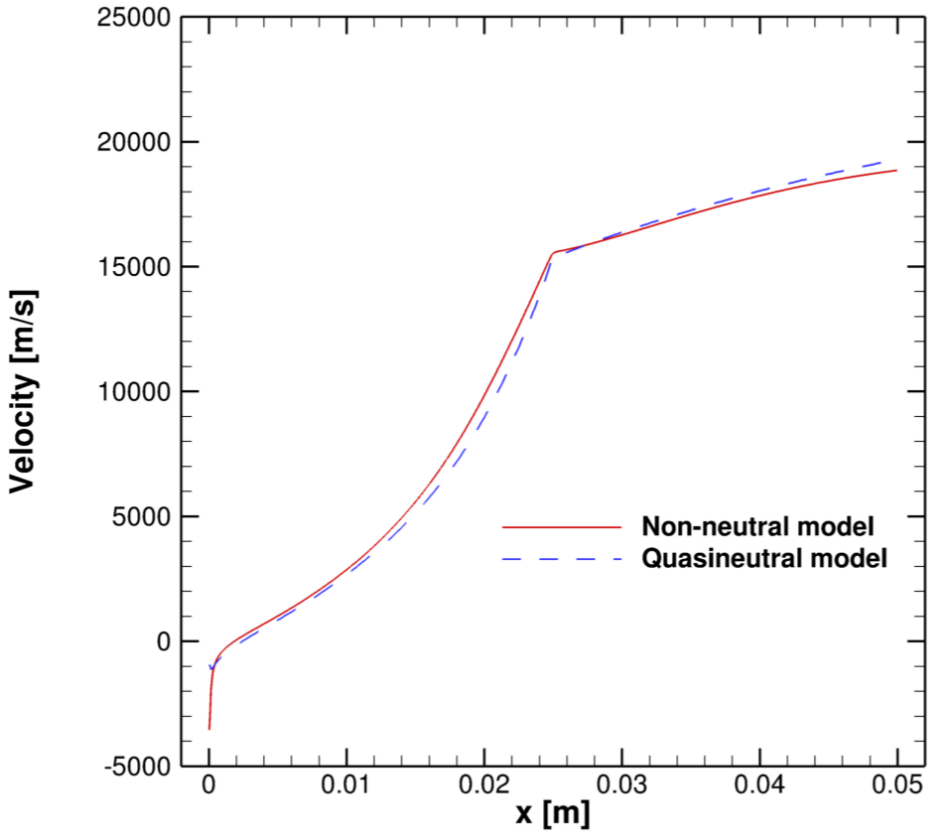

Figure 13.3: Ion velocity profile for the current non-neutral model and the quasineutral model.

quasineutral model, with significant deviation only occurring in the anode sheath. In the sheath, the drop in the electron density causes electrons to accelerate, reaching the high velocities seen here as they bombard the anode. The azimuthal velocity is very high in the anode region as well, and this is an artifact from the method in which the azimuthal velocity is evaluated in the model. Preliminary results from a 1D-2V model that solves for the azimuthal velocity directly show a much smaller azimuthal velocity near the anode. The increased velocity directly leads to higher kinetic and total energies, which in turn leads to artificially inflated ionization rates in the anode sheath.

Figure 13.3 shows the ion velocity for both models. Both models overcome the issue with oscillations appearing in the vicinity of the ion stagnation velocity point (around 0.003 m)

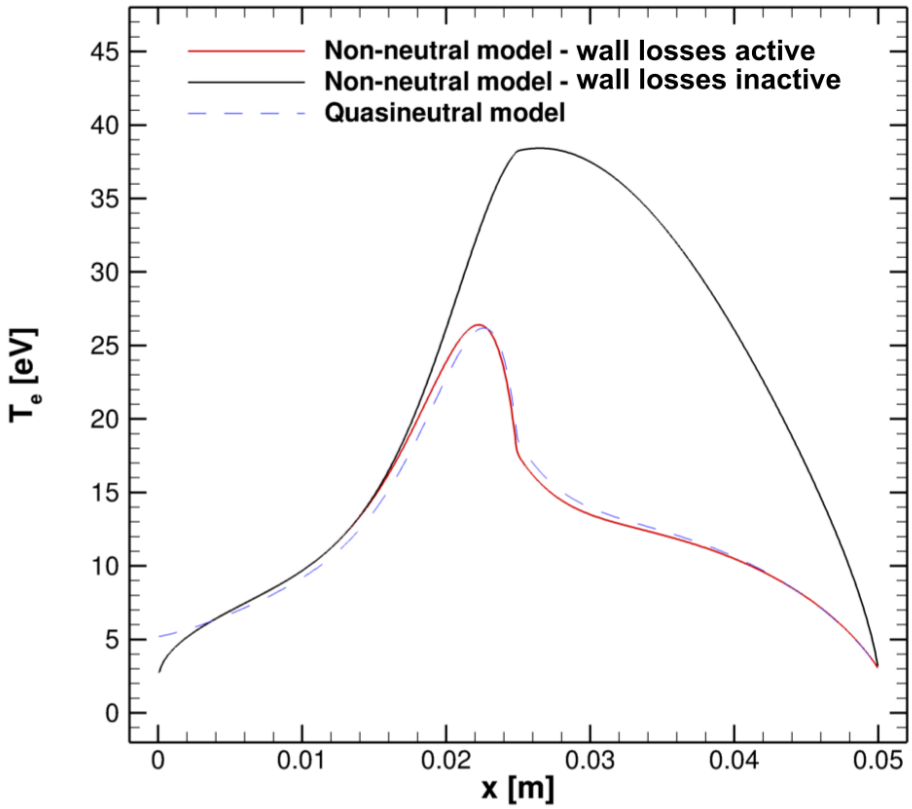

Figure 13.4: Spatial distribution of the electron temperature for the non-neutral model, with wall losses outside the channel being active and inactive, and the quasineutral model.

due to Steger-Warming FVS, albeit using different methods. The ion velocity in the anode region is higher in the non-neutral model, and that is due to the larger electric field developed due to the sheath.

Figure 13.4 shows the temperature distribution in the domain, compared to the quasineutral model, and comparing the cases with and without wall collisions outside the channel, as discussed in Section 12.4. The main difference between the quasineutral and the non-neutral models is the fact that the temperature is lower near the anode in the non-neutral model. This can be attributed to the higher electron velocity seen in Fig. 13.2, which causes the electrons to lose more energy as they bombard the anode surface. The clear difference between the cases with and without wall collisions outside the channel is the significantly higher temperature in the latter case, showing the effect of wall collisions have on the electron energy. The

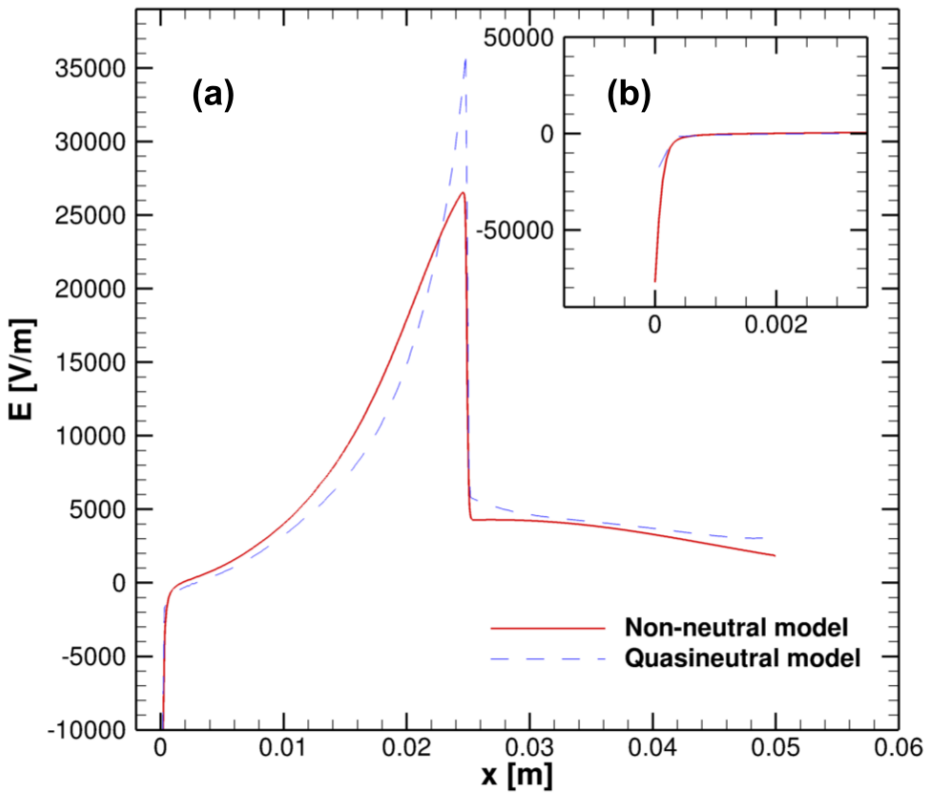

Figure 13.5: Spatial distribution of the electric field for the non-neutral model and the quasineutral model (a) across the entire domain and (b) in the anode region.

location of the maximum temperature is shifted closer to the channel exit in the case of no wall collisions outside the channel. This leads to the ionization rate becoming larger farther from the anode, and this could play a role in the breathing mode oscillations.

Figure 13.5 shows the electric field for both models, and several differences become immediately apparent. The electric field in the anode region is almost an order of magnitude larger in the non-neutral model, due to the development of the anode sheath. The peak electric field is larger in the quasineutral model, and this can be attributed to the method of evaluating the electric field. In the quasineutral model, the electron velocity is calculated from the current conservation, and then used with the quasineutral plasma density in the drift-diffusion equation (Eq. (12.7) to solve for the electric field. This results in the features of the electron mobility, such as the discontinuity in the anomalous mobility, being more

pronounced in the electric field. It is to be expected that the largest divergence between the two models occurs in the electric field.

13.2 Artificially Lowered Electron Kinetic Energy

As previously mentioned in Section 12.4, an artificial parameter χ was introduced to the electron kinetic energy. This parameter essentially makes the kinetic energy zero at the anode, and linearly allows it to grow until it reaches it's total value 1 cm away from the anode. The most significant effect this would have is lower ionization rates in the anode region, due to the drop in the total (internal and kinetic) energy of the electrons. Another difference is in the electron energy equation: the energy loss term due to inelastic collisions depends on the total electron energy, and as such would be lower in the anode region, leading to an increased electron temperature. Figure 13.6 shows how high the total energy in the anode becomes, and how it is effectively lowered. It can be seen that the total energy goes up to 200 eV in the anode region, which is an order of magnitude higher than what it would had the azimuthal velocity not been as high as it is. While electrons become energetic in the anode sheath region, they reach energies of about 40 eV [103]. The increased energy due to the azimuthal velocity can have a significant effect on the results.

Figure 13.7 shows the electron temperature with and without wall collisions outside the channel, comparing the results with and without the parameter χ. It can be seen that the electron temperature rises slightly in the anode region when χ is active and the kinetic energy is artificially decreased. The smaller inelastic collisions energy loss term directly corresponds to the electrons having more energy in the region, leading to this increase in the temperature. While this increase leads to slightly higher electron energy, it is far outweighed by the decrease in the total energy due to artificially decreasing the kinetic energy. This decrease in the total energy leads to a lower ionization rate, since the ionization rate coefficient is a function of the electron energy.

Figure 13.8 shows the ionization rate profile in steady state with and without the parameter χ. It can be seen that originally, the ionization rate profile had a spike in the anode. This

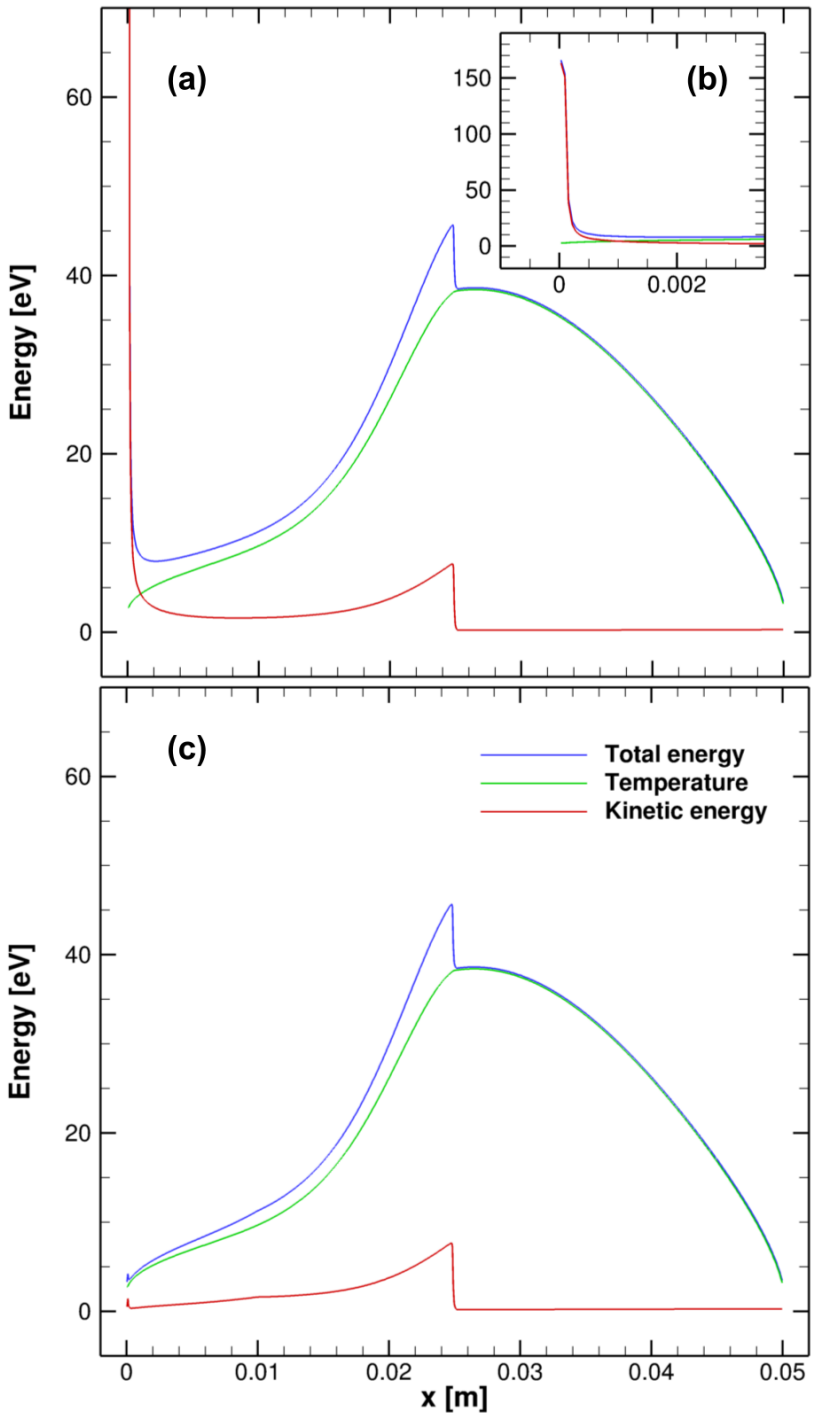

Figure 13.6: Electron total energy (a) without reducing the kinetic energy, (b) in the anode region, and (c) after introducing the kinetic energy parameter χ.

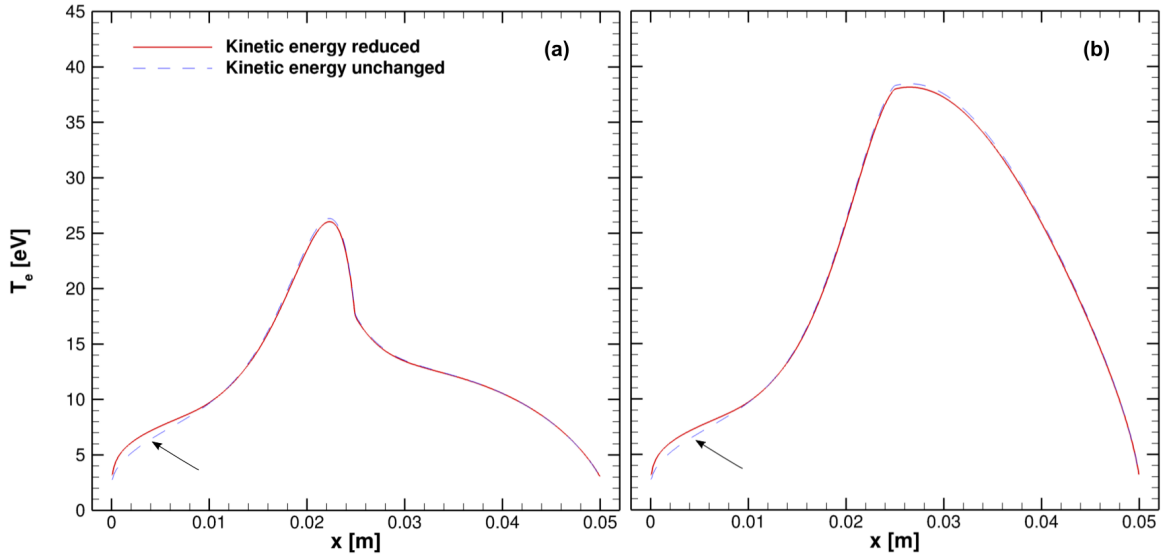

Figure 13.7: Spatial profile of the electron temperature with and without kinetic energy parameter χ for (a) wall collisions active outside the channel and (b) wall collisions inactive outside the channel.

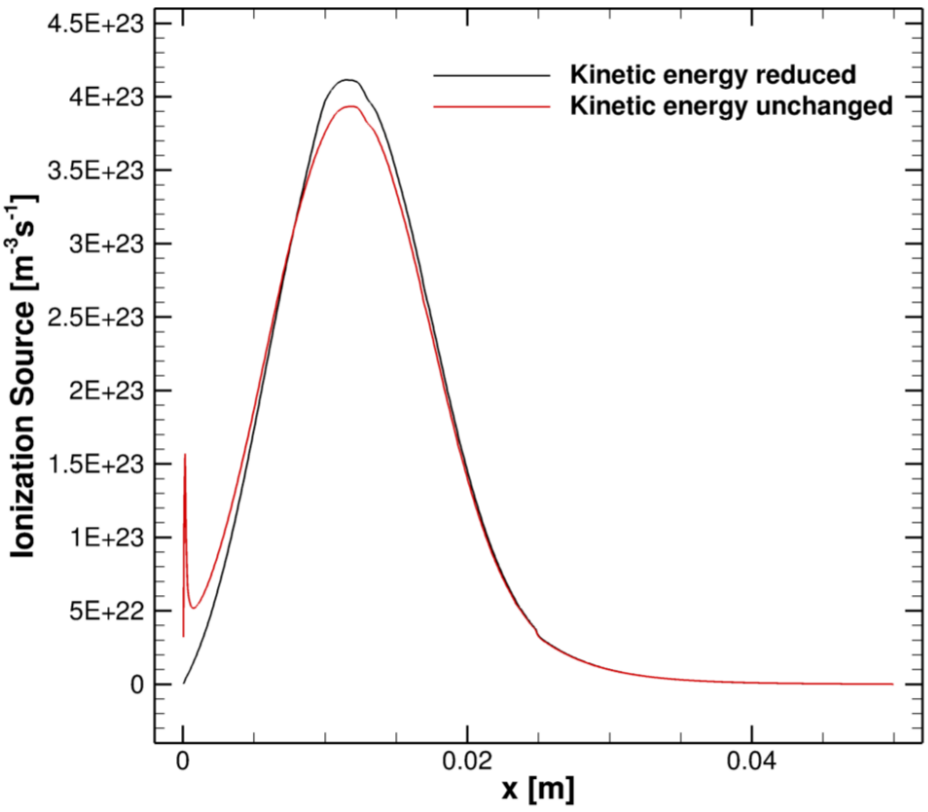

Figure 13.8: Spatial profile of the ionization rate with and without the kinetic energy parameter χ.

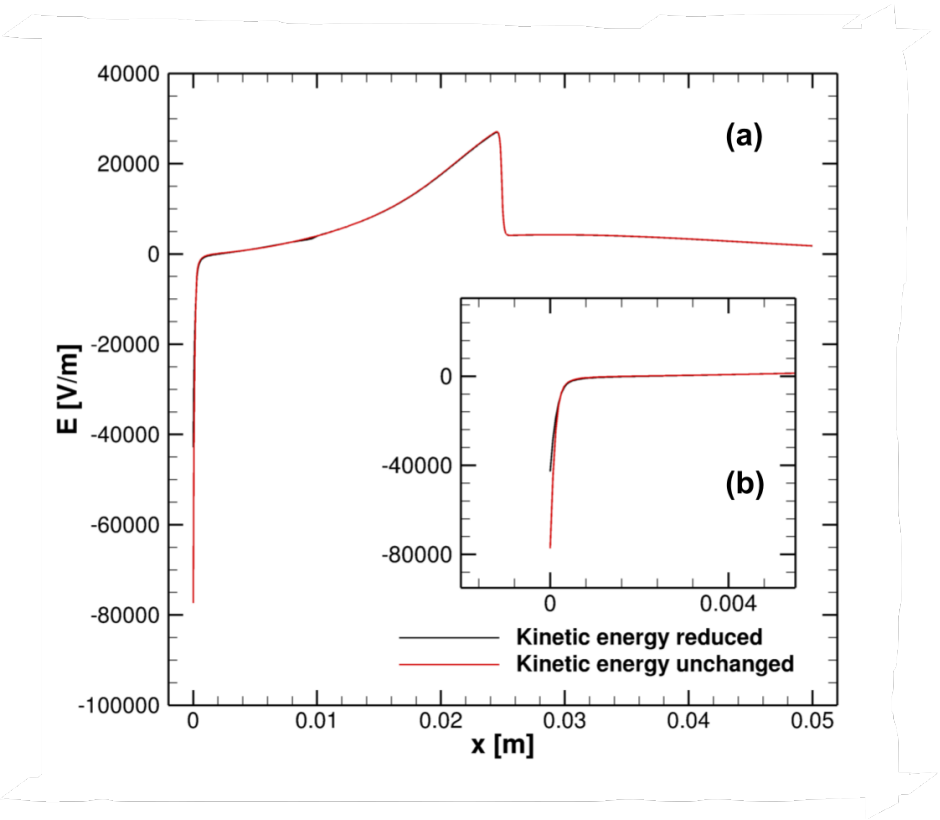

Figure 13.9: Spatial profile of the electric field with and without kinetic energy parameter χ (a) across the entire domain and (b) in the anode region.

can be attributed to the extremely high electron total energy leading to high values of the rate coefficient, while the rapidly decreasing number density in the region decreases the ionization rate, leading to this profile. The lower ionization rate in the anode region in turn leads to a smaller ion population, closing the gap between the the ion and electron densities, and effectively making the anode sheath smaller.

Figure 13.9 compares the the electric fields without and without χ, and it becomes immediately clear that the lower ionization rate significantly changes the makeup of the anode sheath. The lower ion density manifests itself in a smaller anode potential drop, in both cases leading to an electric field about half the size of the cases with no χ.

It was suggested in Ref. [104] that the electron transport is the main stabilizing mechanism for breathing mode oscillations. Specifically, the electron energy balance between Joule

heating, convective fluxes, wall losses and inelastic collisions plays a significant role in damping the breathing modes. In the results shown in Fig. 13.10, it can be seen that when the kinetic energy is artificially decreased, the breathing mode oscillations are damped less than in the baseline cases. This can be attributed to the aforementioned electron energy balance: the decreased kinetic energy leads to lower energy loss due to inelastic collisions. This essentially means that one of the main cooling mechanisms is less effective, and consequently the oscillations do not damp as much.

13.3 Discharge Current

Figure 13.10 shows the discharge current as a function of time. Breathing mode oscillations with a frequency of 19-21 kHz can be clearly seen. This falls within the range of frequencies within which breathing modes have been observed in both experiments [105] and both kinetic and fluid simulations [106]. The time averaged discharge current is between 7.28 A and 7.38 A for all cases, with the former corresponding to the case when wall collisions are inactive outside the channel. These values agree with the discharge current reported in the quasineutral model, where the steady-state current is 7.29 A [94].

While for all the cases shown the breathing mode oscillation frequency is the same, there's a sizeable difference in both the amplitude of the waves and more importantly the damping rate. The waves start out with a larger amplitude when there are no wall collisions outside the channel, but they damp much more quickly than the case with wall collisions outside the channel. This further supports the hypothesis that the damping of the breathing modes depends heavily on the electron energy. With the removal of wall losses as a cooling mechanism outside the channel, the ionization front moves farther away from the anode, and its oscillation damps faster.

It is important to note that the oscillations seen the electron current may not be breathing modes altogether. They could simply rise from the current trying to adjust itself to the discharge level that corresponds to the steady-state current for the applied voltage imposed on the model. Since the initial condition for the current is not the final value, the current adjusts

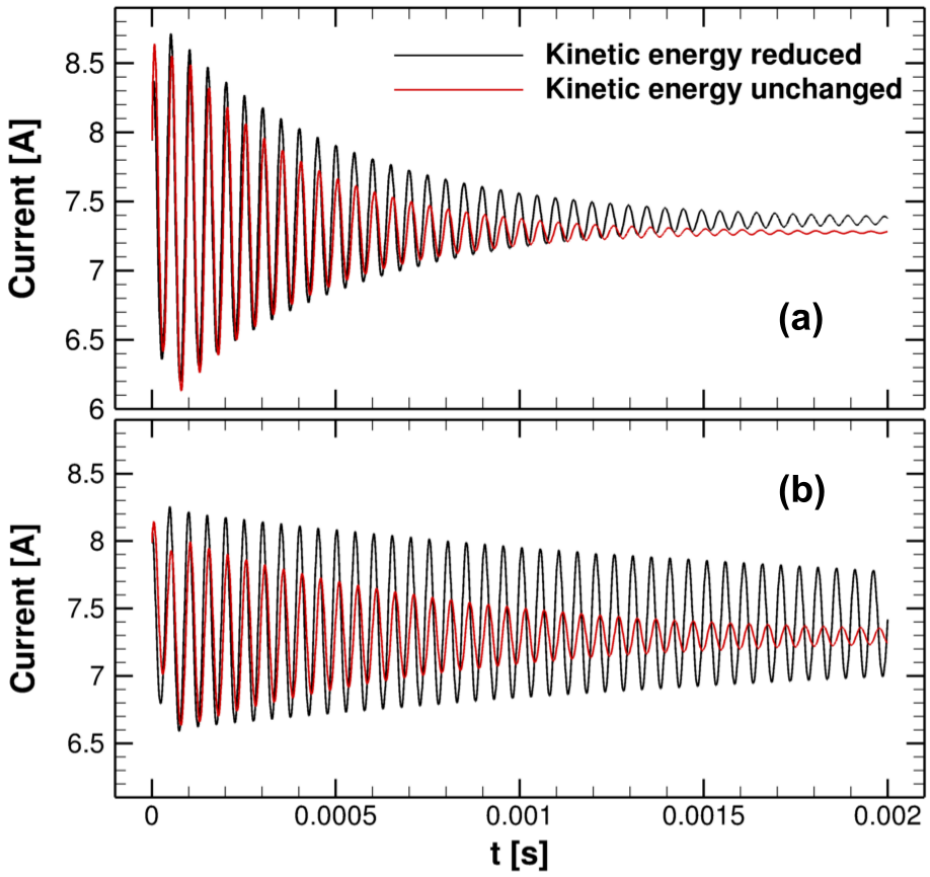

Figure 13.10: Discharge current over time for (a) wall collisions inactive outside the channel and (b) wall collisions active outside the channel.

itself by oscillating and damping to the steady state value. The current oscillates at the natural frequency of the system, which happens to be the breathing modes. A possible explanation for the damping of these oscillations, with the system reaching a steady state instead of propagating the breathing modes, is related to the large anomalous mobility outside the channel. This mobility conducts the electric current and dampens the oscillations.

As previously mentioned, the reduction of the kinetic energy leads to less energy loss due to inelastic collisions near the anode. The lower electron energy in the anode region leads to less energy loss due to inelastic collisions, and that may play a role in causing the breathing mode oscillations to damp more slowly. The combination of the four cases shown suggests that while the damping of the breathing mode oscillations depends heavily on the electron energy, it also depends on where in the physical domain electron energy mechanisms act. The damping of the oscillations is sensitive to changes in the near-anode region, where slightly higher energy loss can lead to significant change in the damping effect. On the other hand, farther from the anode, a decrease in energy loss can move the main ionization front away from the anode, further damping the oscillations. Further investigation of the effect of other energy loss mechanisms might give more insight into the effect of the electron energy on the damping of the breathing mode oscillations.

14. CONCLUSIONS & FUTURE WORK

Plasma propulsion is a field that has been in development and a subject of great interest for the past half century. Hall effect thrusters offer a highly efficient, high specific impulse, moderate thrust operation parameters that have already been used for stationkeeping in satellites, and show promise in terms of use for deep-space exploration. Many of the mechanisms governing HET's are not fully understood, and self-consistent computational models help expand our knowledge of their operation and further expand this field.

A 1D non-neutral drift-diffusion model was developed to simulate the operation of a Hall effect thruster by solving for both ions and electrons, and evaluating the plasma potential by solving Poisson's equation. Several numerical methods were developed and implemented in order to help with the time constraints set on the allowable timestep size in non-neutral plasma simulations. An ion solver was implemented using Global Lax scheme in order to effectively remove numerical oscillations from the solution. Several input parameters were varied, and their results compared. Breathing mode oscillations of around 20 kHz are observed and damp over time at differing rates based on the input parameters. A non-neutral sheath region is formed near the anode, and electrons accelerate and gain energy in that region. The increased electron energy leads to high ionization rates in the anode region. The kinetic energy is artificially decreased, and the results are compared and discussed.

This work is nowhere close to being completed, and is simply a stepping stone towards to the broader project of identifying the source of anomalous electron transport in HET's. As a continuation of this work, the drift-diffusion approximation will be abandoned, first by implementing a time-varying drift-diffusion model. This entails ignoring the inertial term in the electron momentum equation, but not the transient term. Once results from that model are obtained and compared to the results of this model, the next step is solving the electron momentum equation fully. A two-fluid model that fully solves the governing equations for both ions and electrons is already in development by my colleague Rupali Sahu. Fully

simulating ions and neutrals, including their respective energy equations, could potentially further expand our understanding of the governing mechanisms.

Once these models are perfected, additional physics will be introduced into the governing equations. For instance, the current models do not account for the self-magnetization of the electrons as they experience azimuthal drift, which may play a role in the anomalous transport. The chemistry model can be further expanded to include metastables and more reactions. Another important development is transitioning the code to being fully two dimensional, in both the axial-radial regime and the axial-azimuthal regimes, in order to observe the multidimensional effects that no doubt play a vital role in dictating the electron transport. In the meantime, the codes developed will be parallelized to utilize multithreading and allow for significantly faster simulations. All these steps are going to hopefully be the basis of my doctoral studies.

REFERENCES

[1] V. Vekselman, M. Feurer, T. Huang, B. Stratton, and Y. Raitses, "Complex structure of the carbon arc discharge for synthesis of nanotubes," *Plasma Sources Sci. Technol.*, vol. 26, no. 6, p. 065019, 2017.

[2] J. Ng and Y. Raitses, "Self-organisation processes in the carbon arc for nanosynthesis," *J. Appl. Phys.*, vol. 117, no. 6, p. 063303, 2015.

[3] J. Drowart, R. P. Burns, G. Demaria, and M. G. Inghram, "Mass spectrometric study of carbon vapor," *J. Chem. Phys.*, vol. 31, no. 4, pp. 1131–1132, 1959.

[4] R. E. Honig, "Mass spectrometric study of the molecular sublimation of graphite," *J. Chem. Phys.*, vol. 22, no. 1, pp. 126–131, 1954.

[5] F. Chen, *Introduction to Plasma Physics and Controlled Fusion*. Springer, 1984.

[6] R. Fitzpatrick, *Plasma Physics: An Introduction*. CRC Press, 2014.

[7] D. Goebel and I. Katz, *Fundamentals of Electric Propulsion: Ion and Hall Thrusters*. Wiley, 2008.

[8] M. Haverkorn and S. R. Spangler, "Plasma diagnostics of the interstellar medium with radio astronomy," *Space Science Reviews*, vol. 178, no. 2, pp. 483–511, 2013.

[9] J. D. Huba, *NRL Plasma Formulary*. U.S. Naval Research Lab, 2007.

[10] M. A. M. A. Lieberman and A. J. Lichtenberg, *Principles of plasma discharges and materials processing*. Wiley-Interscience, 2005.

[11] I. Adamovich, S. D. Baalrud, A. Bogaerts, P. J. Bruggeman, M. Cappelli, V. Colombo, U. Czarnetzki, U. Ebert, J. G. Eden, P. Favia, D. B. Graves, S. Hamaguchi, G. Hieftje, M. Hori, I. D. Kaganovich, U. Kortshagen, M. J. Kushner, N. J. Mason, S. Mazouffre, S. M. Thagard, H.-R. Metelmann, A. Mizuno, E. Moreau, A. B. Murphy, B. A. Niemira, G. S. Oehrlein, Z. L. Petrovic, L. C. Pitchford, Y.-K. Pu, S. Rauf, O. Sakai,

S. Samukawa, S. Starikovskaia, J. Tennyson, K. Terashima, M. M. Turner, M. C. M. van de Sanden, and A. Vardelle, "The 2017 plasma roadmap: Low temperature plasma science and technology," *Journal of Physics D: Applied Physics*, vol. 50, no. 32, p. 323001, 2017.

[12] M. J. Kushner, "Hybrid modelling of low temperature plasmas for fundamental investigations and equipment design," *J. Phys. D: Appl. Phys.*, vol. 42, p. 19, 2009.

[13] M. J. Kushner, "A low temperature plasma science program: Discovery science for societal benefit," August 2014. White Paper to the 2014 FESAC Strategic Planning Panel.

[14] S. A. Ledvina, Y.-J. Ma, and E. Kallio, "Modeling and simulating flowing plasmas and related phenomena," *Space Science Reviews*, vol. 139, no. 1, pp. 143–189, 2008.

[15] G. Colonna and A. D'Angola, eds., *Plasma Modeling*. IOP Publishing, 2016.

[16] K. Hara and K. Hanquist, "Test cases for grid-based direct kinetic modeling of plasma flows," *Plasma Sources Sci. Technol.*, vol. 27, no. 6, p. 065004, 2018.

[17] C. Cercignani, *The Boltzmann Equation*, pp. 40–103. Springer, New York, 1988.

[18] A. Alexeenko, "Lecture notes in boltzmann equation," September 2007.

[19] G. J. M. Hagelaar, *Modelling methods for low-temperature plasmas*. PhD thesis, Université Paul Sabatier, 2008.

[20] M. Mitchner and C. H. Kruger, *Partially Ionized Gases*. Wiley, 1973.

[21] S. Iijima, "Helical microtubules of graphitic carbon," *Nature*, vol. 354, no. 6348, pp. 56–58, 1991.

[22] R. H. Baughman, A. A. Zakhidov, and W. A. De Heer, "Carbon nanotubes - The route toward applications," *Science*, vol. 297, no. 5582, pp. 787–792, 2002.

[23] C. Journet, W. K. Maser, P. Bernier, A. Loiseau, M. Lamy de la Chapelle, S. Lefrant, P. Deniard, R. Lee, and J. E. Fischer, "Synthesis and application of carbon nanotubes," *Nature*, vol. 388, pp. 756–758, 1997.

[24] A. Mansour, M. Razafinimanana, M. Monthioux, M. Pacheco, and A. Gleizes, "A significant improvement of both yield and purity during SWCNT synthesis via the electric arc process," *Carbon N. Y.*, vol. 45, no. 8, pp. 1651–1661, 2007.

[25] R. Andrews, D. Jacques, D. Qian, and T. Rantell, "Multiwall carbon nanotubes: Synthesis and application," *Acc. Chem. Res.*, vol. 35, no. 12, pp. 1008–1017, 2002.

[26] M. V. Antisari, R. Marazzi, and R. Krsmanovic, "Synthesis of multiwall carbon nanotubes by electric arc discharge in liquid environments," *Carbon N. Y.*, vol. 41, no. 12, pp. 2393–2401, 2003.

[27] K. Ostrikov and A. B. Murphy, "Plasma-aided nanofabrication: Where is the cutting edge?," *J. Phys. D. Appl. Phys.*, vol. 40, no. 8, pp. 2223–2241, 2007.

[28] A. Shashurin and M. Keidar, "Synthesis of 2d materials in arc plasmas," *Journal of Physics D: Applied Physics*, vol. 48, no. 31, p. 314007, 2015.

[29] B. C. Stratton, A. Gerakis, I. Kaganovich, M. Keidar, A. Khrabry, J. Mitrani, Y. Raitses, M. N. Shneider, V. Vekselman, and S. Yatom, "In situ diagnostics for nanomaterial synthesis in carbon arc plasma," *Plasma Sources Science and Technology*, vol. 27, no. 8, p. 084001, 2018.

[30] A. Gerakis, Y.-W. Yeh, M. N. Shneider, J. M. Mitrani, B. C. Stratton, and Y. Raitses, "Four-wave-mixing approach to in situ detection of nanoparticles," *Phys. Rev. Applied*, vol. 9, p. 014031, 2018.

[31] S. Yatom, A. Khrabry, J. Mitrani, A. Khodak, I. Kaganovich, V. Vekselman, B. Stratton, and Y. Raitses, "Synthesis of nanoparticles in carbon arc: measurements and modeling," *MRS Communications*, vol. 8, no. 3, pp. 842–849, 2018.

[32] M. S. Benilov, "Understanding and modelling plasma-electrode interaction in high-pressure arc discharges: A review," *J. Phys. D. Appl. Phys.*, vol. 41, no. 14, p. 144001, 2008.

[33] A. Gleizes, "Perspectives on Thermal Plasma Modelling," *Plasma Chem. Plasma Process.*, vol. 35, no. 3, pp. 455–469, 2015.

[34] N. A. Almeida, M. S. Benilov, and G. V. Naidis, "Unified modelling of near-cathode plasma layers in high-pressure arc discharges," *J. Phys. D. Appl. Phys.*, vol. 41, no. 24, p. 245201, 2008.

[35] M. Baeva, "Thermal and Chemical Nonequilibrium Effects in Free-Burning Arcs," *Plasma Chem. Plasma Process.*, vol. 36, no. 1, pp. 151–167, 2016.

[36] A. Khrabry, I. D. Kaganovich, V. Nemchinsky, and A. Khodak, "Investigation of the short argon arc with hot anode. I. Numerical simulations of non-equilibrium effects in the near-electrode regions," *Phys. Plasmas*, vol. 25, no. 1, p. 013522, 2018.

[37] I. P. Raizer, *Gas discharge physics*. Springer-Verlag, 1991.

[38] J. P. Trelles, "Finite Element Methods for Arc Discharge Simulation," *Plasma Process. Polym.*, vol. 14, no. 1-2, p. 1600092, 2017.

[39] M. Baeva and D. Uhrlandt, "Plasma chemistry in the free-burning Ar arc," *J. Phys. D. Appl. Phys.*, vol. 46, no. 32, p. 325202, 2013.

[40] M. Lisnyak, M. D. Cunha, J. M. Bauchire, and M. S. Benilov, "Numerical modelling of high-pressure arc discharges: Matching the LTE arc core with the electrodes," *J. Phys. D. Appl. Phys.*, vol. 50, no. 31, p. 315203, 2017.

[41] V. A. Nemchinsky and Y. Raitses, "Anode sheath transition in an anodic arc for synthesis of nanomaterials," *Plasma Sources Sci. Technol.*, vol. 25, no. 3, p. 035003, 2016.

[42] V. A. Nemchinsky and Y. Raitses, "Atmospheric pressure arc discharge with ablating graphite anode," *J. Phys. D. Appl. Phys.*, vol. 48, no. 24, p. 245202, 2015.

[43] M. Keidar and I. I. Beilis, "Modeling of atmospheric-pressure anodic carbon arc producing carbon nanotubes," *J. Appl. Phys.*, vol. 106, no. 10, p. 103304, 2009.

[44] A. J. Fetterman, Y. Raitses, and M. Keidar, "Enhanced ablation of small anodes in a carbon nanotube arc plasma," *Carbon N. Y.*, vol. 46, no. 10, pp. 1322–1326, 2008.

[45] M. Kundrapu and M. Keidar, "Numerical simulation of carbon arc discharge for nanoparticle synthesis," *Phys. Plasmas*, vol. 19, no. 7, 2012.

[46] J. H. Kim, T. V. Pham, J. H. Hwang, C. S. Kim, and M. J. Kim, "Boron nitride nanotubes: synthesis and applications," *Nano Conv.*, vol. 5, no. 17, 2018.

[47] R. J. Thorn and G. H. Winslow, "Vaporization coefficient of graphite and composition of the equilibrium vapor," *J. Chem. Phys.*, vol. 26, no. 1, pp. 186–196, 1957.

[48] I. Langmuir, "The vapor pressure of metallic tungsten," *Phys. Rev.*, vol. 2, no. 5, pp. 329–342, 1913.

[49] S. Dushman, *Scientific Foundations of Vacuum Techniques*. John Wily & Sons, Inc., 2 ed., 1962.

[50] A. Lefort, M. J. Parizet, S. E. El-Fassi, and M. Abbaoui, "Erosion of graphite electrodes," *J. Phys. D. Appl. Phys.*, vol. 26, no. 8, pp. 1239–1243, 1993.

[51] S. Sasaki, Y. Ohkouchi, S. Takamura, and T. Kato, "Effective Emission and Ionization Rate Coefficients of Atomic Carbons in Plasmas," *J. Phys. Soc. Japan*, vol. 63, no. 8, pp. 2942–2954, 1994.

[52] A. Kramida, Y. Ralchenko, J. Reader, and and NIST ASD Team. NIST Atomic Spectra Database (ver. 5.5.6), [Online]. Available: `https://physics.nist.gov/asd`. National Institute of Standards and Technology, Gaithersburg, MD., 2018.

[53] W. Weltner and R. J. Van Zee, "Carbon Molecules, Ions, and Clusters," *Chem. Rev.*, vol. 89, no. 8, pp. 1713–1747, 1989.

[54] U. Fantz and S. Meir, "Correlation of the intensity ratio of C2/CH molecular bands with the flux ratio of C2Hy/CH4 particles," *J. Nucl. Mater.*, vol. 337-339, no. 1-3 SPEC. ISS., pp. 1087–1091, 2005.

[55] K. P. Huber and G. Herzberg, "Constants of Diatomic Molecules," in *NIST Chem. WebBook, NIST Stand. Ref. Database Number 69*, National Institute of Standards and Technology, Gaithersburg MD, 20899, 2018.

[56] M. Jacox, "Vibrational and Electronic Energy Levels of Polyatomic Transient Molecules," in *NIST Chem. WebBook, NIST Stand. Ref. Database Number 69*, National Institute of Standards and Technology, Gaithersburg MD, 20899, 2018.

[57] O. Krechkivska, G. B. Bacskay, B. A. Welsh, K. Nauta, S. H. Kable, J. F. Stanton, and T. W. Schmidt, "The ionization energy of C 2," *J. Chem. Phys. J. Chem. Phys.*, vol. 144, no. 144, pp. 144305–144305, 2016.

[58] R. Ramanathan, J. A. Zimmerman, and J. R. Eyler, "Ionization potentials of small carbon clusters," *J. Chem. Phys.*, vol. 98, no. 10, pp. 7838–7845, 1993.

[59] H. Suno and T. Kato, "Cross section database for carbon atoms and ions: Electron-impact ionization, excitation, and charge exchange in collisions with hydrogen atoms," *At. Data Nucl. Data Tables*, vol. 92, no. 4, pp. 407–455, 2006.

[60] G. Halmova, *R-matrix calculations of electron-molecule collisions with C2 and C2-*. PhD thesis, University College London, 2008.

[61] H. Munjal and K. L. Baluja, "Elastic and excitation processes of electron impact on C 3 using the R -matrix method," *J. Phys. B At. Mol. Opt. Phys.*, vol. 39, no. 16, pp. 3185–3198, 2006.

[62] L. Curtis, B. Engman, and P. Erman, "High resolution lifetime studies of the d3Πg C1Πg and D1Σu+ States in C2 with applications to estimates of the solar carbon abundance," *Phys. Scr.*, vol. 13, no. 5, pp. 270–274, 1976.

[63] H. Deutsch, K. Becker, and T. D. Märk, "Calculation of absolute electron-impact ionization cross-sections of dimers and trimers," *Eur. Phys. J. D*, vol. 12, no. 2, pp. 283–287, 2000.

[64] L. Vriens and A. H. M. Smeets, "Cross-section and rate formulas for electron-impact ionization, excitation, deexcitation, and total depopulation of excited atoms," *Phys. Rev. A*, vol. 22, no. 3, pp. 940–951, 1980.

[65] P. M. Mul and J. W. McGowan, "Dissociative recombination of C2/+/, C2H/+/, C2H2/+/ and C2H3/+/," *Astrophys J*, vol. 237, pp. 749–751, 1980.

[66] F. G. Blottner, "Prediction of Electron Density in the Boundary Layer on Entry Vehicles with Ablation," *NASA Special Publication*, vol. 252, p. 219, 1971.

[67] S. Díaz-Tendero, G. Sánchez, P.-A. Hervieux, M. Alcamí, and F. Martín, "Ionization potentials, dissociation energies and statistical fragmentation of neutral and positively charged small carbon clusters," *Brazilian J. Phys.*, vol. 36, no. 2b, pp. 529–533, 2006.

[68] W. Vincenti and C. Kruger, *Introduction to physical gas dynamics*. Krieger, 1967.

[69] W. Wang, M. Rong, A. B. Murphy, Y. Wu, J. W. Spencer, J. D. Yan, and M. T. Fang, "Thermophysical properties of carbon-argon and carbon-helium plasmas," *J. Phys. D. Appl. Phys.*, vol. 44, no. 35, p. 355207, 2011.

[70] J. Pousse, B. Chervy, J.-F. Bilodeau, and A. Gleizes, "Thermodynamic and transport properties of argon/carbon and helium/carbon mixtures in fullerene synthesis," *Plasma Chem. Plasma Process.*, vol. 16, no. 4, pp. 605–634, 1996.

[71] V. Vekselman, A. Khrabry, I. Kaganovich, B. Stratton, R. S. Selinsky, and Y. Raitses, "Quantitative imaging of carbon dimer precursor for nanomaterial synthesis in the carbon arc," *Plasma Sources Sci. Technol.*, vol. 27, no. 2, p. 025008, 2018.

[72] Z. Han and A. Fina, "Thermal conductivity of carbon nanotubes and their polymer nanocomposites: A review," *Prog. Polym. Sci.*, vol. 36, no. 7, pp. 914–944, 2011.

[73] J. L. Steger and R. F. Warming, "Flux vector splitting of the inviscid gasdynamic equations with application to finite-difference methods," *J. Comput. Phys.*, vol. 40, no. 2, pp. 263–293, 1981.

[74] B. Van Leer, "Towards the ultimate conservative difference scheme. IV. A new approach to numerical convection," *J. Comput. Phys.*, vol. 23, no. 3, pp. 276–299, 1977.

[75] G. Yang and J. Heberlein, "Anode attachment modes and their formation in a high intensity argon arc," *Plasma Sources Sci. Technol.*, vol. 16, no. 3, pp. 529–542, 2007.

[76] A. Shashurin, M. Keidar, and I. I. Beilis, "Voltage-current characteristics of an anodic arc producing carbon nanotubes," *J. Appl. Phys.*, vol. 104, no. 6, p. 063311, 2008.

[77] H. Lange, K. Saidane, M. Razafinimanana, and A. Gleizes, "Temperatures and C2 column densities in a carbon arc plasma," *J. Phys. D. Appl. Phys.*, vol. 32, no. 9, pp. 1024–1030, 1999.

[78] S. Robertson, "Sheath and presheath in plasma with warm ions," *Phys. Plasmas*, vol. 16, no. 10, p. 103503, 2009.

[79] H. Valentini, "Bohm criterion for the collisional sheath," *Phys. Plasmas*, vol. 3, no. 4, pp. 1459–1461, 1996.

[80] V. V. Zhurin, H. R. Kaufman, and R. S. Robinson, "Physics of closed drift thrusters," *Plasma Sources Sci. Technol.*, vol. 8, p. R1, 1999.

[81] J. P. Boeuf and L. Garrigues, "Low frequency oscillations in a stationary plasma thruster," *J. Appl. Phys.*, vol. 84, pp. 3541–3554, 1998.

[82] R. R. Hofer, D. M. Goebel, I. G. Mikellides, and I. Katz, "Magnetic shielding of a laboratory hall thruster. ii. experiments," *Journal of Applied Physics*, vol. 115, no. 4, p. 043304, 2014.

[83] S. E. Cusson, M. P. Georgin, H. C. Dragnea, E. T. Dale, V. Dhaliwal, I. D. Boyd, and A. D. Gallimore, "On channel interactions in nested hall thrusters," *J. of Appl. Phys.*, vol. 123, no. 13, p. 133303, 2018.

[84] K. Hara, "An overview of discharge plasma modeling for hall effect thrusters," *Plasma Sources Sci. Technol.*, vol. 28, p. 044001, 2019.

[85] T. Lafleur, S. D. Baalrud, and P. Chabert, "Theory for the anomalous electron transport in hall effect thrusters. i. insights from particle-in-cell simulations," *Phys. Plasma.*, vol. 23, p. 053502, 2016.

[86] J. P. Boeuf, "Tutorial: physics and modeling of hall thrusters," *J. Appl. Phys.*, vol. 121, p. 011101, 2017.

[87] A. I. Smolyakov, W. Frias, I. D. Kaganovich, and Y. Raitses, "Sheath-induced instabilities in plasmas with $\mathbf{e}_0 \times \mathbf{b}_0$ drift," *Phys. Rev. Lett.*, vol. 111, p. 115002, 2013.

[88] I. Mikellides, B. Jorns, I. Katz, and A. Lopez Ortega, "Hall2de simulations with a first-principles electron transport model based on the electron cyclotron drift instability," in *34th International Electric Propulsion Conference*, 07 2016.

[89] K. Hara, I. D. Boyd, and V. I. Kolobov, "One-dimensional hybrid-direct kinetic simulation of the discharge plasma in a hall thruster," *Phys. Plasma.*, vol. 19, p. 113508, 2012.

[90] I. G. Mikellides and I. Katz, "Numerical simulations of hall-effect plasma accelerators on a magnetic-field-aligned mesh," *Phys. Rev. E*, vol. 86, p. 046703, 2012.

[91] S. I. Braginskii, "Transport processes in a plasma," *Reviews of Plasma Physics*, vol. 1, p. 205, 1965.

[92] J. W. Koo and I. D. Boyd, "Computational model of a hall thruster," *Comp. Phys. Comm.*, vol. 164, pp. 442 – 447, 2004.

[93] G. J. M. Hagelaar, J. Bareilles, L. Garrigues, and J. P. Boeuf, "Role of anomalous electron transport in a stationary plasma thruster simulation," *J. Appl. Phys.*, vol. 93, pp. 67–75, 2003.

[94] K. Hara, "Non-oscillatory quasineutral fluid model of cross-field discharge plasmas," *Phys. Plasmas*, vol. 25, no. 12, p. 123508, 2018.

[95] Z. He, Y. Zhang, X. Li, L. Li, and B. Tian, "Preventing numerical oscillations in the flux-split based finite difference method for compressible flows with discontinuities," *J. Comp. Phys.*, vol. 300, pp. 269 – 287, 2015.

[96] D. L. Scharfetter and H. K. Gummel, "Large-signal analysis of a silicon read diode oscillator," *IEEE Transactions on Electron Devices*, vol. 16, no. 1, pp. 64–77, 1969.

[97] W. R. Frensley, "Scharfetter-gummel discretization scheme for drift-diffusion equations," April 2004.

[98] G. J. M. Hagelaar and G. M. W. Kroesen, "Speeding up fluid models for gas discharges by implicit treatment of the electron energy source term," *J. Comp. Phys.*, vol. 159, no. 1, pp. 1 – 12, 2000.

[99] A. Theunissen, "Numerically solving pde's: Crank-nicholson algorithm," March 2006. BUS 864 Computing Notes.

[100] G. Recktenwald, "Finite-difference approximations to the heat equation," March 2011.

[101] L. Liu, *Studies on the discretization of plasma transport equations*. PhD thesis, Eindhoven: Technische Universiteit, 2013.

[102] J. W. Koo and I. D. Boyd, "Modeling of anomalous electron mobility in hall thrusters," *Physics of Plasmas*, vol. 13, no. 3, p. 033501, 2006.

[103] L. Dorf, Y. Raitses, and N. J. Fisch, "Experimental studies of anode sheath phenomena in a hall thruster discharge," *J. Appl. Phys.*, vol. 97, no. 10, p. 103309, 2005.

[104] K. Hara, M. J. Sekerak, A. D. Gallimore, and I. D. Boyd, "Breathing mode in hall effect thrusters," in *34th International Electric Propulsion Conference*, 07 2015.

[105] M. J. Sekerak, A. D. Gallimore, D. L. Brown, R. R. Hofer, and J. E. Polk, "Mode transitions in hall-effect thrusters induced by variable magnetic field strength," *J. Propul. Power*, vol. 32, no. 4, pp. 903–917, 2016.

[106] K. Hara, S. Keller, and Y. Raitses, *Measurements and theory of driven breathing oscillations in a Hall effect thruster*. AIAA, 2016.

[107] W. T. Lee, "Tridiagonal matrices: Thomas algorithm," November 2011. MS6021 Scientific Computation.

[108] W. K. Anderson, J. L. Thomas, and B. Van Leer, "Comparison of finite volume flux vector splittings for the Euler equations," *AIAA J.*, vol. 24, no. 9, pp. 1453–1460, 1986.

[109] J. Droniou, "Muscl methods," September 2008. A beginner's course in finite volume approximation of scalar conservation laws.

APPENDIX A

THOMAS TRIDIAGONAL MATRIX SOLVER

Thomas tridiagonal matrix algorithm is a highly efficient variation of Gauss elimination, used to inexpensively solve systems of tridiagonal equations of the form $a_j x_{j-1} + b_j x_j + c_j x_{j+1} = d_j$. The algorithm returns the solution with $O(n)$ operations for n unknowns, as opposed to $O(n^3)$ for Gauss elimination. The algorithm begins by filling out the tridiagonal matrix components a_j, b_j, c_j and the load vector d_j for all $1 < j < n$. The components for $j = 1$ and $j = n$ correspond to the boundary conditions imposed on the system, with $a_1 = 0$ and $c_n = 0$.

The algorithm consists of a forward sweep followed by a back substitution. The forward sweep is performed over $j = 2, 3, .., n$ such that:

$$w = \frac{a_j}{b_{j-1}},$$

$$b_j = b_j - w c_{j-1},$$

$$d_j = d_j - w d_{i-1}.$$

This is then followed by the backward substitution. First, x_n is evaluated:

$$x_n = \frac{d_n}{b_n},$$

after which the values of x_j are subsequently evaluated, going backwards such that $j = n-1, n-2, ..., 1$:

$$x_j = \frac{s_j - c_j x_{j+1}}{b_j}.$$

For the algorithm to be stable, the tridiagonal matrix must be diagonally dominant, such that $|b_j| > |a_j| + |c_j|$ for all j [107].

APPENDIX B

STEGER-WARMING SCHEME WITH MUSCL RECONSTRUCTION FOR INVISCID FLUX

Excluding source and collisional terms, the left hand side of the conservation equations follows the form of the inviscid Euler formulation, given by:

$$\frac{\partial Q}{\partial t} + \frac{\partial F}{\partial x} = 0, \tag{B.1}$$

where $Q = [\rho, \rho u, \rho\varepsilon]^T$ are the state variables corresponding to continuity, momentum conservation and energy conservation, respectively, $F = [\rho u, \rho u^2 + p, (\rho\varepsilon + p)u]^T$ are the inviscid fluxes, and ε is the total energy per unit volume. The state variables Q are located on the cell centers, whereas the fluxes F are evaluated at the cell interfaces.

B.1 Steger-Warming Scheme

Steger-Warming employs FVS by evaluating the eigenvalues of the Jacobian matrix obtained from Eq. (B.1) [73]. The eigenvalues for the Euler equation are $\lambda_1 = u$, $\lambda_2 = u + c$, and $\lambda_3 = u - c$, where $c = (\gamma p/\rho)^{1/2}$ is the local speed of sound. The numerical procedure begins with the reconstruction of the cell-center conservative quantities. This way, every cell interface will have two values, Q^L and Q^R, corresponding to the reconstructed value on the left and on the right side, respectively.

After that, the flux vector F is split into two parts, F^+ and F^-, which correspond to the flux vectors associated with the positive and negative eigenvalues, respectively. Here, the positive and negative eigenvalues on the cell interfaces are calculated as $\lambda_j^+ = \max(\lambda_{j,L}, 0)$ and $\lambda_j^- = \min(\lambda_{j,R}, 0)$ for $j = 1, 2, 3$. The numerical fluxes are then calculated as

$$
\begin{aligned}
F_{\rho}^{\pm} &= \frac{\rho^{\pm}}{2\gamma}[2(\gamma-1)\lambda_1^{\pm} + \lambda_2^{\pm} + \lambda_3^{\pm}], \\
F_{\rho u}^{\pm} &= \frac{\rho^{\pm}}{2\gamma}\left[2(\gamma-1)\lambda_1^{\pm}u^{\pm} + \lambda_2^{\pm}(u+c)^{\pm} + \lambda_3^{\pm}(u-c)^{\pm}\right], \\
F_{\rho u}^{\pm} &= \frac{\rho^{\pm}}{4\gamma}\left[2(\gamma-1)\lambda_1^{\pm}(u^{\pm})^2 + \lambda_2^{\pm}[(u+c)^{\pm}]^2 + \lambda_3^{\pm}[(u-c)^{\pm}]^2 + w\right],
\end{aligned}
$$

where $w = (3-\gamma)(\lambda_2^{\pm} + \lambda_3^{\pm})c^2/(\gamma-1)$. The so-called sonic problem for rarefaction waves can be eliminated using MUSCL reconstruction [108], which guarantees a smooth solution without numerical oscillations.

B.2 Monotonic Upwind Scheme for Conservation Laws (MUSCL)

FVS methods require that quantities be discretized on the cell interfaces in order to evaluate the fluxes. Since quantities reside on the cell centers in finite volume methods, an interpolation scheme is needed to populate the cell interfaces. One of the most commonly used schemes is monotonic upwind scheme for conservation laws (MUSCL), which reconstruct the solutions as piecewise discontinuous linear approximations in the interval of the finite volume $[j-1/2, j+1/2]$ [109]. The evaluated slopes in the cells allow for the evaluation of the quantities on the right and left side of the cell interfaces. Limiters such as MINMOD, Koren, Van Leer, and others are utilized to ensure the reconstructed values are not out of the bounds of the cell centered quantities, in order to ensure stability. In the models discussed in this thesis, a Koren limiter is used.

To exemplify the implementation of MUSCL, cell interface $j+1/2$ is considered, and placeholder quantity u is being reconstructed. In order to evaluate $u_{j+1/2}^{+}$, which is the left

component on the interface, the slopes are defined as:

$$s_1 = u_j - u_{j-1},$$

$$s_2 = u_{j+1} - u_j,$$

where s_1 and s_2 are the slopes over the intervals $[j-1, j]$ and $[j, j+1]$, respectively. If the two slopes share the same signs, then the reconstructed slope is given by:

$$\psi = \min\left[2, \min\left[2\left(\frac{s_1}{s_2}\right), \frac{2 + s_1/s_2}{3}\right]\right], \tag{B.2}$$

where ψ is the reconstructed slope. If the two slopes s_1 and s_2 have opposing signs, then $\psi = 0$ is taken. The left interface quantity is then evaluated as:

$$u^+_{j+1/2} = u_j + \frac{\psi}{2}(u_{j+1} - u_j).$$

To evaluate $u^-_{j+1/2}$, which is the right component on the interface, then the slopes are defined as:

$$s_1 = u_{j+1} - u_j,$$

$$s_2 = u_{j+2} - u_{j+1},$$

where the slopes are over intervals $[j, j+1]$ and $[j+1, j+2]$, respectively. The reconstructed slope ψ is given by Eq. (B.2), or is set to be zero of s_1 and s_2 have opposite signs. The right interface quantity is then evaluated as:

$$u^-_{j+1/2} = u_{j+1} - \frac{\psi}{2}(u_{j+2} - u_{j-1}).$$

The interface quantities can then be fed into the FVS method, ensuring a smooth solution with no numerical oscillations originating from the evaluation of the cell interface quantities.

B.3 Global Lax-Friedrichs

The use of a local FVS method can lead to the formation of oscillations at locations of stationary contact discontinuities, where the local velocity is zero [95]. In order to resolve this issue, a global FVS method is used. Global Lax-Friedrichs introduced a global parameter β that is accounted for in the calculation of the eigenvalues used to calculate the fluxes described above. The value of β is taken to be the maximum eigenvalue throughout the domain, such that $\beta = \max(\lambda_1^{\pm}, \lambda_2^{\pm}, \lambda_3^{\pm})$. The local eigenvalues $\lambda_1^{\pm}$, $\lambda_2^{\pm}$ and $\lambda_3^{\pm}$ are then modified by adding (in the case of λ^+) or subtracting (in the case of λ^-) β and dividing by 2, thus effectively taking the average between the local eigenvalue and the absolute maximum eigenvalue in the domain. This ensures non-zero eigenvalues throughout the domain. The modified eigenvalues are used to calculate the fluxes as previously described, and the calculations proceed without the development of oscillations.

APPENDIX C

CRANK-NICOLSON METHOD

Crank-Nicolson is a semi-implicit method of integration that uses quantities from both the current timestep k and the future timestep $k+1$ to evaluate quantities in the future timestep. It is used to solve the fluid energy equation in order to avoid timestep restrictions imposed by the conductive term of the heat equation [100]. The method will be presented here using the following 1D equation as an example [99]:

$$a\frac{\partial^2 u}{\partial x^2} + b\frac{\partial u}{\partial x} + c - \frac{\partial u}{\partial t} = 0,$$

where a, b, and c are parameters not directly dependent on u. The terms of the equation can be seen as corresponding to the conductive term, the convective term, the source terms, and the time varying term of the temperature equation, respectively. The implementation of Crank-Nicolson discretizes the spatial terms as an average between the two timesteps, such that:

$$\frac{\partial u}{\partial x} = \frac{u^k_{j+1} - u^k_{j-1} + u^{k+1}_{j+1} - u^{k+1}_{j-1}}{4\Delta x},$$

$$\frac{\partial^2 u}{\partial x^2} = \frac{u^k_{j+1} - 2u^k_j + u^k_{j-1} + u^{k+1}_{j+1} - 2u^{k+1}_j + u^{k+1}_{j-1}}{2\Delta x^2},$$

when the operators are discretized around point j. Discretizing the PDE above and grouping terms from the future timestep on the left hand side and terms from the current timestep on the right hand side, the equation becomes:

$$(2a\Delta t + b\Delta x\Delta t)u_{j+1}^{k+1} - (4a\Delta t + 2\Delta x^2)u_j^{k+1} + (2a\Delta t - b\Delta t\Delta x)u_{j-1}^{k+1}$$

$$= -(2a\Delta t + b\Delta x\Delta t)u_{j+1}^{k} + (4a\Delta t + 2\Delta x^2)u_j^{k} - (2a\Delta t - b\Delta t\Delta x)u_{j-1}^{k} - 2c\Delta t\Delta x^2,$$

which takes the tridiagonal form, with the right hand side being the load vector. This system is then solved using Thomas tridiagonal matrix solver from Appendix A.